# Analysis of long-term closure in drifts excavated in Callovo-Oxfordian claystone : roles of anisotropy and hydromechanical couplings

Lina María Guayacan Carrillo

▶ **To cite this version:**

Lina María Guayacan Carrillo. Analysis of long-term closure in drifts excavated in Callovo-Oxfordian claystone : roles of anisotropy and hydromechanical couplings. Geophysics [physics.geo-ph]. Université Paris-Est, 2016. English. NNT : 2016PESC1120 . tel-01542407

HAL Id: tel-01542407

https://pastel.hal.science/tel-01542407

Submitted on 19 Jun 2017

# ANALYSIS OF LONG-TERM CLOSURE IN DRIFTS EXCAVATED IN CALLOVO-OXFORDIAN CLAYSTONE: ROLES OF ANISOTROPY AND HYDROMECHANICAL COUPLINGS

Thèse soumise pour l'obtention du grade de

*Docteur de l'Université Paris Est*

Ecole Doctorale Sciences, Ingénierie et Environnement (SIE)

Spécialité : *Géotechnique*

présentée le 9 décembre 2016 à Champs-sur-Marne par

*Lina María GUAYACAN CARRILLO*

JURY

| | | |
|---|---|---|
| Pr. Fréderic PELLET | École des Mines Paris-Tech | Président du Jury |
| Pr. Giovanni BARLA | Politecnico di Torino | Rapporteur |
| Pr. Jian-Fu SHAO | Ecole Polytechnique – Université de Lille | Rapporteur |
| Pr. Georg ANAGNOSTOU | Swiss Federal Inst. of Technology in Zurich | Examinateur |
| Dr. Gilles ARMAND | Andra R&D | Examinateur |
| Pr. Jean SULEM | Ecole des Ponts ParisTech | Directeur de thèse |
| Dr. Siavash GHABEZLOO | Ecole des Ponts ParisTech | Co-encadrant de thèse |
| Dr. Darius SEYEDI | Andra R&D | Co-encadrant de thèse |

*A mi más grande tesoro:*

*Mi familia,*

*Gracias por su apoyo incondicional*

# ACKNOWLEDGEMENTS

# ABSTRACT

The French National Radioactive Waste Management Agency (Andra) began in 2000 the construction of an Underground Research Laboratory (URL) with the main goal of demonstrating the feasibility of a geological repository in Callovo-Oxfordian claystone. Several research programs have taken place to improve the knowledge of the rock properties and its response to the excavation progress. A network of experimental drifts has been constructed with variations on: excavation method, structure geometry, supports system and orientations with respect to principal stresses' directions. In each drift different sections have been instrumented to monitor the hydro-mechanical behavior of the rock mass formation. Continuous monitoring of the excavated zone around the drifts in the main level (-490 m) revealed the development of a fractured zone (extensional and shear fractures) induced by the excavation. The extent of this fractured zone depends on the drift orientation regarding the in-situ stress field. Accordingly, the convergence measurements showed an anisotropic closure which depends also on the drifts' orientations. Moreover, marked overpressures and an anisotropic pore pressure field around the drifts have been also observed.

The approach proposed in this work is mainly based on a direct analysis of the convergence measurements, for studying the anisotropic response of the rock formation during and after excavation. The convergence evolution is analyzed on the basis of the semi-empirical law proposed by Sulem et al. (1987) [Int J Rock Mech Min Sci Geomech Abstr 24: 145–154]. The monitoring and analysis of convergence data can provide a reliable approach of the interaction between rock mass and support. Therefore, the anisotropy and the variability of the closure are analyzed taking into account different field cases: drifts excavated in two different orientations (i.e. influence of the initial stress state), different methods, sizes and rates of excavation and different supports systems with different conditions of installation. This broad range of cases permits to refine the analysis for reliable predictions of the convergence evolution in the long term. This approach can thus be used for the design of various types of support and the evaluation of its performance in the long term.

On the other hand, the pore pressure evolution induced by excavation of drifts as recorded in-situ has been analyzed. The anisotropic response observed in-situ suggests that the intrinsic anisotropy of the material plays a key role in the response of the rock formation. To understand these phenomena, an anisotropic poroelastic analysis of the pore pressure evolution induced by the drift excavation is performed. The main goal is to simulate the main trends of the pore pressure evolution with a simple model taking into account the inherent anisotropy of the material. Finally, an analysis of the onset of failure shows the key role of the hydro-mechanical coupling on the extension of the failed zone around the drifts.

# RESUME

L'Agence nationale pour la gestion des déchets radioactifs (Andra) a commencé en 2000 la construction du Laboratoire Souterrain de Meuse / Haute-Marne (LS-M/HM) avec l'objectif principal de démontrer la faisabilité d'un stockage géologique dans l'argilite du Callovo-Oxfordien. Un réseau de galeries expérimentales a été excavé, principalement en suivant les directions des contraintes horizontales (majeure et mineure), avec des variations sur : la méthode d'excavation, la géométrie de la structure et le soutènement. Chaque galerie a été instrumentée en différentes sections pour suivre le comportement hydromécanique de la roche face à l'excavation. Le suivi de la zone autour des galeries excavées au niveau principal (-490 m) a révélé le développement d'une zone fracturée (fractures en extension et en cisaillement) induite par l'excavation. La distribution de la zone fracturée dépend à la fois de l'orientation de la galerie et du champ de contraintes in-situ et a une influence importante sur la déformation des galeries. En effet, les mesures de convergence ont montré une fermeture anisotrope de la section de la galerie. De plus, il a été observé un champ de distribution anisotrope de la pression de pores ainsi que des surpressions autour des galeries.

Afin d'analyser la réponse anisotrope du massif pendant l'excavation et après celle-ci, les travaux effectués dans le cadre de la thèse sont axés principalement sur une étude directe des mesures de convergence in-situ. Cette analyse s'effectue à l'aide de la loi semi-empirique proposée par Sulem et al. (1987) [Int J Rock Mech Min Sci Geomech Abstr 24: 145–154]. A cet égard, différentes galeries excavées dans le LS-M/HM ont été étudiées. Ces galeries présentent certaines différences dans leurs orientations et l'état initial des contraintes, dans la méthode et la vitesse d'excavation ainsi que dans les diamètres de la section et les types de soutènements installés. Cette analyse permet d'obtenir des prédictions fiables de la convergence à long-terme, ce qui peut servir pour le dimensionnement et la prévision de la performance du soutènement à long-terme.

En outre, nous avons étudié la réponse anisotrope du champ de pression interstitielle observée in-situ. Cette analyse est basée sur une approche poroélastique anisotrope. L'objectif principal est de reproduire qualitativement l'évolution de la pression des pores autour des galeries avec une approche simple qui prend en compte l'anisotropie intrinsèque du matériau. Enfin, une analyse de l'apparition de la rupture montre le rôle clé que joue le couplage hydromécanique dans l'extension de la zone fracturée.

**Mots-clés**: convergences, déformation des tunnels, comportement différé, anisotropie, argilite du Callovo-Oxfordien, excavation souterraine, effets d'échelle, couplage hydromécanique, poroelasticité

*International journals*

- Guayacán-Carrillo LM, Sulem J, Seyedi DM, Ghabezloo S, Noiret A & Armand G (2016). Analysis of long-term anisotropic convergence in drifts excavated in Callovo-Oxfordian claystone. *Rock Mechanics and Rock Engineering, 49(1),* pp 97-114. doi: 10.1007/s00603-015-0737-7.

- Guayacán-Carrillo LM, Sulem J, Seyedi DM, Ghabezloo S, Noiret A & Armand G (2016). Convergence analysis of an unsupported micro-tunnel at the Meuse/Haute-Marne underground research laboratory. In: *Radioactive Waste Confinement: Clays in Natural and Engineered Barriers. Geological Society of London (GSL) Special Publication SP443. 24.* doi:10.1144/SP443.24.

- Guayacán-Carrillo LM, Sulem J, Seyedi DM, Ghabezloo S & Armand G (2016). Size effect on the time-dependent closure of drifts excavated in Callovo-Oxfordian claystone. *Tunnelling and Underground Space Technology.* (Submitted).

- Guayacán-Carrillo LM, Ghabezloo S, Sulem J, Seyedi DM & Armand G (2016). Effect of anisotropy and hydro-mechanical couplings on pore pressure evolution during tunnel excavation in low-permeability ground. *International Journal of Rock Mechanics and Mining Sciences.* (Accepted).

*International Conferences (peer-reviewed)*

- Guayacán-Carrillo LM, Sulem J, Seyedi DM, Ghabezloo S, Noiret A & Armand G (2015). Anisotropic closure analysis of a drift in Callovo-Oxfordian claystone based on in-situ convergence data. *Proc. 13th ISRM Congress. Montréal, Mai 2015.* ISBN 978-1-926872-25-4.

- Guayacán-Carrillo LM, Sulem J, Noiret A, Seyedi DM, Ghabezloo S & Armand G (2016). Analyse de la convergence à long terme des galeries dans l'argilite du Callovo-oxfordien. *Journées Nationales de Géotechnique et de Géologie de l'Ingénieur, Nancy, Juillet 2016.*
  http://jngg2016.sciencesconf.org/80814/document.

- Guayacán-Carrillo LM, Seyedi DM, Sulem J, Ghabezloo S, Noiret A & Armand G (2016). The effect of over excavation on the time-dependent convergence of a drift in Callovo-Oxfordian claystone. In: *Ulusay et al. (eds), Rock Mechanics and Rock Engineering: From the Past to the Future. Proc. ISRM International Symposium and EUROCK 2016, August 2016*, pp 945-950. ISBN 978-1-138-03265-1.

- Guayacán-Carrillo LM, Seyedi DM, Sulem J, Ghabezloo S, Noiret A & Armand G (2016). Tunnel excavation in low permeability ground: effect of anisotropy on excess pore pressure. In: *Ulusay et al. (eds), Rock Mechanics and Rock Engineering: From the Past to the Future. Proc. ISRM International Symposium and EUROCK 2016, August 2016*, pp 463-467. ISBN 978-1-138-03265-1.

*International Conferences (without proceedings)*

- Guayacán-Carrillo LM, Sulem J, Seyedi DM, Ghabezloo S, Noiret A & Armand G (2014). Analysis of convergence measurements in drifts in Callovo-Oxfordian Claystone. *Poster presented in 25th ALERT Workshop, Aussois, October 2014.* Booklet of abstracts ISBN 978-2-9542517-2-1.

- Guayacán-Carrillo LM, Sulem J, Seyedi DM, Ghabezloo S, Noiret A & Armand G (2015). Anisotropic convergence analysis in drifts of the Meuse/haute-Marne underground research laboratory. *Poster presented in 6th International Clay Conference, Brussels, March 2015.*

- Guayacán-Carrillo LM, Sulem J, Ghabezloo S, Seyedi DM & Armand G (2016). Tunnel excavations in low-permeability anisotropic ground: hydromechanical couplings. *Oral presentation in EMI International Conference, Metz, October 2016.*

# TABLE OF CONTENTS

# LIST OF TABLES

# LIST OF FIGURES

# INTRODUCTION

The radioactive waste disposal has been a key issue for several years in France. Thousands of cubic meters of radioactive wastes are produced each year. Nowadays, about 90% of the total wastes (mainly Low and intermediate level, short-lived radioactive wastes (LILW-SL) and Very-low-level wastes (VLLW)) are managed in France by existing disposal centers (e.g. CSA (Centre de stockage de l'Aube), Cires (Le Centre industriel de regroupement, d'entreposage et de stockage)). However, the other wastes, among them the High level wastes (HLW) and Intermediate level – Long lived wastes (IL-LLW), cannot be disposed in the centers at the surface for safety reasons (Andra 2013a). Therefore, an appropriate solution is required for these types of waste.

Deep geological formations with favorable characteristics for the radioactive waste disposal are considered to be a good alternative and a safe solution in France and in other countries (e.g. Belgium, Canada, Switzerland, Sweden…), where Underground Research Laboratories (URL) have been implemented in order to demonstrate the feasibility of constructing and operating a radioactive waste disposal facility within a geological formation (NEA 2001). As explained by Delay et al. (2014), experiments in the URLs meet to sets of needs: (a) characterization, that is, acquiring knowledge of the geological, hydro-geological, geochemical, structural and mechanical properties of the host rock and of its response to perturbations; and (b) construction and operation, that is, developing equipment to acquire know-how about the construction of all the components of a disposal facility up to its closure, and the emplacement and/or retrieval of the waste.

The law of 30 December 1991 has formally assigned the French national radioactive waste management agency (Andra: Agence Nationale pour la gestion des déchets radioactifs) the mission to analyze the feasibility of a geological repository in deep geological formation (Andra 2005). After several years of research, the Callovo-Oxfordian claystone has been chosen as the potential geological barrier for the disposal of HL and IL-LL wastes. This formation presents favorable characteristics considering its very low permeability, small molecular diffusion and significant retention capacity for radionuclide (Andra 2005, Armand et al. 2013). In 2000, Andra began the construction of the Meuse/Haute-Marne Underground Research Laboratory (M/HM URL) at Bure (East of Paris sedimentary basin) with the main goal of demonstrating the feasibility of geological repository in Callovo-Oxfordian claystone. As explained by Armand et al. (2015a), the main goal of the first research phase (2000-2005) was to characterize the confining properties of the clay through in-situ hydrological tests, chemical measurements and diffusion experiments. Moreover, this first phase aimed to demonstrate that the construction and

operation of a geological repository would not introduce pathways for radionuclides migration (Delay et al. 2007). Then, since 2005, the research program is more dedicated to technologies improvement and demonstration issues of the different disposal systems, even if characterization studies are still ongoing (Armand et al. 2015a).

The design of the geological repository presents different strategic issues related to the justification of different adopted decisions and the demonstration of the feasibility and safety after the repository closure (i.e. for thousands of years). To meet these requirements and the reversibility during about 100 years, the design of the CIGEO facility (Industrial center for geological disposal / Centre Industriel de Stockage Géologique) needs to be based on an iterative process considering: the knowledge acquisition, phenomenological modeling and engineering approaches, as explained by Ozanam et al. (2016). For that purpose, the M/HM URL plays a key role in the knowledge acquisition. Thereby, in 2006 a step by step approach has been initiated (Armand et al. 2015a), which is carried out based on comparison of hydro-mechanical behavior of drifts excavated with variations on: excavation method, structure geometry, supports system and orientations with respect to the principal stresses' directions. Each drift excavation is an experiment in itself and is used to characterize the response of the rock to different drift construction methods.

### *The Industrial Center for Geological Disposal project (CIGEO)*

CIGEO is conceived to give definitive and passive safety for the radioactive HL and IL-LL wastes, at about 500 m depth in a claystone formation. It is composed of different types of excavations as presented in Fig. I.1 (i.e. Shafts for construction and ventilation, ramps for waste packages and general service, drifts for the IL-LL waste disposal zone, drifts for HL waste disposal zone). For the IL-LL wastes, the drifts will be excavated with a size between 9 to 11 m, where precast concrete rectangular containers (containing the IL-LLW) will be stored. Concerning the HL wastes, vitrified HL waste Stainless Canister (primary waste) will be placed in thick steel overpacks, which at its turn will be placed in horizontal micro-tunnels with a diameter of about 0.7 m (Andra 2009; Armand et al. 2015a).

Most of these drifts will be exploited for more than hundred years. Therefore, nonstop service continuity is required without human intervention for drifts maintenance. One of the main issues is to determine the optimal size, excavation and support methods for each drift depending on the duties attributed to each one. CIGEO design and development are performed in an incremental way. Cells will be added progressively as the operation progresses until they reach a total maximum area of about 15 km$^2$, after about 100 years. The ulterior drifts will be adapted and

optimized according to the feedback obtained from the monitoring and follow-up of the first drifts excavated. CIGEO will be placed in the area near the M/HM URL. The installations will be progressively built, operated and finally closed over a period of roughly 150 years (Armand et al. 2015a).
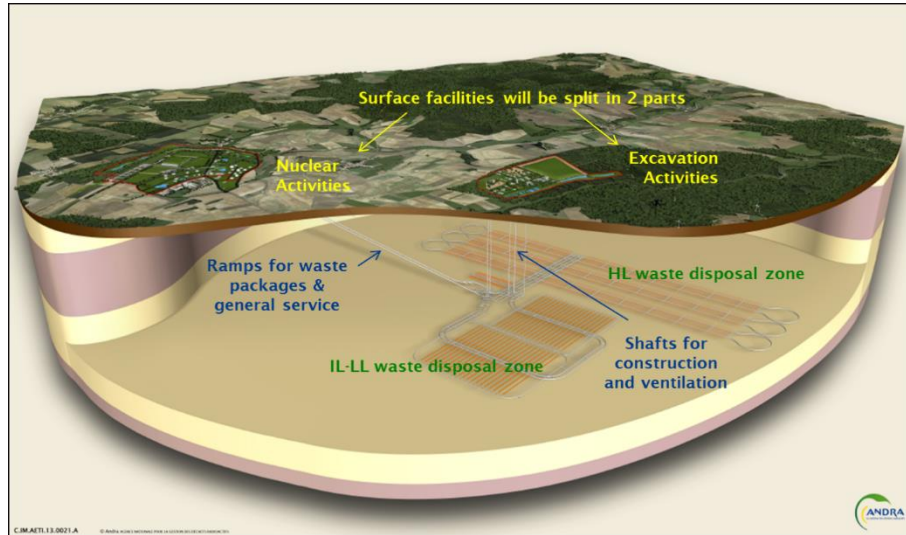


**Fig. I. 1.** Schema of CIGEO: Industrial Center for Geological Disposal (adapted from Armand et al. 2015a)

### Outline and presentation of the Thesis content

An important part of the knowledge acquired about the host rock behavior and its response to the excavation works is obtained by means of the research performed at the M/HM URL, which gives a feedback on the underground excavations in the Callovo-Oxfordian claystone for more than 10 years. The research program has been mainly related to: the characterization of the thermo-hydro-mechanical behavior of the rock mass formation; the analysis of the hydro-mechanical response of the rock mass to drift and shaft excavations (short- and long-term behavior); the characterization of the Excavation Damaged Zone (EDZ) developed around drifts; the interaction between the rock and the support and also the support response. This research aims at identifying, understanding and modeling the physical processes to give valuables insights for the optimization of CIGEO design.

In-situ observations show that the response of the Callovo-Oxfordian claystone to the excavation works depends on different features including the initial stress state, the intrinsic anisotropy of the material, the excavation method…. A remarkable in-situ observation is the anisotropic response which is mainly evidenced in: the extension of the induced fracture network, the drifts closure and the pore pressure field around drifts. Within this context, the present work addresses the question

of the anisotropic closure of drifts by means of a direct and extensive analysis of the in-situ measurements.

This dissertation is structured in three parts:

***Part I***: The first part describes the Meuse/Haute-Marne Underground research laboratory (M/HM URL). First the hydro-mechanical properties of the Callovo-Oxfordian claystone are summarized. Then, the excavation and support methods used in the construction of the different experimental drifts are described. An overview of the drifts installations and the set up for the performed hydro-mechanical measurements are described in detail and the in-situ observations at the M/HM URL are summarized. Finally, an overview of the existing models for the characterization of the rock mass behavior and the response to the excavation progress is presented.

***Part II***: The anisotropic closure evolution of different drifts, excavated at the M/HM URL, is analyzed based on a direct analysis of the convergence measurements using the semi-empirical law proposed by Sulem et al. (1987). The influence of the different excavation and support methods, of the size and of the rate of excavation on the anisotropic closure of the drifts are studied. The analysis is performed taking into account the effect of the following parameters on the time-dependent behavior of the ground: the direction of excavation (i.e. influence of the initial stress state), the excavation size (from 0.7 m to 6.3 m), the supports systems and time delayed for its installation, the excavation rate and also the influence of the drift cross section enlargement. The analysis is extended to the study of the radial displacements of the ground around the drifts recorded by the extensometers. This extensive treatment of the recorded data allows for reliable predictions of the convergence evolution in the long term. Based on the data obtained by the monitoring of supports, the interaction between the rock mass and support is analyzed. It is shown that this approach can provide useful information for the design of supports.

***Part III***: One important point to analyze is the role of hydromechanical couplings on the anisotropic response of the rock formation. Considering the in-situ observations of an anisotropic pore pressure field around drifts, the main goal of this part is to analyze the pore pressure evolution induced by drifts excavation. This is done by means of a fully coupled 2D finite element simulation in the framework of anisotropic poroelasticity. The objective is to simulate the main trends of the pore pressure evolution with a simple model taking into account the inherent anisotropy of the material. Special attention is paid to the drifts following the direction of the major principal horizontal stress, where even with a quasi-isotropic initial stress state in the cross section of the drift, the pore pressure field and the mechanical response are anisotropic. These observations indicate that the intrinsic anisotropy of the material plays a key role in the coupled

response of the rock formation. Finally, an analysis of the onset of failure demonstrates the importance of the hydro-mechanical coupling on the extension of the failed zone around the drifts.

# PART I: ANDRA's PROJECT

In 2000, the French National Radioactive Waste Management Agency (Andra) began the construction of the Meuse/Haute-Marne Underground Research Laboratory (M/HM URL) at Bure (East of Paris sedimentary basin) with the main goal of demonstrating the feasibility of geological repository in Callovo-Oxfordian claystone. Several research programs have taken place to improve the knowledge of the rock properties and its response to the excavation progress. A full understanding of the short and long-term response of the rock mass formation and the interaction with the support system is important to optimize the design of nuclear waste repository in claystone host rock (Noiret et al. 2015). To this aim, a network of experimental drifts (with diameters ranging between 4 m and 9 m) has been excavated with different choices on: the excavation method, the structure geometry, the supports system and the orientations with respect to in-situ principal stresses' directions. Then, from these experimental drifts, micro-tunnels (with a diameter of about 0.7 m) have been excavated to test the feasibility of disposal cells for high level waste (HLW) and Intermediate level - Long lived (IL-LL) waste packages and its impact on the surrounding rock (Renaud et al. 2010). Fig.1.1 presents the network of drifts excavated until now and the projection for the currently year. It should be noted that, at the main level of URL, most of the drifts are excavated following horizontal principal stresses.
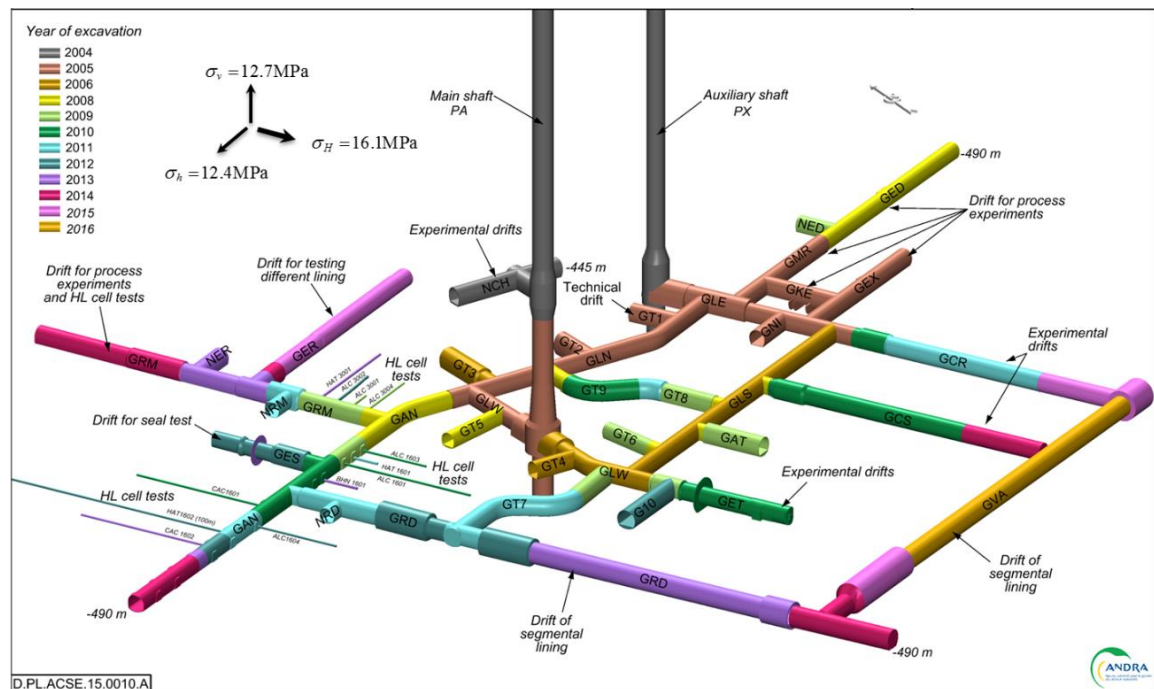


**Fig. 1. 1.** URL drifts network 2004-2016 (from Seyedi et al. 2016)

In each drift, different sections have been instrumented to monitor and characterize the excavation-induced deformation and the hydromechanical response of the rock mass formation during and after excavation. Continuous monitoring of the excavated zone around the drifts revealed the development of a fractured zone (extensional and shear fractures) induced by the excavation. The extent of this fractured zone depends mainly on the drift orientation regarding the in-situ stress field (Armand et al. 2014). Indeed, for the drifts excavated along the major principal horizontal stress ($\sigma_H$) the fracture network is developed mainly in the horizontal direction of the cross section, while for the drifts excavated along the minor principal horizontal stress ($\sigma_h$), it is mainly developed in the vertical direction. The fractures' distribution has an important influence on the convergence of the drifts. The measurements show an anisotropic closure, which depends on the drifts' orientations and an evolution in time of the deformation. For the drifts excavated along $\sigma_H$, the ratio of the vertical closure to the horizontal one is about 0.5, whereas it is about 4 for the drifts excavated along $\sigma_h$ (Armand et al. 2013). Moreover, the field monitoring during the excavation showed marked overpressures and an anisotropic pore pressure field around the drifts.

The main goal of Part I of this thesis is to give a detailed description of the characteristics of the Callovo-Oxfordian claystone (section 1.1), the in-situ stress state (1.2) and of the excavations and supports methods used in the construction of the different experimental drifts at the URL (section 1.3). We shall also present an overview of the drifts installations and the set up for the hydro-mechanical measurements performed at the URL (section 1.4), of the in-situ observations (section 1.5) and of the existing models for the characterization of the rock mass behavior and the response to the excavation progress (section 1.6).

## 1.1. The Callovo-Oxfordian claystone

The Callovo-Oxfordian Claystone (COx) is an argillaceous formation, lying between depths of 420 and 550 m in Meuse/Haute-Marne region in France (Fig. 1.4). This formation is interbedded between Dogger limestone formation (224 m thick layer below) and Oxfordian limestone formation (212 m thick layer above), all of which are sub-horizontal (dip smaller than 3°) (Cornet et al. 2012). The COx claystone has been studied for more than one decade as a potential host formation for High level (HL) and Intermediate level - Long lived (IL-LL) nuclear waste. Considering its very favorable characteristics like a very low hydraulic conductivity, a small molecular diffusion and a significant retention capacity for radionuclides (Andra 2005, Armand et al. 2013) it is considered as a reliable host rock formation. Some principal characteristics of the COx are summarized in this section.

### *1.1.1. Mineralogical composition and microstructure*

In the literature the mineralogical composition for the COx claystone is presented by several authors (e.g. Sammartino et al. 2003; Yven et al. 2007; Robinet et al. 2008) and have been studied taking into account different scales of interest (i.e. microscopic [$< \mu m$], mesoscopic [$\mu m - cm$], macroscopic [$cm - dm$], and formation scale [$> dm$], Robinet 2008 and Andra 2013b). As explained by Gaucher et al. (2004) and Andra (2005), the mineralogical composition of the host rock varies slightly within the stratigraphic levels.

The mineralogical composition at the main level of the URL (-490 m) is presented in Table 1.1. The clay minerals composition is relatively constant with 55 % I/S (illite–smectite interstratified minerals), 30% illite and 15% kaolinite and chlorite. Fig. 1.2 presents a three-dimensional distribution of minerals groups in the COx claystone, based on the observations obtained from the X-ray tomography (Robinet et al. 2012).

**Table 1. 1.** Mineralogical composition at the main level of the URL (Gaucher et al. 2004; Andra 2005)

| | |
|---|---|
| Tectosilicates | 20 % |
| Carbonates | 20 - 25 % |
| Clay minerals | 50 - 55 % |
| Subordinate pyrite and iron oxides | 3 % |
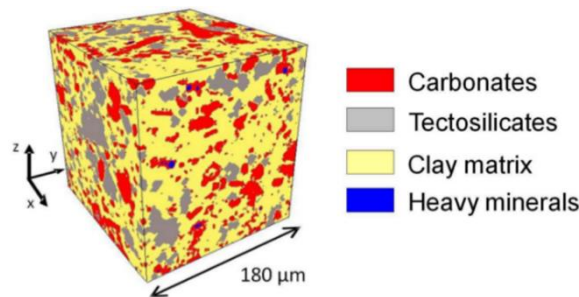


**Fig. 1. 2**. Mineral groups distribution of the Callovo-Oxfordian Claystone, obtained from X-ray tomography (from Robinet et al. 2012)

Studies on the Callovo-Oxfordian claystone microstructure (e.g. Chiarelli 2000; Sammartino et al. 2003; Yven et al. 2007; Song et al. 2015; Robinet JC et al. 2015) show a very small mean pore diameter of about 0.02 μm. Therefore, the claystone has a low permeability ($\approx 5 \times 10^{-20}$ to $5 \times 10^{-21}$ m$^2$) at the main level of the URL. The rock porosity at this level is between 14 and 21% with an average of 18±1%. Natural water contents of core samples range between 5 and 8%.

### 1.1.2. *Hydro-mechanical behavior*

The hydromechanical characterization of the Callovo-Oxfordian claystone is presented in the literature by several authors (e.g. Chiarelli 2000; Chiarelli et al. 2003; Escoffier et al. 2002; Bemer et al. 2004; Homand et al. 2006; Hoxha et al. 2007a; Hu et al. 2014; Menaceur et al. 2016). The main characteristics of the Callovo-Oxfordian claystone at the main level of the M/HM URL are presented in Table 1.2.

**Table 1. 2.** Characteristics of the Callovo – Oxfordian claystone at -490 m (adapted from Armand et al. 2014)

| | | |
|---|---|---|
| *Microstructure and hydraulic properties* | Mean pore diameter | $\approx 0.02$ μm |
| | Porosity | $18 \pm 1$ % |
| | Water content | 5 and 8 % |
| | Permeability | $\approx 5 \times 10^{-20}$ to $5 \times 10^{-21}$ m$^2$ |
| | Solid grains density | 2.39 g/cm$^3$ |
| *Poroelastic properties* | Young modulus | $4000 \pm 1470$ |
| | Poisson ratio | $0.29 \pm 0.05$ |
| | Biot's coefficient | 0.60 |

Sedimentation has led to a slightly anisotropic behavior of the claystone. As explained by Blümling et al. (2007), the anisotropy might be caused by diagenetic processes or metamorphism, leading to planes of weakness (bedding planes) in the rock. Therefore, this kind of formation have properties that vary with direction and are said to be inherently anisotropic (Amadei 1983 and 1996). Compressive and shear wave measurements on cubic samples and also triaxial tests have exhibit an elastic anisotropy. The anisotropy ratio of the dynamic Young's Modulus varies between 1.2 and 2.0 (Armand et al. 2013 and 2014). It has also been observed that the uniaxial compressive and tensile strengths depend of the orientation with respect to the bedding planes (about 17.8 MPa and -1.5 MPa for uniaxial compressive and tensile strength parallel to bedding planes; and about 19.9 MPa and -1.2 MPa perpendicular to bedding planes, from Andra database).

Concerning the Biot's effective stress coefficient, in the literature one can find a rather large range of values (between 0.3 to 1) for the Callovo-Oxfordian claystone as determined in laboratory experiments (e.g. Vincké et al. 1998, Escoffier 2002, Bemer et al. 2004, Pham 2006, Belmokhtar et al. 2016). In addition to the natural variability of the tested samples, this discrepancy can be attributed partly to different initial saturation conditions of samples and also different loading rates in the performed experiments. However, the average value of the Biot's coefficient, commonly preconized for the Callovo-Oxfordian Claystone, is about 0.6 (Jia et al. 2008, Charlier et al. 2013, Plassart at al. 2013, Pardoen et al. 2015a).

*Short- and long-term behavior*

As presented by Armand et al. (2013) and Armand et al. (2016), the short- and long-term behavior of the Callovo-Oxfordian claystone can be summarized as:

(1) For the short-term behavior, triaxial compression and extension tests have been performed. Fig. 1.3a shows typical experimental results obtained from triaxial compression tests. A linear response is observed under low deviatoric stress. The onset of damage which can be associated with the loss of linearity can be estimated at about 50 % of the peak stress. A brittle failure of the samples is observed under low confining pressures, which has been evidenced by the formation of an inclined shear band. By increasing the confining pressure, the rock behavior changes progressively from brittle to ductile. The transition confining pressure can be estimated to 20 MPa. Finally, it has been observed that the claystone presents a rather brittle behavior under tensile loading.

(2) The long-term behavior of the rock has been experimentally explored by performing creep tests. Fig. 1.3b presents the results obtained from uniaxial creep tests under multi-step uniaxial load (Zhang et al. 2010). The load has been applied upwards to 4, 7, 10, 13 MPa and downwards to 10 and 7 MPa. In the case of loading stages, it is observed that the strains increase gradually with time. Then, all the creep curves present a transient phase with decreasing strain rates during the first 2 – 3 months. Finally, a quasi-stationary phase with a relatively constant strain rate is observed. In the case of unloading stages, the creep strain evolves firstly with negative rates (as show in the right of the Fig. 1.3b) and then it tends to returns to a positive rate with time. Creep rates of about $2\times10^{-11}\text{s}^{-1}$ to $6\times10^{-11}\text{s}^{-1}$ have been observed during the loading phases, whereas lower rates of about $1\times10^{-11}\text{s}^{-1}$ to $2\times10^{-11}\text{s}^{-1}$ have been observed during the unloading phases. Similar observations have been performed in works of Gasc-Barbier et al. (2004) and Fabre et al. (2006). The experimental results presented in Fig. 1.3b have been obtained by applying the axial load perpendicular to the bedding plane. However, sample EST25321 (see Fig. 1.3b) has been axially loaded parallel to the bedding plane. It is observed that the strain evolution curves are relatively parallel, suggesting little anisotropy of the viscous deformation in the claystone, as explained by Zhang et al. (2010).

The deformation behavior of the COx has been widely studied based on laboratory experiments under various THM conditions (e.g. Zhang and Rothfuchs 2004, Zhang et al. 2010, Zhang 2015, Armand et al. 2016). However, one open question which is under study, is which mechanisms at the micro-scale control the time-dependent behavior of the rock. Studies performed until now show that the bound porewater has an important role in the rock deformation. The creep of the

clay matrix, sub-critical propagation of micro-cracks and swelling of some of the clay minerals can be at the origin of the observed time-dependent behavior.
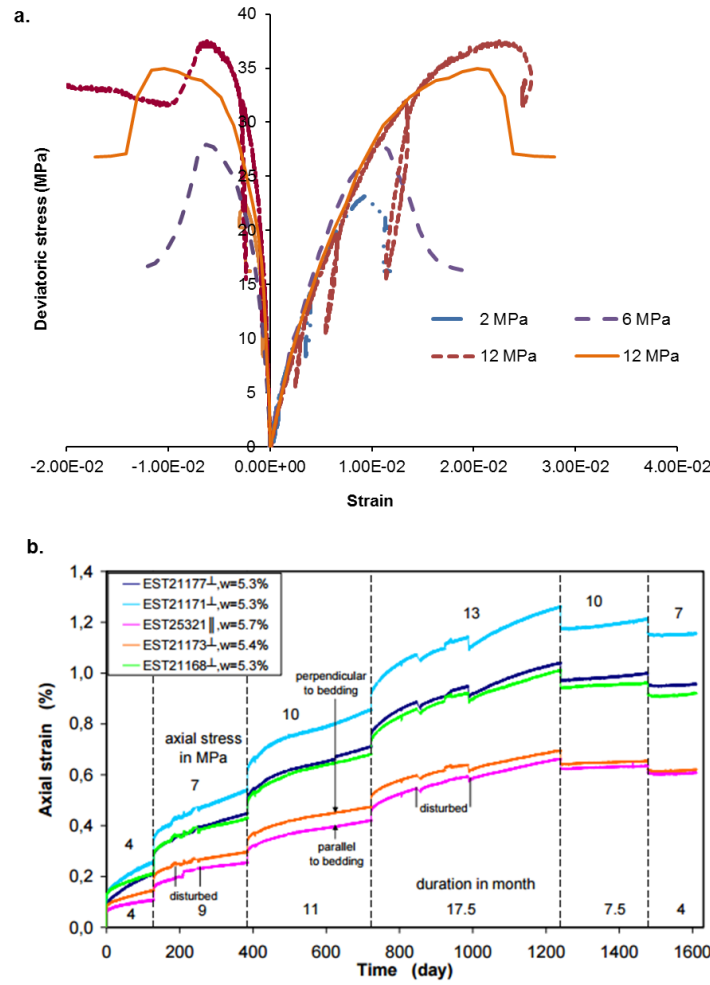


**Fig. 1. 3.** Results obtained from different samples of Callovo-Oxfordian claystone: a. Triaxial tests (from Armand et al. 2016). b. Uniaxial creep tests (from Zhang et al. 2010)

## 1.2. In-situ stress state

Several techniques have been applied for the determination of the stress field in the rock formation at the M/HM URL. They include hydraulic tests in vertical and inclined boreholes and borehole imaging. Hydraulic fracturing tests are commonly performed in order to estimate the value of the minimum principal stress. Then, as explained by Wileveau et al. (2007), based on a linear isotropic elastic analysis and the concept of effective strength (Haimson, 1993), the major horizontal principal stress magnitude has been calculated. In complement sleeve fracturing tests and a systematic analysis of the breakouts observed in boreholes have been performed to better assess the knowledge about the in-situ stress state.

The obtained results have been validated by the analysis of the convergence evolution during the excavation of the main shaft (with a diameter of about 6 m) used for accessing the URL. As explained by Wileveau et al. (2007), on the basis of a plane strain elastic back analysis of the measured convergence, the difference between the principal horizontal stresses has been evaluated together with the determination of the orientation of the maximal horizontal stress. Stress directions and magnitudes as obtained from different tests performed are in good accordance. As explained by Cornet et al. (2012), the stress magnitudes do not vary linearly with depth. In fact, the vertical variations are controlled by the rheological characteristics of various formations. Therefore, the ratio of anisotropy between the major and minor principal horizontal stresses vary with depth, as explained by Wileveau et al. (2007). Fig. 1.4 summarizes the results of the complete stress determination presented by Gunzburger and Cornet (2007) and Wileveau et al. (2007).
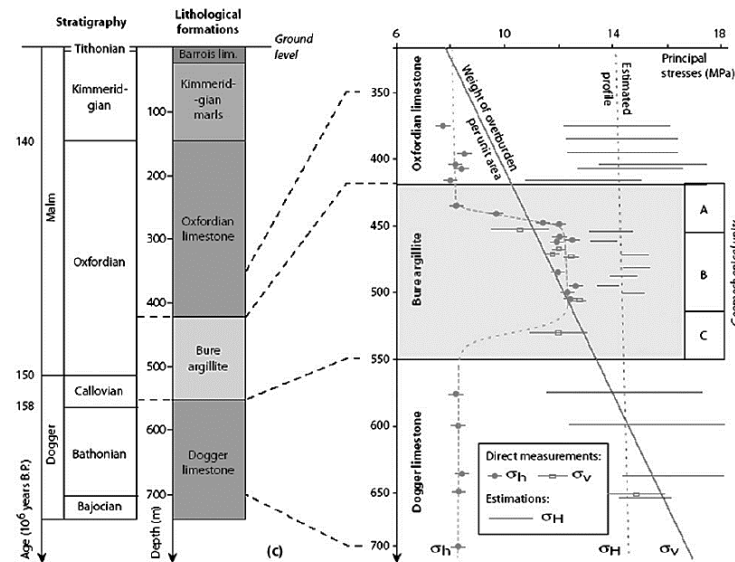


**Fig. 1. 4.** Stress determination results at the M/HM URL (from Cornet et al. 2012)

At the main level of the M/HM URL (i.e. -490 m), the major principal horizontal stress is considered to be about 16.1 MPa[1] and is oriented in the direction N155°E $\pm$ 10°, while the minor principal horizontal total stress is very close to the vertical stress, 12.4 MPa and 12.7 MPa respectively. The pore pressure at the main level (-490 m) is around 4.7 MPa.

---

[1] The major horizontal principal stress value presents uncertainties because of its estimation is based on indirect methods, whereas the minor horizontal and vertical principal stresses are measured.

## 1.3. Excavation and support methods installed at the URL

One of the main objectives of the M/HM URL is to study and compare the influence of different excavation methods and different support systems on the rock response. In this section an overview of the excavation methods and supports systems implemented at the URL is presented.

### 1.3.1. Excavation methods

For drifts (4 to 9 m of diameter), the excavation was carried out by three different techniques. Most of the drifts have been excavated by two conventional techniques: the pneumatic hammering machine (Fig. 1.5a) and the road header machine (Fig. 1.5b). More recently, the excavation was carried out by a road header under shield with segments emplacement technique (Fig. 1.5c). It should be noted that a full face tunnel boring machine (TBM), which could be used for access drifts in the repository, could not be used at the URL due to the small size of the shaft and low capacity in size and load of the freight elevator (Armand et al. 2015a).
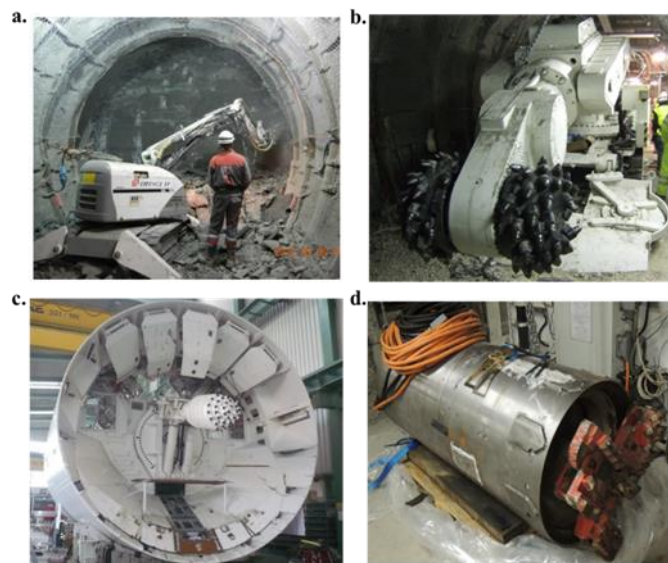


**Fig. 1. 5.** Different excavation methods: a. Pneumatic hammering machine. b. Road header machine. c. Road header under shield machine. d. Micro-tunnel boring machine

For micro-tunnels ($\approx$ 0.7 m of diameter), the excavation was carried out by a micro tunnel boring machine, which has a drilling head that can be adapted to excavate diameters of 70 to 75 cm (Fig. 1.5d). This tailor-made machine is laser-guided, which allows the control of the micro-tunnel trajectory with a precision higher than +/- 2 cm, preventing vertical and horizontal deviation during excavation. Moreover, this machine has been conceived to meet with some specific constraints of the digging as: using air drilling without fluid, limit the induced damage in the rock

and the possibility of removal from the liner place at the end of excavation by rotation in the opposite direction. Therefore, different tests performed for the excavation of micro-tunnels will allow to improve the micro tunnel boring machine gradually.

The comparison of different excavation techniques and supports allow to better understand the response of the rock formation to the excavation progress and also the time-dependent behavior of drifts. To this aim, the progress of the experimental drifts excavation is performed taking into account different configurations (in type of support and time delayed for the installation of the support):

- The first drifts have been excavated and supported by a flexible support in order to analyze the behavior of rock mass formation induced by the excavation progress.
- Then, the installation of a rigid permanent lining in some drifts has been tested some months after the passage of the tunnel face.
- Finally, the installation of a rigid support after the passage of the drift face has been also tested.

### 1.3.2. Support methods

The experimental program has been established in a sequential progress. The first excavations have been performed for drifts following the direction of the major principal horizontal stress ($\sigma_H$), with the installation of a flexible support. Then, different supports types have been tested and the time of their installation has been modified. The experimental excavation program has then been extended to drifts excavated following the direction of the minor principal horizontal stress ($\sigma_h$). Finally, a new methodology of excavation is performed by Road header under shield, as explained above. In that case, a new type of rigid support has been tested. In this section an overview of the two types of support (i.e. flexible and rigid) are described. Fig. 1.6 and Fig. 1.7 summarize the distribution of support installation on different drifts of the M/HM URL.

#### 1.3.2.1. <u>Drifts support</u>

<u>Flexible support:</u>
The flexible support is mainly composed of radial bolts (about 12 bolts type HA25 of 3 m length, installed around the perimeter of the drift cross section), a small thick layer of fiber shotcrete (of about 10 cm to 20 cm) and welded mesh. Then, depending on the drift, the support can be composed of yieldable concrete wedges (e.g. GCS drift – *Galerie de Conception Souple / Flexible*

*design drift*, Bonnet-Eymard et al. 2011), or of sliding arches installed every meter (e.g. GED drift – *Galerie Expérimentale Deux / Experimental drift*). These supports can accommodate the rock mass deformation and allow for the ground deconfinement (Fig. 1.6). Indeed, as explained by Anagnostou and Cantieni (2007), one of the technical options is the installation of a yielding lining in contact with the excavation face, which will deform with the rock. Therefore, the flexible support allows to accommodate deformation without damage to the lining.
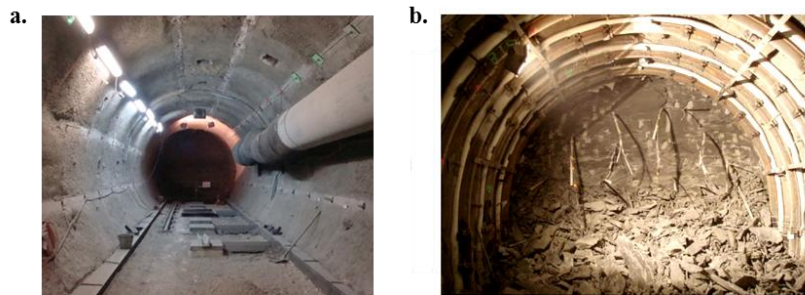


**Fig. 1. 6.** Flexible support installation: a. Support with yieldable concrete wedges (GCS drift). b. Support with sliding arches (GED drift)

Rigid support:

The rigid support (Fig. 1.7) is mainly composed of radial bolts (about 12 bolts type HA25 of 3 m length, installed around the perimeter of the drift cross section) and welded mesh, as for drifts with flexible support together with a thick layer of fiber shotcrete that can vary from 20 cm to 45 cm. The installation of a support of 45 cm permits to rapidly block the convergence evolution (e.g. BEP drift – *Béton Projeté Epais / Thick shotcrete*).

Special testing has been performed for a drift with a flexible support composed of about 20 cm thick layer of fiber shotcrete and yieldable concrete wedges, as explained above (e.g. GCR drift – *Galerie de Conception Rigide / Rigid design drift*). Then, about 7 months after the installation of the flexible support, a permanent stiff lining has been installed (about 27 cm thick layer of concrete). Two types of concrete have been tested, for the final lining, in two different sections along the drift: C60/75 and C30/37 (concrete classification based in its compression strength).

The support installed for the drift excavated by Road header under shield is only composed of prefabricated segments approximately 45 cm thick, with radial injection of mortar of about 13.5 cm. Each support ring is composed of 9 prefabricated segments of about 0.80 m length. The type of concrete used for the fabrication of the segments is C60/75 (e.g. GRD4, experimentation TPV – *Tunnel avec Pose de Voussoirs / Lining Segmental Tunnel*).

**Fig. 1. 7.** Rigid support installation: a. Support of 45 cm of fiber shotcrete (BEP drift). b. Support with 20 cm of fiber shotcrete and a permanent lining installation 7 months after (GCR drift). c. Support composed of rings of prefabricated segments (GRD4 drift)

### 1.3.2.2. *Micro-tunnels support*

The French concept for High Level activity waste (HLW) consists of cased horizontal micro-tunnels with a diameter of about 0.7 m. Demonstration of the feasibility of excavation started in 2009 (Morel et al. 2010). Micro-tunnels have been excavated with lengths varying between 20 to 40 m. The excavation has been achieved with or without casing (Fig. 1.8). The casing is made of segments of 2 m long, 70 cm in diameter and 2 cm thick metal tubes. The 2 m long elements are welded or socketed to each other as the excavation advances (Morel et al. 2013). The unsupported micro-tunnels permit to follow the formation of breakouts (Fig. 1.8b) and also, to follow the state of the micro-tunnels' walls and their evolution with time.
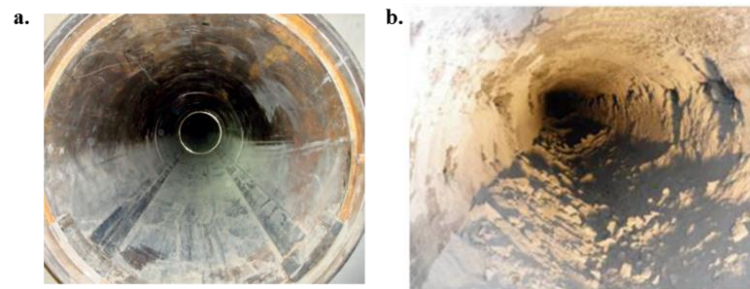


**Fig. 1. 8.** Micro-tunnels after excavation. a. with casing. b. without casing

## 1.4. Geotechnical instrumentations set up in the M/HM URL

The response of the rock formation has been monitored by instrumenting several sections for convergence measurements of the drifts' walls. Some sections are also equipped with extensometers and extrusometers. Extensometers are used to monitor radial displacements around the drift whereas extrusometers (known also as reverse head extensometers) are used to monitor longitudinal displacement ahead of the tunnel face. Moreover, a continuous monitoring of the

pore pressure change around drifts has been performed. The response of the different supports installed at the URL is also monitored. The continuous monitoring of the rock and the interaction between the rock mass and the support can provide useful knowledge about the rock response during and after excavation, which is a key issue for the repository design and safety. Furthermore, as explained by Armand et al. (2015b), understanding the impact of support and excavations methods on the hydromechanical behavior of drifts in the short and long-term is necessary to optimize the design of the support.

### 1.4.1. Convergence measurements

*Along the drifts*

Convergence measurements have been carried out in several sections. Six monitoring points located in a plane normal to the drift axis have been installed in each section. Measurements of wall movements are recorded along five different strings, which connect these points as shown in Fig. 1.9. The distribution of these strings permits to monitor the global deformation of the drift in vertical, horizontal and transverse directions. In general, these monitoring points are installed at an initial distance of about 2 m from the tunnel face. A detailed description of the convergence measurements is presented in Part II of this dissertation.
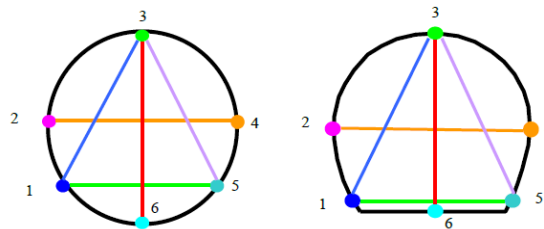


**Fig. 1. 9.** Convergence measurement sections for two different drift geometries

*Along the micro-tunnels*

Convergence measurements have been performed using a specifically designed system, which permits measurements with an accuracy of 0.1 mm, as described by Gay et al. (2010). This system is installed in four convergence measurement sections placed at 4 to 8 m from each other, depending on the length of the micro-tunnel. It permits a long-term monitoring of walls closure and also, the identification of the breakout zones. Measurements are taken in the vertical, horizontal and transverse directions as shown in Fig. 1.10.
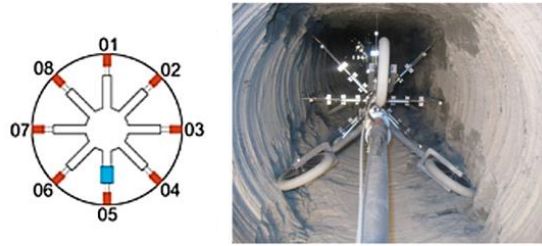
**Fig. 1. 10.** Instrumentation of a convergence measurement section in ALC1603 micro-tunnel. At left: schematic picture of the convergence measurement section (SMC). At right: Photo of the installation of the SMC. The convergence measurements are performed in the vertical (01-05), horizontal (03-07) and transverse (02-06 and 04-08) directions

### 1.4.2. Extensometer measurements

The radial displacements of the ground around the drifts have been followed by the installation of borehole extensometers, as a complement to the convergence measurements. The extensometers provide useful information about the deformation distribution inside the rock mass and its evolution with time. Two groups of borehole extensometers can be distinguished. One group has been installed along the drifts during the excavation progress in sections called 'reinforced measurement sections (SMR)', and the other group has been installed before the beginning of the drift excavation as a part of mine-by tests.

*Extensometer measurements in reinforced measurement sections*

In one or two sections along the drift (the so-called reinforced measurement sections (SMR-*Section de mesures renforcée*)), four multi-position borehole extensometers about 30 m long and four mono-position boreholes about 1 m long have been installed. In Fig. 1.11 is shown the installation of SMR in GCS drift (multi-position borehole extensometers are denoted OHZ1707, OHZ1704 for the vertical ones and OHZ1703, OHZ1705 for the horizontal ones; and also, the mono-position borehole extensometers are denoted OHZ1782, OHZ1784 for the vertical ones and OHZ1783, OHZ1785 for the horizontal ones). As for the convergence measurements, these extensometers are installed close to the tunnel face at a distance of about 1.5 to 2.0 m. The variations depend on various factors such as the size of the drilling machine, the installation of the temporary invert and the works to secure the tunnel face.

Multi-position borehole extensometers have usually seven points of measurement at different depths from the drift wall. Their distribution (between 1 and 30 m) allows to follow the rock mass response around the drift and to highlight the area where the stronger deformation is developed. However, these extensometers installed after the excavation of the section give only a partial knowledge of the deformation of the rock mass due to the face advance. Complementary

information can be obtained from the extensometers installed before the beginning of the excavation as explained below.
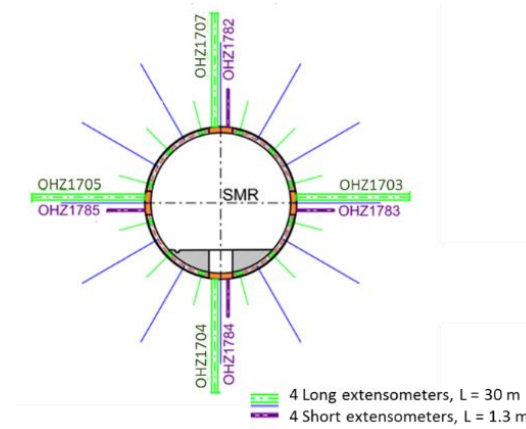


**Fig. 1. 11.** Extensometers in a reinforced measurement section: example of GCS drift

*Extensometers of mine-by experiments*

Mine-by experiments have been performed in an attempt to characterize the excavation-induced deformation and the hydro-mechanical response of the rock formation during and after excavation (Armand et al. 2011). Similar experiments have been implemented in other clayey rocks, e.g. the ED-B experiment in Opalinus clay (Martin et al. 2002 and Corkum and Martin 2007); the CLIPEX experiment in indurate Boom clay (Bernier et al. 2003).

At the main level of the URL (i.e. -490 m), several types of measurements have been performed for the characterization of the fractured zone around the drifts. The mine-by test was emplaced in three different drifts following the direction of $\sigma_H$ as shown in Fig. 1.12. It is composed by 15 boreholes: 3 extensometers, 3 inclinometers and 9 boreholes devoted to the measurement of pore pressure. A detailed description of these experiments can be found in Armand et al. (2011) and Noiret et al. (2011).

The extensometers of mine-by tests permit to follow the deformations of the rock mass induced by the excavation progress and their evolution in time. The instantaneous response can then be separated from the long-term response as explained in Part II of this dissertation.
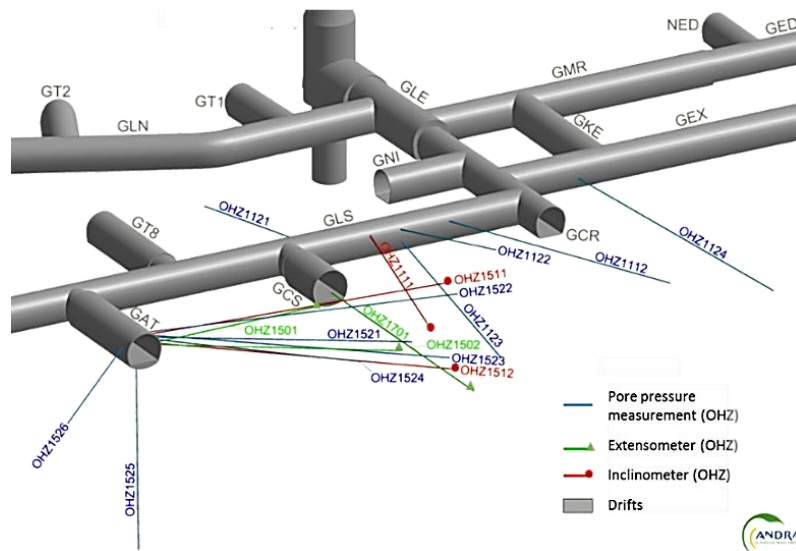
**Fig. 1. 12.** Instrumentation of mine-by experiment (Armand et al. 2011)

### 1.4.3. Extrusometers

Extrusometers, known also as reverse head extensometers, are used to monitor longitudinal displacement ahead of the tunnel face. These ones are composed of mono-position extensometers joined together by sliding connections and have been drilled in the axis of some drifts in order to have a continuous monitoring of the axial displacements of the face during excavation. The installation is shown in Fig. 1.13. The head of the extrusometer records longitudinal displacements between different points, situated at various distances up to 20 m ahead of the face. This device installed at the end of the borehole is destroyed by the excavation progress. Thus, measurements are performed even if the sensors are being successively destroyed during advancing excavation, as explained by Steiner (2007).
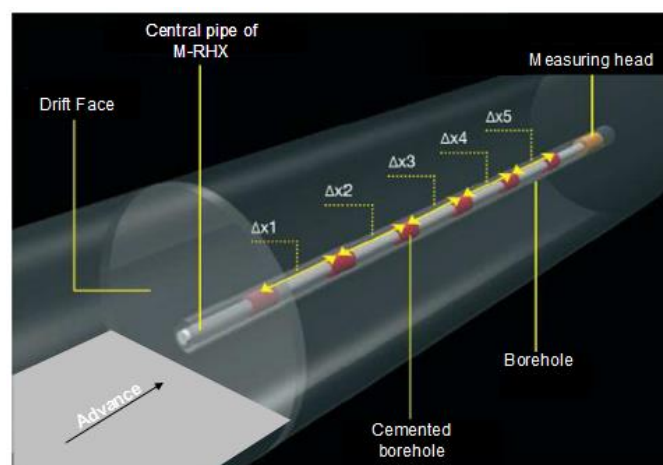


**Fig. 1. 13.** Reverse head extensometer installation

### 1.4.4. *Pore pressure and permeability measurements*

Boreholes devoted to the pore pressure measurement have been installed before the beginning of drift excavation as a part of mine-by-test, as explained above. Pore pressure measurements have been instrumented at least two months before the drift excavation, to let the pore pressure to build up and to stabilize (Armand et al. 2015a).

A specific multi-packer system called the Pore pressure system (PP system) has been used for the pore pressure monitoring in boreholes up to 60 m from the drift wall (Fig. 1.14). This is a designed system furnished by Solexperts AG, which allows to have 5 measurement intervals in the same borehole (Armand et al. 2015b). As explained by Fierz et al. (2007), each 10 to 20 cm long interval has two stainless steel lines connected to a control panel placed in the drift. A pressure sensor mounted on one of the stainless steel line allows the continuous monitoring of variations in pressure, while the other line allows the running of hydraulic tests (pulse, injection, production). The volume of the chamber is reduced as much as possible in order to assure the rapid stabilization of pressure. Moreover, a section of resin in the annulus of the borehole is used to insulate each interval. The resin ensures long-term stability as well as very low system compressibility.

In order to prevent leakage in the fracture and change of transmissivity of the fractures network, a system called Mini-Multi-Packer-System (MMPS) is used in boreholes shorter than 9 m as a complement of the PP system (mainly used beyond the EDZ zone), as explained by Armand et al. (2015b). The system is similar to the PP system except that each chamber is isolated by a packer inflated with water. The rigid packers limit the compressibility. This system provides 5 to 6 chambers 10 to 20 cm in length. A detailed description of these measurements systems is presented in Fierz et al. (2007) and Armand et al. (2015b).



**Fig. 1. 14.** Measurement chamber of a PP system (from Armand et al. 2015b)

### 1.4.5. *Support Installation monitoring*

The monitoring of the support behavior is performed in different measurement sections installed along the drifts. In general, for the shotcrete and concrete behavior, the monitoring of the hoop strain is performed by vibrating wire strain gauge (total of 13 gauge distributed around the cross section), which are designed for non-dynamic measurements and present long-term stability and reliability. It should be noted that in each measurement section, one gauge located at the roof of the drift is isolated (no loaded) in order to try to correct measured deformation from thermal and drying effects, induced by the concrete poured. This means that the deformations recorded in this gauge are directly related to the intrinsic behavior of the support material. This gauge is used as a reference gauge for the corrections performed in the measurements recorded in the other 12 gauges in the section. Moreover, the monitoring of the hoop stress is performed by using total pressure cells (or flat jack in the shotcrete case), which are installed at four different angles of the drift cross section. For the support containing yieldable concrete wedges, two instrumented sections with 4 extensometers (potentiometers) and 4 total pressure cells (vibrating wire) have been installed along drifts. Fig. 1.15 presents a measurement section for a support with yieldable concrete wedges.
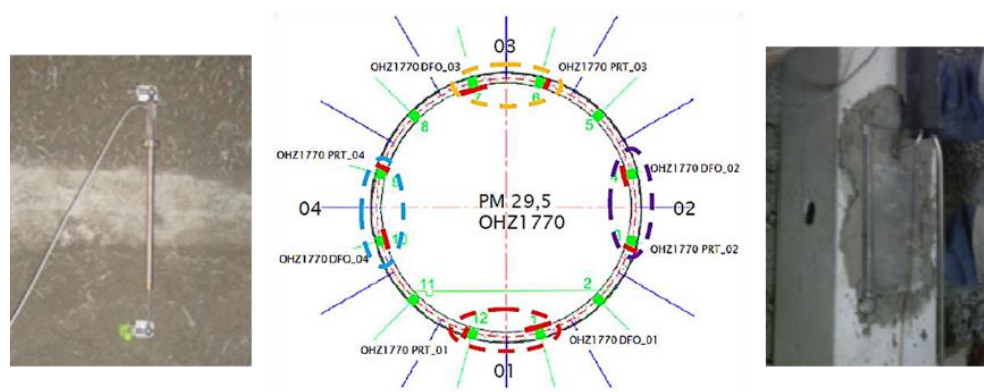


**Fig. 1. 15.** Measurement section to follow the yieldable concrete wedges. The gadgets have been installed in four different zones around the drift cross section. Each zone is composed of one potentiometer (left) and one pressure cell (right)

For the drifts having a support composed of prefabricated segments (e.g. GRD4 drift), the measurements gadgets have been installed into the segments during their fabrication, as shown in Fig. 1.16. Four different rings of segments have been instrumented along the drift. Each ring is composed of nine segments among which eight are instrumented. This means that, for each ring, a total of 64 deformation measurements by vibrating wire extensometers (i.e. 4 measurements of hoop deformation, 2 of radial deformation and 2 of longitudinal deformation in each segment) and 24 stress measurements by total pressure cells (i.e. 2 measurements of hoop stress and 1 of radial

stress at the extrados in each segment) are recorded. It should be noted that one control segment, which is not loaded, is used as a reference segment for the corrections performed in the measurements with respect to the concrete shrinkage.



**Fig. 1. 16.** Implementation of measurements gadgets in the segments before the concrete is poured

## 1.5. In-situ observations

As explained above, most of the drifts have been instrumented to follow the response of the rock mass formation to the excavation progress and the interaction between the rock mass and the support. In this section, a description of the different in-situ observations is presented. It should be noted that attention is mainly focused on the fracture network distribution around the drifts. The evolution of the convergence, the deformation and the pore pressure around the drifts will be presented in more detail in Parts II and III of the dissertation.

### 1.5.1. Fracture network distribution induced by drifts excavation

Stress redistribution induced by the excavation of drifts results in the development of a fracture network around the opening section, which can affect the hydromechanical response of the rock mass formation, as explained by Armand et al. (2014).

Due to the favorable confining conditions for repository of radioactive waste, this argillaceous formation is considered as a reliable host rock. However, as explained by Armand et al. (2014), the disturbance and damage induced by the excavation, in the area around drifts, might change the favorable properties of the rock mass formation and affect its barrier functions. Therefore, a good knowledge of the fractured zone (type of fractures, orientations, extension, hydro-mechanical behavior…) around the excavations is required for the repository safety assessment. Furthermore,

as explained by Seyedi et al. (2016), the extent of the fractured zone has a direct impact on the load transferred to the drift's support. The extent and nature of the fractured zone affects in this manner the support system design. The characterization and analysis of the induced fracture network have been performed by several methods in the URL (Armand et al. 2007 and 2014):

- Structural analysis of the core samples drilled from the drifts
- Geological survey of the drift face and sidewalls (three-dimensional scan measurements)
- Seismic measurements (evaluation of the change of P and S wave velocities due to damage)
- Permeability measurements
- Overcoring of resin-filled fractures

It should be noted that no structures with tectonic origins have been observed at the URL. The observed network of fractures is mainly induced by the excavation progress of drifts and micro-tunnels, as explained by Arnould et al. (2016).

All drifts excavated at the main level showed induced fracture networks. The shape of fracture network depends on the orientation of the drift with respect to the in-situ stress field. Moreover, it is observed that the extent of the fractured zone follows a similar pattern for different drifts diameters. The shear fractures represent 75% of the total fractures developed around drifts in the two directions of excavation. Therefore, a conceptual fracturing model has been proposed for drifts in both directions of excavation (Fig. 1.17), following the direction of $\sigma_H$ and following the direction of $\sigma_h$ (Armand et al. 2014):

### *Drifts following the direction of $\sigma_H$ :*

It is observed an extension of fractures which is more developed in the horizontal direction of the drift cross section, with a distribution of mixed fractures (extensional and shear fractures) near the drift wall and an extension on only shear fractures until about 0.8 times the diameter of the drift (Fig. 1.18). In the vertical direction, it is observed only a distribution of mixed fractures until about 0.1 times the diameter. A schematic view of the fracture distribution obtained around drifts of 5 m diameter is presented in Fig. 1.17a. It should be noted that similar observations have been made for excavations with different sizes: around a borehole of 5 cm diameter and around a micro-tunnel of 0.7 m diameter, showing that the lateral extent of shear fractures is almost equal to 1 diameter of the excavation.
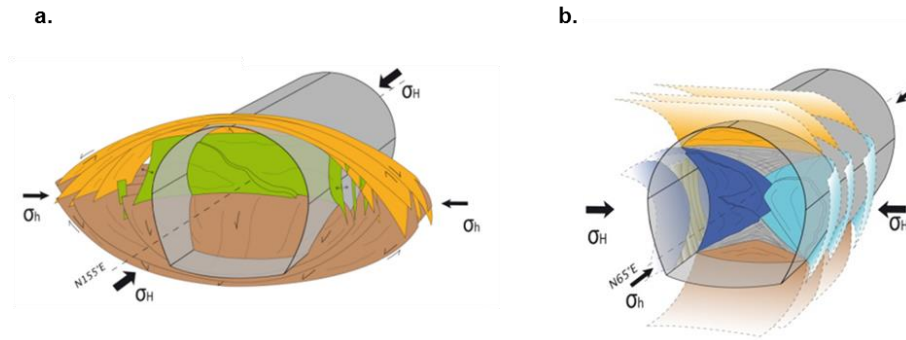
**Fig. 1. 17.** Fractured zone induced by the excavation: a. for drifts parallel to $\sigma_H$ - N155°E. b. for drifts parallel to $\sigma_h$ – N65°E (from Armand et al. 2014)
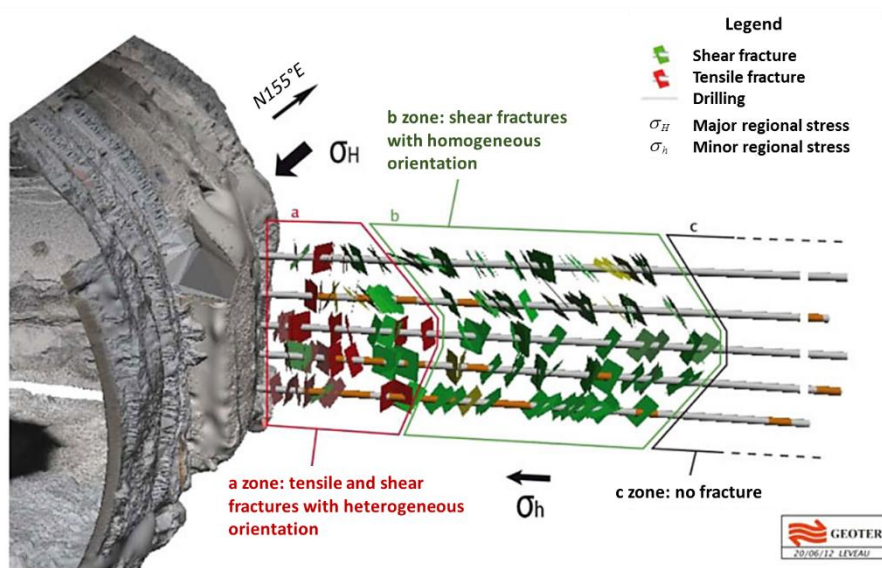


**Fig. 1. 18.** 3D visualization of fractures network for drifts parallel to $\sigma_H$ - N155°E (adapted from Armand et al. 2014)

*Drifts following the direction of $\sigma_h$ :*

It is observed that the extension of fractures, for drifts excavated in this direction, is more developed in the vertical direction of the drift cross section. The fractured zone is composed of mixed fractures (extensional and shear fractures) near drift ceiling and floor, followed by an extension of only shear fractures until about 0.6-0.8 times the diameter (Fig. 1.17b). In the horizontal direction only a distribution of mixed fractures has been observed. Table 1.3 summarizes the average extent (related to the excavation diameter) of fracture zones for both directions of excavation.

**Table 1. 3.** Average extent of fracture distribution around drifts – distance related to the drift diameter (adapted from Armand et al. 2014)

| *Direction parallel to:* | Extensional fractures | | | Shear fractures | | |
|---|---|---|---|---|---|---|
| | Ceiling | Floor | Wall | Ceiling | Floor | Wall |
| $\sigma_H$ | $0.1 \times D$ | | $0.2 \times D$ | - | - | $0.8 \times D$ |
| $\sigma_h$ | $0.3 \times D$ | $0.4 \times D$ | $0.1 \times D$ | $0.6 \times D$ | $0.8 \times D$ | - |

As explained by Blümling et al. (2007), the development of the fracture networks around the excavations is related to the material anisotropy and to the orientations of the principal in-situ stresses. Indeed, it is observed that the shape of the fractured zone differs in the two directions of excavation, which correspond to different initial stress state. For drifts following the direction of $\sigma_H$, the initial stress state is quasi-isotropic in the plane of the drift cross section, but the extent of the fractured zone presents a dissymmetrical shape with a higher extent in the horizontal direction. Therefore, these observations suggest that the intrinsic anisotropy of the material plays an important role in the development of fractures.

### 1.5.2. Convergence measurements

Convergence monitoring have been performed since the construction of drifts or micro-tunnels until now, i.e. for several months or years, depending on the drift. In-situ observations showed an anisotropic response of the drifts convergence, which is more pronounced for drifts excavated along the minor horizontal stress with a ratio of vertical to horizontal convergence of about 4.0, whereas for drifts excavated along the major horizontal stress this ratio is of about 0.5. The origin of this anisotropic response can be related to some factors as the shape of fracture zone induced by the excavation and to the anisotropic behavior of rock formation, as explained by Armand et al. (2013) and Morel et al. (2013). It should be noted that some differences have been observed on the ratio of vertical to horizontal convergence depending on the excavation rate and the support system. A detailed analysis of the convergence evolution is presented in Part II of this dissertation.

### 1.5.3. Radial and axial displacements measurements

From the extensometers measurements, it is observed that drifts oriented along the direction of $\sigma_H$ show a stronger deformation in the direction of $\sigma_h$ which is extended in a distance of around one drift diameter from the wall. This distance coincides approximately with the extent of the lateral fractured zone in this direction. In contrast, for the drifts excavated parallel to $\sigma_h$, a

stronger deformation is observed in the vertical direction, which is also extended in a distance of one drift diameter which is slightly higher than the extent of the vertical fractured zone.

Axial displacement measurements show an influence of the face advance which begins before the front arriving. The recorded data consistently show that the deformation is initiated at about 2 diameters ahead from the face (Armand et al. 2013). As the head of the extensometer is located outside the influence zone of excavation, it can reasonably be considered as fixed. For GCS drift (5 m of diameter), a maximum displacement of 3 mm is measured at 1.45 m from the face (Armand et al. 2011).

### 1.5.4. *Pore pressure and permeability measurements*

With the excavation advance it has been observed that the pore pressure increases before the passage of the face and that the distance of influence of the excavation on the pore pressure is about 20 m, which is twice the distance of influence observed for the axial displacement measurements. It is also observed that, in the two directions of excavation, an overpressure is developed in the horizontal direction of the cross section. Even though the initial stress state for drifts following the direction of the major horizontal principal stress is quasi-isotropic, an anisotropic pore pressure change is measured around these excavations. It should be noted that similar observations have been made for different excavations sizes as drifts (5 m diameter), micro-tunnels (0.7 m diameter) and boreholes (0.15 m diameter), as explained by Armand et al. (2015b). A detailed presentation and analysis of the in-situ pore pressure measurements is presented in detail in Part III of this dissertation.

It has been observed that the rock permeability is highly influenced by the fracture networks developed around drifts. The highest permeability is found in the extensional fractures zone (Armand et al. 2014) with values higher than $10^{-17}\,m^2$. Next to this zone, a slightly disturbed zone is also observed with a permeability ranging between $10^{-17}\,m^2$ and $10^{-19}\,m^2$. As explained by Pardoen (2015), a correlation between hydraulic conductivity measurements and fractures network observations can be evidenced. Therefore, the zones where the permeability is affected depends on the drifts orientations (Fig. 1.19).
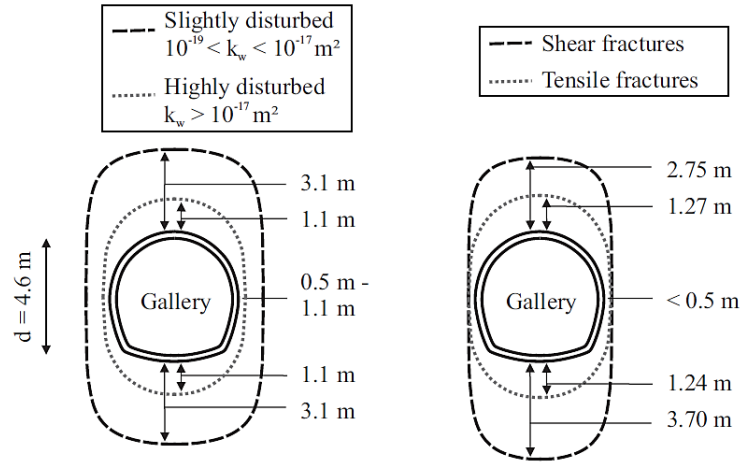
**Fig. 1. 19.** Extensions of hydraulic permeability (left) and fracture zones (right) measured around GED drift (4.6 m diameter) parallel to the minor horizontal principal stress $\sigma_h$ (from Pardoen 2015)

### 1.5.5. Support monitoring

As explained above, in all the drifts, the highest convergence is observed in the direction of the cross section for which the fractured zone is more developed (i.e. in the horizontal direction for drifts following the direction of $\sigma_H$ and in the vertical direction for drifts following the direction of $\sigma_h$). In accordance with these observations, the support deformation is also anisotropic with extension and compression zones depending on the load direction in the cross section. As explained by Armand et al. (2015a), the evolution of measured strain and stress in drifts following the direction of $\sigma_H$ (e.g. GCR and GRD4 drifts) confirms an anisotropic stress field in the structure which has to be considered in the design and optimization of the support for the repository. A detailed description of the measurements recorded in the various supports is presented in Part II.

## 1.6. Analysis of in-situ observations: overview of existing numerical models

As explained above, different experimentations performed at the M/HM URL allow to obtain valuable information with respect to the hydro-mechanical response of the host rock as: the anisotropic extension of the fracture network around drifts, which is induced by the excavation progress; the anisotropic closure of drifts and its evolution in time; the pore pressure evolution and the marked overpressures developed around excavation openings.

Moreover, a large number of experimental tests (as explained in section 1.1) and an extensive research program concerning the numerical simulation of the response of the rock mass formation

to the excavation progress has been performed by various research teams in the last decade. As explained by Armand et al. (2016), the development of these models aims to reproduce the THM behavior of the Callovo-Oxfordian claystone under different repository conditions and for different repository structures. The development of constitutive models for the Callovo-Oxfordian claystone started within the framework of the MODEX-REP European project and of scientific cooperations between Andra and research institutions (Andra 2005, Su (Ed) 2003 and 2007). Then, in 2012 a model benchmark exercise (Seyedi et al. 2016) has been launched in order to provide an overall view of the developed and used models regarding the in-situ observations. This exercise has been based on two series of test cases: (1) at the material point scale and (2) at the drift scale. The main goal was to evaluate the proposed models and analyze how the assumptions made in each model influence the outcomes with respect to the in-situ observations.

Numerical modelling has been performed generally based on isotropic elastic-viscoplastic models (e.g. Plassart et al. 2013; Souley et al. 2011; Blanco Martin et al. 2011a; Renaud et al. 2010). More recently, other models have been used such as: damage models (e.g. Robinet R et al. 2015), discrete elements based analysis (e.g. Yao et al. 2015) and a two-scale computational homogenized model (CHM) (e.g. van den Eijnden 2015). Table 1.4 presents a summary of the models developed and used within the benchmark. An overview of the main characteristics and performances of the existing models is presented in the review paper of Seyedi et al. (2016) and will be summarized in the following.

### 1.6.1. *Isotropic elastic-viscoplastic models*

The short-term response of the rock is described by strain hardening/softening elastoplasticity. Progressive damage is taken into account either through plasticity theory or damage mechanics, as explained by Souley et al. (2011). The modified Lemaître's model is commonly used for the time-dependent response (e.g. Souley et al. 2011). Some authors consider a coupling between plastic strains and viscoplastic damage and assume a time-dependent degradation of both the elastic modulus and the failure surface (e.g. Chiarelli et al. 2003; Shao et al. 2006a; Zhou et al. 2008). Most of these models focus on the mechanical response of the host rock. Some of them also take into account the hydro-mechanical behavior (e.g. Mánica et al. 2015) and thermo-hydro-mechanical behavior (e.g. Jia 2006).

The obtained results show that the elasto-visco-plastic models can provide some overall information about the global behavior of the rock mass around drifts, as the extent of the plastic zone compared to the global extent of the damaged zone and the pore pressure evolution induced by the drifts excavations:

Concerning the extent of the damage zone around drifts, it has been observed that, for any softening constitutive law, using an elastoplastic model to simulate the behavior beyond the strength peak yields to mesh dependent results associated to strain localization, as explained by Seyedi et al. (2016). Therefore, a regularization technique is necessary to obtain robust and mesh-independent results (e.g. Collin and Pardoen 2013). As explained by Pardoen et al. (2015a), the second gradient theory can be used to properly model the development of shear fractures around drifts as strain localization zones. In these works, the main trends of the fractures network as obtained in the numerical analyses (Fig. 1.20) are in good agreement with in-situ observations for the drifts oriented along the minor horizontal stress (Collin and Pardoen 2013; Pardoen et al. 2015a). Moreover, the influence of cross-anisotropy on shear strain localization has been studied in the case of an initial isotropic stress state, for drifts oriented along the major horizontal stress (Pardoen et al. 2015b).
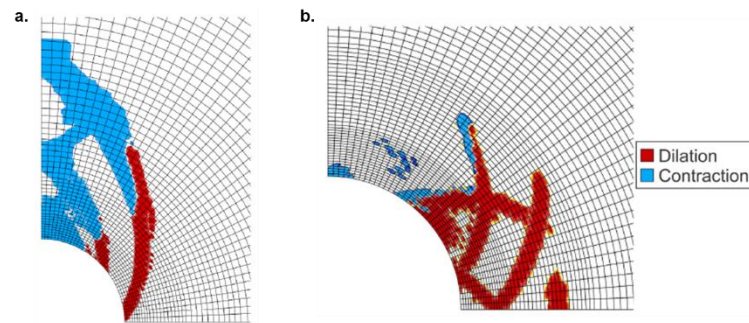


**Fig. 1.20.** Shear band type at the end of drift excavation. Results obtained fort he case of: a. A drift following the direction of $\sigma_h$ . b. A drift following the direction of $\sigma_H$ (adapted from Pardoen 2015)

Concerning the pore pressure evolution, most of the models cannot reproduce the anisotropic evolution of the pore pressure around drifts. This is the case in particular for drifts oriented in the direction of the major principal horizontal stress, for which the pore pressure field around the drifts is anisotropic and marked overpressures are observed in the horizontal direction of the cross section. Important improvements have been recently obtained with the anisotropic time-dependent model proposed by Mánica et al. (2016). This model seems to give accurate results regarding the in-situ observations, mainly for reproducing the increase of the pore pressure before the passage of the drift face (with a lower value of the peak observed in-situ) and the drop of the pore pressure observed in the horizontal direction of the cross section due to the increase of the permeability in the damaged zone (Fig. 1.21). However, further study is required for the reproduction of the peak value of overpressure observed before of the face passage. Moreover, overpressure is observed for several months after the passage of the face, which is not well reproduced by the existing models.

Therefore, an accurately reproduction of the pore pressure evolution in time needs also further study.

In summary, important improvements can be made by accounting for strain localization and considering an initial mechanical anisotropy. However, no information is provided on the detailed behavior of the fractured zone, density of fractures and their possible opening. Moreover, the pore pressure evolution in time and the values of the overpressure peaks need further progress. Finally, it should be noted that the anisotropic closure evolution is one of the points which needs improvement.
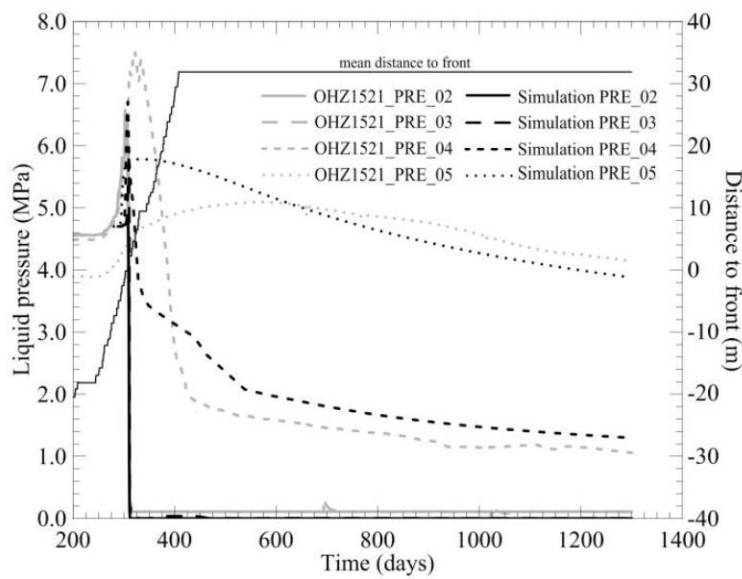


**Fig. 1. 21.** Horizontal pore pressure evolution. In-situ measurements are represented with continuous lines and simulation results with dashed lines (adapted from Mánica et al. 2016)

### 1.6.2. Damage models

Understanding damage mechanisms and the possible pattern and extent of induced fracture zones around the repository structures constitute an important issue in the context of radioactive waste disposals, as explained by Seyedi et al. (2015). However, as explained by Pouya et al. (2016), damage zones around some excavations openings show shapes and extensions which are difficult to reproduce and analyze by classical approaches. Therefore, as a complement of the elastic-viscoplastic approach, phenomenological damage models are recently studied in order to reproduce induced damage around the drifts and the non-symmetric pattern observed.

In recent works, Robinet R et al. (2015) proposed a model that depends on a double strain based criterion in extension/compression. Moreover, an interaction between damage and creep rate is

also introduced providing rather good results with respect to the extension of the fracture zone. However, damage threshold and damage/creep interaction function are calibrated on situ data for the diameter of a given drift. Therefore, extrapolation of the model to structures with different diameters needs further study and improvement.

Continuum damage mechanics based models can be considered as a complementary approach to elasto-visco-plastic models in order to better assess the reproduction of the fractures network developed around drifts. More efforts are underway to develop robust damage models especially regarding damage evolution laws and the treatment of the damage localization phenomena.

### 1.6.3. Discrete elements based method

Discrete elements based methods represent another way for reproducing induced damage around drifts. As explained by Yao et al. (2015), the elasto-visco-plastic models fail to explicitly describe the onset of macroscopic fractures. Moreover these authors argued that, even if extended finite element methods have also been proposed to consider the onset and propagation of fractures, these models are generally limited to 2D conditions and fail to deal with multiple fractures problems.

An extended rigid block spring method is proposed, which is developed to provide an alternative discrete approach for modeling crack growth and fracturing in cohesive brittle materials (Yao et al. 2015). In this model, the rock mass is characterized by an assembly of rigid blocks linked together with interface laws representing the macroscopic mechanical behavior of the rock. Moreover, the local failure process of an interface is controlled by both normal and shear stresses with possible tensile and shear failures. One key point of this method is the mesh generation, which is developed in order to minimize effects of mesh size and arrangement. Indeed, the numerical results show that for example the peak compression strength is nearly independent on the element size and mesh arrangement (Yao et al. 2015 and Yao et al. 2016a).

As explained by Yao et al. (2015), the proposed model is able to describe the main features of mechanical behavior of brittle rocks, in particular the transition from diffused microcracks to localized fractures. The modeling results obtained for the Callovo-Oxfordian claystone (Yao et al. 2016b), show that taking into account the mechanical anisotropy improves significantly the obtained fracture patterns in both directions of excavation (Fig. 1.22). However, additional efforts are necessary to improve their efficiency and for taking into account hydromechanical coupling, time-dependent behavior and hydromechanical anisotropy.
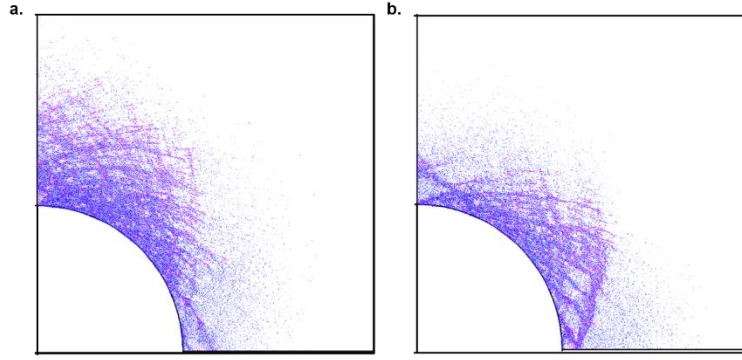
**Fig. 1. 22.** Fracture patterns for a. A drift following the direction of $\sigma_h$. b. A drift following the direction of $\sigma_H$. Tensile cracks are represented by blue color and shear cracks by pink color (adapted from Yao et al. 2016b)

### 1.6.4. A two-scale computational homogenized model

A two-scale computational homogenized model (CHM) has been developed to model the localization of deformation around drifts excavation taking into account the hydro-mechanical coupling (van den Eijnden 2015). The rock is modeled by representative elementary volumes (REV) at the micro scale and the global response of this REV serves as a homogenized numerical constitutive law for the macro-scale. Then, as explained by van den Eijnden et al. (2016a), on the macroscale a poro-mechanical continuum is defined with coupled hydro-mechanical behavior, relying on the constitutive relations obtained from the modelling at the microscale. Moreover, this approach is coupled with a local second gradient paradigm to be able to study localization of strain and to maintain mesh objectivity when shear bands develop. The results (Fig. 1.23) are a good prospective on obtaining a general way of modelling material anisotropy and hydromechanical coupling (van den Eijnden et al. 2016a). However, it seems that more efforts are still necessary for a more realistic microstructural representation and to improve the efficiency of the model to be used at large-scale.
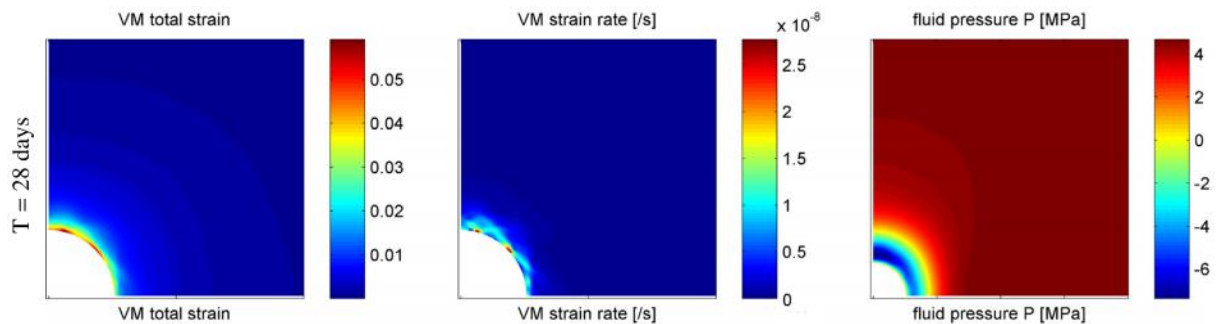


**Fig. 1. 23**. Deformations and pore pressure fields around a drift following the direction of $\sigma_h$. Simulation performed at 28 days (adapted from van den Eijnden et al. 2016b)

## *1.6.5. Discussion*

The development of different numerical models has allowed an important progress in the simulation of the in-situ observations at the M/HM URL. Therefore, these advances allow to have a global vision of the possible avenues to explore in the design of the deep geological repository. However, as explained by Seyedi et al. (2016), more efforts are necessary to improve the robustness of these approaches in the complex context of Callovo-Oxfordian claystone response to excavation works, where a detailed reproduction of the whole in-situ observed phenomena by a numerical model remains a challenge. Further study and improvements are required mainly in:

- The fracture network reproduction: Even if some models based on fractures mechanics for modelling crack initiation and propagation (e.g. Hauseux et al. 2016 for crack initiation) or on strain localization analysis accounting for the non-linear behavior of porous material (e.g. Pardoen et al. 2015a and 2015b) give interesting insights, further study is required mainly for the reproduction of extensional fractures. Therefore, a model which is able to give information about the density of fractures is still an open question.
- Convergence evolution: The anisotropic closure of drifts cannot be correctly reproduced in most of the models, mainly for drifts oriented in the direction of the major principal horizontal stress. For this direction the initial stress state in the section of drift is quasi-isotropic, but the closure of the drift cross section showed an anisotropic pattern of deformation. An accurate reproduction of this anisotropic closure and its evolution in time remains a task to achieve.
- Pore pressure evolution around drifts: Most of the models cannot reproduce the anisotropic evolution of the pore pressure around drifts, mainly for drifts oriented in the direction of the major principal horizontal stress. In these drifts, even with a quasi-isotropic initial stress state, the pore pressure field around drift shows an anisotropic response with marked overpressures developed in the horizontal direction of the cross section. Further study is required for the reproduction of the peak value of overpressure observed before of the face passage and for an accurately reproduction of the pore pressure evolution in time.

Within this context, the present work addresses the question of the anisotropic closure evolution of drifts by means of a direct analysis of in-situ measurements performed at the M/HM URL. This will be presented in the next part of this dissertation.

**Table 1. 4.** Summary of the different models used in the framework of a benchmark exercise for the Callovo-Oxfordian Claystone (adapted from Seyedi et al. 2016)

| Model | Complementary description | Mechanical anisotropy | Failure criterion | Time-dependent behavior | References |
|---|---|---|---|---|---|
| *Elasto-visco-plasticity* | | | Generalized Hoek et Brown criterion with hardening and softening functions | Perzyna type model, taking into account tertiary creep | Laigle 2004; Kleine 2007; Plassart 2011; Plassart et al. 2013 |
| | | | | Lemaitre type model, with creep threshold and damage-dependent creep strain rates | Souley et al. 2009; Souley et al. 2011 |
| | | | Drucker-Prager including the effect of $\sigma_{moy}$ | Lemaitre type model, with creep threshold | Hoxha et al. 2007a and 2007b |
| | | Anisotropic elasticity | Power type failure function with hardening/softening | The creep is governed by a kinematic hardening law accounting for in-situ stress state | Hoxha et al. 2007a and 2007b |
| | | Yes | Mohr-Coulomb criterion for the yield and failure limits and its anisotropic extension | Modified form of the Lemaitre law for visco-plastic strains | Mánica et al. 2015; Mánica et al. 2016 |
| | with localisation traitment | | Drucker-Prager with hardening law on friction angle/cohesion | | Collin and Pardoen 2013; Pardoen et al. 2015a |
| | | Yes | Drucker-Prager with hardening law on friction angle/cohesion, with anisotropic cohesion | | Pardoen et al. 2015b; Pardoen 2015, Pardoen and Collin 2016 |
| *Elastoplasticity* | with isotropic damage | | Strain based criterion with distinction between compression and extension damage | Creep strain modeled as a retarded elastoplastic strain | Chiarelli et al. 2003; Shao et al. 2006a ; Jia 2006 ; Zhou et al. 2008 ; Jia et al. 2008 |
| | with anisotropic damage | Yes | Strain based criterion with distinction between compression and extension damage and anisotropy accounted through a fabric tensor | | Shao et al. 2005; Shao et al. 2006b ; Chen et al. 2010 |
| *Rigid Body-Spring Model(RBSM)* | | Yes | Isotropic/anisotropic criterion for interface failure | | Yao et al. 2015, 2016a and 2016b |
| *Anisotropic damage model* | | Yes | Double strain based criterion in extension/compression | Time-dependent strains calculated through a creep law calibrated based on creep tests | Robinet et al. 2015 |
| *Computational homogenized model (CHM)* | | Yes | FEM2[*] using a REV[**] (at the micro scale). The global response of this REV serves as a homogenized numerical constitutive law for the macro-scale | | van den Eijnden 2015, van den Eijnden et al. 2016a and 2016b. |

[*] FEM2 – Double scale finite element method          [**] REV – Representative elementary volume

## 1.7. Conclusions

The hydro-mechanical behavior of the Callovo-Oxfordian claystone and its response to the excavation works have been followed and studied during several years at the Meuse/Haute-Marne Underground Research Laboratory (M/HM URL). To this aim, different experimental drifts have been excavated following the direction of the major and minor horizontal principal stresses. The excavation has been performed with different characteristics (e.g. excavation methods, support systems, excavation size). A continuous monitoring around drifts has been performed from the excavation time until now. Several sections have been equipped with high precision measurement sensors, in order to follow the hydro-mechanical response induced by the excavation and its evolution in time. Valuable information has been obtained with respect to the host rock response such as: the anisotropic extension of the fracture network around drifts, which is induced by the excavation progress; the anisotropic closure of drifts and its evolution in time; the pore pressure evolution and the marked overpressures developed around excavation openings. These observations suggest that, in addition to the effect of the initial stress state, the rock anisotropy plays a key role in the response of the rock mass formation.

In complement to the different experimentations performed at the M/HM URL, a large experimental program of laboratory tests has been performed on samples extracted from the URL by various research teams to get a good knowledge of the hydro-mechanical behavior of the Callovo-Oxfordian claystone. Moreover, an extensive research program dedicated to the numerical simulation of the rock response to the excavation progress has been developed in the recent years. These models are mainly based on the analysis of the hydro-mechanical response of the host rock. Important advances have been achieved for the simulation of the in-situ observations. However, a good reproduction of all the phenomena observed in-situ by a numerical model needs still improvement, mainly related to the anisotropic hydro-mechanical response of the ground. One of the key tasks to achieve is to reproduce, as accurately as possible, the anisotropic closure of drifts. This is very important for design of the support systems.

# PART II: LONG-TERM ANISOTROPIC CLOSURE IN DRIFTS

The main goal of this part is to study the anisotropic closure of drifts during and after the excavation progress. This is done by means of a direct analysis of the convergence measurements. The monitoring and analysis of convergence data can provide a reliable approach of the interaction between rock mass formation and support, which is a key issue for the supports design. For the sake of simplicity, first a detailed description of the experimental drifts studied in this work will be presented (section 2.1). The semi-empirical law used for the analysis of convergences is then described in section 2.2. In sections 2.3 to 2.7, a detailed description of the convergence measurements performed in each drift will be presented together with the proposed analysis.

Following the methodology proposed by Vu et al. (2013), the principal axes of deformation are identified assuming that the drift sections deform following an elliptical shape, according to the anisotropic character of the drifts closure observed in-situ. Then, the convergence evolution is analyzed based on the semi-empirical law proposed by Sulem et al. (1987). This convergence law permits to clearly distinguish the face advance effect from the time-dependent response of the ground. It also permits reliable prediction of long-term closure as shown for various tunnels excavated in squeezing ground (e.g. Sulem et al. 1987; Panet 1996; Vu et al. 2013). One first objective of this part is to evaluate the parameters of this convergence law along the two principal axes of deformation for two drifts excavated in perpendicular directions. As shown in the following, a remarkable result is that several parameters of the convergence law are the same in the two principal directions of deformation, and do not vary along each drift. The anisotropy and the variability of the closure are thus mainly described by the variation of a single parameter identified as the short-term closure. It is shown that fitting this parameter on the first measurements of a different drift (not used in the calibration of the other parameters) is sufficient for a reliable prediction of the long-term closure.

In the next part, the effect of the excavation size on the long-term anisotropic convergence evolution is analyzed. To this aim, a direct analysis of the convergence measurements in drifts of different sizes (0.74 m, 3.8 m, 5.2 m and 6.3 m of diameter) is performed. This comparison is made on drifts excavated in the direction of the major horizontal principal stress ($\sigma_H$). Furthermore, the effect of the support system and the time delay for the support installation is also discussed. Finally, the influence of the enlargement of the drift cross section on the long-term response is analyzed.

## 2.1. Overview of studied drifts

Each drift excavation is an experiment in itself and is used to characterize the response of the rock to different drift excavation and construction methods. This work includes the analysis of five different experimental drifts (with diameters ranging between 3.8 and 6.3 m) and one micro-tunnel (0.74 m diameter). Note that in addition to the different size of excavations openings, the studied drifts are characterized by different methods of excavation and support, different geometry and orientation. A detailed description of all drifts is presented in this section. Tables 2.1, 2.2 and 2.3 summarize the characteristics, the geotechnical and support instrumentation of all the studied drifts.

### 2.1.1. GCS drift

The GCS drift follows the direction of $\sigma_H$. Excavated by a road header machine, it has a circular section with a diameter of 5.2 m and a length of 63.3 m. Its support is installed immediately after each step of excavation, which has a length of 1.2 m. The support is composed of radial bolts, 21 cm thick layer of fiber shotcrete, yieldable concrete wedges and welded mesh (Fig. 2.1). The yieldable concrete wedges take in charge the rock mass deformation and allow for the ground deconfinement. A detailed description of this support is presented in Bonnet-Eymard et al. (2011).
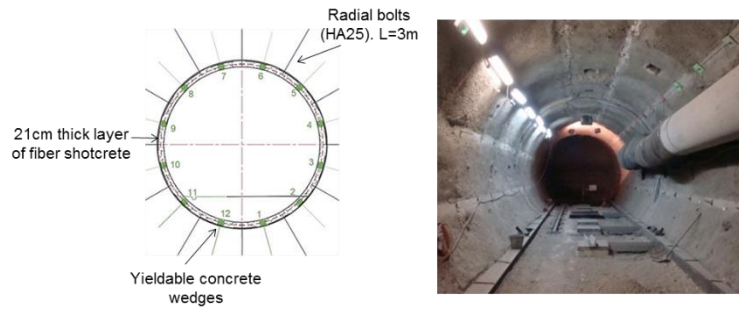


**Fig. 2. 1.** GCS support section: distribution of bolts and compressible wedges around the drift perimeter

Convergence data have been recorded in six sections along the drift, as explained in section 1.4.1 (Part I). Convergence monitoring has been performed since the construction of the drift until now, i.e. for about six years. During the first two weeks after the excavation, the measurements were taken with a frequency of one per day. After that, the frequency of measurements decreases. In the last year, one measurement was taken every four months.

In addition to the convergence measurements, one extensometer monitoring section has been installed at PM 40 (metric point from the entrance of the drift), as shown in section 1.4.2 (Part I). Finally, one horizontal extensometer was installed in a parallel drift and it arrives perpendicularly to the right wall of GCS drift at PM 17.3. This extensometer was installed before the excavation of GCS and its position permits to follow the deformation induced by GCS excavation. In Section 2.3.3, the data obtained by this extensometer will be analyzed and compared with the data obtained from the convergence measurements in the section at PM 16.9.

### 2.1.2. GCR drift

The GCR drift is excavated by a road header machine parallel to GCS drift (i.e. follows the direction of $\sigma_H$). It has a circular section with a diameter of 5.4 m and a length of 64.3 m. The GCR drift has the same kind of support as GCS. However, between PM 47.5 and 58.3, the support does not include yieldable concrete wedges (Fig. 2.2). Convergence has been monitored in three sections. One monitoring section has been installed in the last part of the drift (with the stiffer support), which permits to follow the influence of a different support in the convergence evolution.

It should be noted that for this drift, a permanent stiff lining (27 cm thick concrete annulus) has been installed about 7 months after the installation of the first support presented above. However, this study focusses only on the response during the first seven months that will be compared with that of GCS drift.



**Fig. 2. 2.** GCR section. Flexible support (left) and final lining installed after 7 months (rigth)

### 2.1.3. GED drift

This drift follows the direction of $\sigma_h$. Excavated by a pneumatic hammer machine, it has a horse-shoe section with an average diameter of 4.6 m and a length of 71.2 m. Its support is also installed

immediately after each step of excavation which has a length of 1 m. The support is composed of radial bolts, sliding arches installed every meter and a 10 cm thick layer of fiber shotcrete, as shown in Fig. 2.3.

Six convergence measurement sections have been installed along the drift. However, only three sections are considered as representative for the convergence measurements analysis. Actually, the three last sections were installed as a part of the drift dedicated to the analysis of the influence of the saturation and desaturation process on the excavation damaged zone (EDZ). These sections were isolated and the measurements were stopped. For the three first sections, the frequency of measurements is the same as described above for GCS drift and convergence has been monitored for about eight years.

As for GCS, during the excavation progress, one extensometer measurement section was installed at PM 50.4. Because of the drift position, the installation of an extensometer section before the beginning of the excavation was not possible.



**Fig. 2. 3.** GED support section

### 2.1.4.  GRD4 drift

The GRD4 drift is excavated in the direction of $\sigma_H$ by a road header under shield technique. It has a circular section with a diameter of 6.3 m and a length of 89 m. Its rigid support is composed of segmental lining, with segments of 45 cm thick and 0.8 m length. An initial 15 cm over-cut is taken into account. The remaining gap is filled with radial injection of mortar. At the end, the inner and outer drift diameters are 6 m and 5.10 m respectively. The support is installed a couple of days after the passage of the tunnel face. About 20 days after the passage of the face, the entire support is completed and functional. The cross section after excavation and the distribution of support installation are presented in Fig. 2.4.

Because of the method of excavation, the convergence measurement sections and the reinforced measurements sections were installed after the support installation. Consequently, an important part of the convergence and radial displacements is lost in the records. However, a horizontal extensometer was installed as a part of a mine-by experiment in a neighbor drift, before the beginning of excavation. This extensometer is perpendicular to the left wall of GRD4 drift. Thus, in the following, the analysis of the closure evolution of this drift is based on the analysis of the radial displacements recorded by this extensometer.
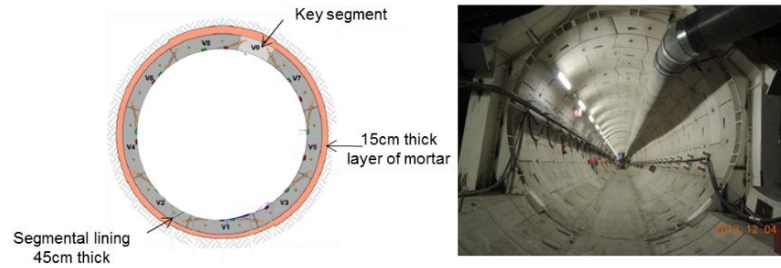


**Fig. 2. 4.** GRD4 support section

### 2.1.5.  GRM3 drift

The GRM3 drift is excavated in the framework of a DPC experiment ('Déconfinement Préliminaire avant Creusement' i.e. preliminary deconfinement before tunnel excavation to the final diameter) performed in the URL. This experiment consists of a drift excavation in two stages. In the first stage, the drift is excavated with a lower diameter than the final one. Then, about three months after the end of the first stage, an enlargement of the cross section is performed to obtain the final diameter. The main goal was to investigate if it is possible to reduce the extent of the excavation induced fractured zone by this two stages of excavation as compared to a drift excavated directly to the final diameter (Noiret et al. 2015).

This drift follows the direction of the major principal horizontal stress $\sigma_H$. Excavated by a pneumatic hammering machine, it has a circular section with a diameter of 3.8 m and a length of 46.2 m (stage 1). Its support is installed immediately after each step of excavation which has a length of 1.5 m. The support is composed of radial bolts and 10 cm thick layer of fiber shotcrete, except in the lower part of the section which is left unsupported. The cross section after excavation are presented respectively in Fig. 2.5a.

The second stage of excavation (stage 2), consists in an enlargement of the drift cross section, as explained above. The final diameter of the drift is 5.7 m in the first 16 m of excavation, then 5.2 m in the remaining part. Its support is installed immediately after each step of excavation

which has a length of 1 m. The support is composed of radial bolts, 5 cm thick layer of fiber shotcrete (20 cm in the lower part of the drift section) and sliding arches installed every meter (Fig. 2.5b). A photo of the cross section presenting the first stage and the over excavation is shown in Fig. 2.5c.
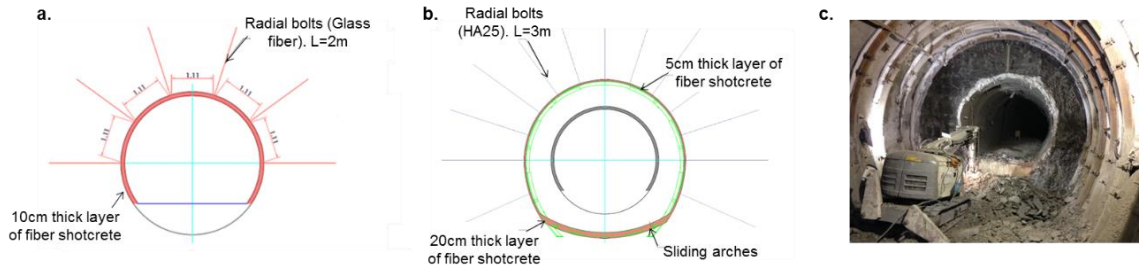


**Fig. 2. 5.** GRM3 support section: a. Stage 1. b. Stage 2. c. Cross section showing the first stage and the enlargement of the cross section

For a continuous monitoring of the walls closure evolution, four convergence measurement sections (SMC) have been installed along the drift. In order to follow the convergence evolution with the advance of the enlargement stage, four convergence measurement sections (SMCs) have been installed very close to the ones installed in the stage 1, as showed in Table 2.3. Moreover, deformations due to the enlargement of drift section have been followed by a reinforced measurement section (SMR) installed in stage 1 of the excavation at PM 12.1.

### 2.1.6. ALC1603 micro-tunnel

This micro-tunnel follows the direction of the major principal horizontal stress $\sigma_H$. Excavated by a micro tunnel boring machine, it has a diameter of 0.74 m and a length of 20 m. This micro-tunnel is unsupported, which permits to study the response of the ground alone (Fig. 2.6). The excavation rate was around 0.6-0.7 m/hour and the excavation has been performed in 3 days. It should be noted that, due to a hydraulic failure, the excavation had been stopped for 31 hours at PM 13. The convergence measurements instrumentation was installed 3 weeks after the end of the excavation. Four measurement sections have been installed at PM 4, PM 8, PM 12 and PM 16 respectively. Measurements are taken in the vertical, horizontal and transverse directions as shown in Fig. 1.10 (Part I). It should be noted that, for the micro-tunnel, as the convergence measurements instrumentation was installed 3 weeks after the end of the excavation, the recorded data only describe the time-dependent behavior of rock mass. The face of the micro-tunnel is far enough from the convergence measurement sections, thus it doesn't have any influence on the convergence evolution.
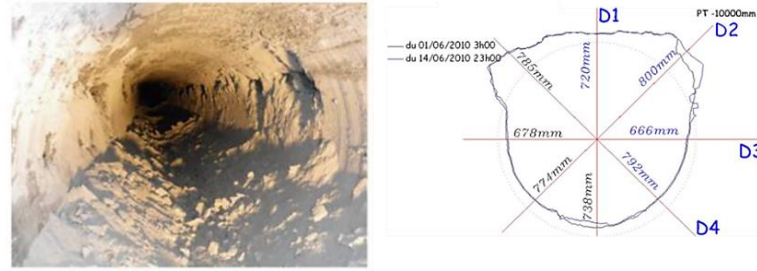
**Fig. 2. 6.** State of the ALC1603 micro-tunnel wall (adapted from Morel et al. 2013). At left: Photo after the end of excavation. At right: typical profile of the micro-tunnel wall after excavation

**Table 2. 1**. Characteristics of studied drifts in the M/HM URL

| Drift | | Direction | Dimensions | | Excavation description | | Type of support |
|---|---|---|---|---|---|---|---|
| | | | Diameter (m) | Length (m) | Machine | Step of excavation (m) | |
| GCS | | Parallel to $\sigma_H$ | 5.2 | 63.3 | Road header | 1.2 | Flexible |
| GCR | | | 5.4 | 64.3 | Road header | 1.2 | Flexible/Rigid |
| GRD4 | | | 6.3 | 89 | Road header under shield | 89[*] | Rigid |
| GRM3 | Stage 1 | | 3.8 | 46.2 | Pneumatic hammering | 1.5 | Flexible |
| | Stage 2 | | 5.2 – 5.7 | 46.2 | | 1.0 | Flexible |
| ALC1603 micro-tunnel | | | 0.74 | 20 | Micro-tunnel boring | 20[*] | |
| GED | | Parallel to $\sigma_h$ | 4.6 | 71.2 | Pneumatic hammering | 1.0 | Flexible |

[*] The excavation progress is considered as continuous

**Table 2. 2.** Description of support installed in each drift and its monitoring sections

| Drift | | Support description | | | Support monitoring sections |
|---|---|---|---|---|---|
| | | *Radial bolts* | *Thick layer of fiber shotcrete (cm)* | *Complement* | |
| GCS | | yes | 21 | yieldable concrete wedges and welded mesh | 2 monitoring sections for yieldable concrete wedges at PM:[**] 29.5 – 47.5 2 monitoring sections for shotcrete at PM: 34.0 (hoop strain); and 37.0 (hoop stress) |
| GCR | | yes | 21 | yieldable concrete wedges and welded mesh | 2 monitoring sections for yieldable concrete wedges at PM: 22.3 – 43.7 5 monitoring sections for shotcrete at PM: 36.0 – 40.9 – 55.3 (hoop strain); and 37.3 – 54.1 (hoop stress) |
| GRD4 | | | | segmental lining with radial injection of mortar | 4 monitoring sections for segmental lining at PM: 21.2 – 37.2 (zone with classical mortar); and 53.2 – 69.2 (zone with compressible mortar) |
| GRM3 | Stage 1 | yes | 10 | | |
| | Stage 2 | yes | 5 (20 cm in the lower part of the drift section) | sliding arches installed every meter | |
| ALC1603 micro-tunnel | | | | | |
| GED | | yes | 10 | sliding arches installed every meter | |

[**] PM – metric point from the entrance of the drift

**Table 2. 3.** Geotechnical instrumentation of studied drifts in the M/HM URL

| Drift | PM (m) | Description | Convergence measurements | Extensometers measurements | Reverse head extensometers | Pore pressure borehole |
|---|---|---|---|---|---|---|
| GCS | 0.0 – 13.3 | Dedicated to the installation of the road header machine | 1 monitoring section at PM: 8.5 | | | |
| | 13.3 – 57.7 | Part of the studied drift | 6 monitoring sections at PM: 16.9 – 30.1 – 40.7 – 49.2 – 52.9 – 57.7 | 1 reinforced measurement section at PM 40 2 extensometers of mine-by test at PM 17.3 (perpendicular to GCS axis) and at PM 37 | 1 reverse head extensometer at PM 30.6 to 49.6 | 6 boreholes of mine-by test: 4 from GAT drift (one arrives to the axe of the GCS drift at PM 35.7); and 2 from GLS drift |
| | 57.7 – 63.3 | Support of only radial bolts | 1 monitoring section at PM: 58.6 | | | |
| GCR | 0.0 – 16.3 | Dedicated to the installation of the road header machine | 1 monitoring section at PM: 10.6 | | | |
| | 16.3 – 47.5 | Part of the studied drift (flexible support as GCS) | 2 monitoring sections at PM: 22.1 – 43.6 | 1 reinforced measurement section at PM 23.5 | 1 reverse head extensometer at PM 34.2 to 53.2 | |
| | 47.5 – 58.3 | Part of the studied drift (stiffer support) | 1 monitoring section at PM: 53.2 | 1 reinforced measurement section at PM 52.3 | | |
| | 58.3 – 64.3 | Non-instrumented (flexible support) | | | | |
| GRD4 | 0.0 – 4.0 | Dedicated to the initial operation of the road header under shield machine | | | | |
| | 4.0 – 43.2 | Part of the studied drift, support with a classic mortar | 4 monitoring sections at PM: 10.8 – 20.4 – 26.8 – 36.4 | 1 reinforced measurement section at PM 27.6 1 extensometer of mine-by test at PM 15.7 | 1 reverse head extensometer at PM 20.8 to 39.8 | 2 boreholes of mine-by test from GET at PM 25.2 (horizontal and inclined ascending) |
| | 43.2 – 48.0 | Transition zone | | | | |
| | 48.0 – 78.4 | Zone of a support with compressible mortar | 3 monitoring sections at PM: 52.4 – 63.6 – 68.4 | 1 reinforced measurement section at PM 62.8 | | |
| | 78.4 – 89.0 | Dedicated to the uninstallation of the road header under shield machine | | | | |

| | | | | | |
|---|---|---|---|---|---|
| GRM3 | 0.0 – 46.2 | Stage 1 | 4 monitoring sections at PM: 12.9 – 25.7 – 36.2 – 43.7 | 1 reinforced measurement section at PM 12.1 | |
| | 0.0 – 46.2 | Stage 2 | 4 monitoring sections at PM: 12.8 – 25.9 – 36.2 – 43.2 | | |
| ALC1603 micro-tunnel | 0.0 – 20.0 | | 4 monitoring sections at PM: 4.0 – 8.0 – 12.0 – 16.0 | | |
| GED | 0.0 – 57.0 | Part of the studied drift | 3 monitoring sections at PM: 19.5 – 35.5 – 51.5 | 1 reinforced measurement section at PM 50.4 | 4 boreholes installed at about 7 months after the end of excavation. PM 52.5 |
| | 57.0 – 71.2 | Dedicated to analyze the influence of saturation and desaturation process | 3 monitoring sections at PM: 59.1 – 61.6 – 63.9 | | 4 boreholes installed at about 7 months after the end of excavation. PM 61.0 |

## 2.2. Convergence law

The convergence is the variation of distance between two opposite points of the drift wall. It is a function of variables: $x$ - distance to the face and $t$ - time after passage of the face. Thus, for the case of a circular tunnel, the convergence evolution can be defined as $C(x,t) = D - D_0$, with $D_0$ the initial diameter and $D$ the final diameter of the tunnel section (for a given distance $x$ and time $t$, after the passage of the tunnel face).

Furthermore, the total deformation is defined as the addition of the instantaneous and time-dependent deformation $\varepsilon = \varepsilon_i + \varepsilon_d$. In an attempt to analyze the influence of the convergence evolution as a function of these two variables, Panet (1979) proposed a relation (eq. 2.1) decoupling the convergence induced by the tunnel face advance ($C_1(x)$) and the time-dependent convergence, which depends on the rheological behavior of the rock mass ($C_2(t)$):

$$C(x,t) = C_1(x) + C_2(t) \tag{2.1}$$

### 2.2.1. Tunnel face advance effect

The excavation advance changes the initial equilibrium of the medium inducing deformations close to the face after its passage. Therefore, the dominant parameter is the distance to the face. For the case of an elastic medium, for the analysis of the convergence Panet (1979) proposed a function of exponential evolution (eq. 2.2):

$$C_1(x) = C_{\infty x}\left[1 - e^{-\frac{x}{X}}\right] \tag{2.2}$$

Panet and Guenot (1983) proposed a different function to represent the face advance effect for an elastoplastic medium (eq. 2.3):

$$C_1(x) = C_{\infty x}\left[1 - \left(\frac{X}{x+X}\right)^2\right] \tag{2.3}$$

### 2.2.2. *Time-dependent behavior*

When the face is far ahead or during an interruption of the excavation advance, the face influence is attenuated and the deformations are mainly controlled by the rheological behavior of the rock mass formation. To represent the convergence evolution as a function of time, usually logarithmic or exponential functions (eq. 2.4) are implemented. The last one is obtained in the case of a Kelvin-Voigt viscoelastic medium:

$$C_2(t) = A \log(1 + t/T)$$
$$C_2(t) = A(1 - e^{(-t/T)})$$

$(2.4)$

Based on the analysis of the convergence data of Frejus Tunnel (between France and Italy), Sulem (1983) and Sulem et al. (1987) showed that neither an exponential nor a logarithmic function could fit correctly the experimental data. They proposed the following function (eq. 2.5):

$$C_2(t) = A\left\{ 1 - \left[ \frac{T}{t+T} \right]^n \right\}$$

$(2.5)$

Moreover, based on the study of subsequent interruptions of the face advance they concluded that the parameter A was also dependent on the distance to the face $x$ and with a same form as $C_1(x)$ which led to the definition of a new parameter $m = A(x)/C_1(x)$.

### 2.2.3. *General form of the convergence semi-empirical law*

The convergence law proposed by Sulem (1983) and Sulem et al. (1987) depends on five parameters (eq. 2.6): $T$ - parameter related to the time-dependent properties of the system (rock mass formation – support); $X$ - parameter related to the distance of influence of the face, and the extension of the decompressed zone around the drift; $C_{\infty x}$ - instantaneous convergence obtained in the case of an infinite rate of face advance (no time-dependent effect); $m$ - parameter related to the relationship between the time-dependent convergence and the instantaneous convergence; $n$ - exponent which describes the form of the fitted curve. This last parameter has been usually fixed by several authors as 0.3 (e.g. Hingant and Guerpillon 1986, Sulem et al. 1987, Panet 1995, Boidy 2002). However, as will be explained in the following, these convergence law parameters also depend on the excavation process, in particular on the rate of excavation.

$$C(x,t) = C_{\infty x}\left[1-\left(\frac{X}{x+X}\right)^2\right]\left\{1+m\left[1-\left(\frac{T}{t+T}\right)^n\right]\right\}$$ (2.6)

The total convergence in the long-term is defined by:

$$C_{Total} = C_{\infty x}(1+m)$$ (2.7)

This law permits reliable prediction of long-term closure as shown for various tunnels excavated in squeezing ground (Sulem et al. 1987; Panet 1996; Vu et al. 2013). It should be noted that this law has been proposed to describe the tunnel closure evolution by a direct analysis of convergences measurements. In a recent paper of Tran-Manh et al. (2016), the parameters of this law have been related to the ground parameters for the case of the Saint-Martin-la-Porte access adit in France within the framework of a constitutive model with time-dependent degradation of the rock mass.

## 2.3. Analysis of the convergence evolution for a representative supported drift in each direction of excavation

In this section, the convergence measurements recorded for one representative drift in each direction will be presented and analyzed (GCS drift and GED drift, which follow the direction of $\sigma_H$ and $\sigma_h$ respectively). First, the principal axes of deformation are identified for each drift. The evolution in time of these axes is then interpreted as the convergence of the drift wall. This convergence is analyzed based on the semi-empirical law proposed by Sulem et al. (1987). It is observed that this approach allows a satisfactory representation of the anisotropic closure of drifts. The validation of the used methodology will be presented by the analysis of a different drift (GCR drift).

### 2.3.1. In-situ observations

The convergence measurements show an anisotropic closure, which depends on the drifts' orientations. The drifts following the direction of $\sigma_h$ show a vertical to horizontal convergence ratio of about 4.0, while this ratio is about 0.5 for the drifts with axis following the direction of $\sigma_H$ (Armand et al. 2013). It should be noted that for the drifts following this latter direction, the stress state is quasi isotropic in the plane of drift section. The anisotropic behavior of the rock mass may be one of the factors at the origin of the anisotropic deformation and also the fracture distribution around drifts has an influence in the cross section closure of the drift.

For the drifts parallel to $\sigma_H$ (e.g. GCS), the initial in-situ stress state is quasi-isotropic. However, the horizontal convergence is about two times larger than the vertical one, as shown in Fig. 2.7a. A high convergence rate is observed during the first hundred days before reaching stabilization. After 900 days of monitoring, the deformation rate is about $5 \times 10^{-11}$ s$^{-1}$. It should be noted that the convergence rate in the horizontal direction presents values slightly higher than in the vertical direction.

For drifts parallel to $\sigma_h$ (e.g. GED), the initial in-situ stress state is anisotropic. The major principal stress to the vertical principal stress ratio is about 1.3. In this case, the vertical convergence is about four times larger than the horizontal convergence. As in the perpendicular drifts, a high convergence rate is observed during the first hundred days. After that, the horizontal convergence reaches stabilization. But even if the convergence rate decreases with time, the vertical convergence continues to evolve as shown in Fig. 2.7b. After 900 days of monitoring, the deformation rate is about $1 \times 10^{-11}$ s$^{-1}$ in the horizontal direction and $1 \times 10^{-10}$ s$^{-1}$ in the vertical direction.
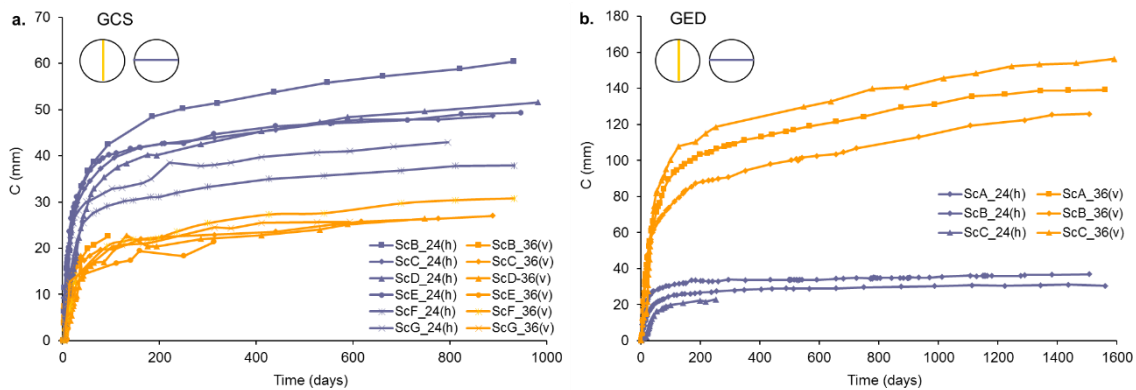


**Fig. 2. 7.** Convergence evolution in drifts of the URL: a. GCS drift excavated along $\sigma_H$ ; b. GED drift excavated along $\sigma_h$

The recorded data clearly show the importance of the rock mass time-dependent behavior in the drifts deformation. This will be discussed in detail in section 2.3.3. Moreover, a significant scatter in the data can be observed in all drifts, and this scatter is more important in the direction of stronger convergence. This is due, on one hand, to local heterogeneities of the rock formation and mainly to the scatter of the fractures' distribution around the drift. On the other hand, the convergence measurement sections were not all installed at the same distance from the face. As mentioned above for the SMR installation, various factors can influence the distance or the time of installation of the convergence targets as for example the works to secure the tunnel face. As the maximum closure rate occurs in the first days after excavation, if the initial measurement is

delayed for a section, a significant part of the total expected closure is lost in the records. However, as explained in the following, this 'lost' part of the convergence curve is actually considered in the analysis of the data.

### 2.3.2. *Analysis of the convergence evolution in a drift following the direction of* $\sigma_H$

The anisotropic character of the drift closure is taken into account by assuming that its shape evolves as an ellipse (Fig. 2.9) (Vu et al. 2013). As explained by Delaloye et al. (2015), elliptical uniform deformation can be expected in a rock mass when either the stress conditions are non-homogeneous or the rock mass is anisotropic. In this section, the methodology used for the data analysis is described. From the convergence data in different directions, the deformation of the drift is first fitted with the equation of an ellipse. The convergence evolution along the two axes of the ellipse is then fitted using the semi-empirical law proposed by Sulem et al. (1987). For the sake of simplicity, data analysis of GCS drift will be used for the explanation of followed procedure. Then, in section 2.3.3 the results of GED drift will be presented and compared with those of GCS.

#### 2.3.2.1. *Evaluation of the elliptical deformation*

Following the methodology proposed by Vu et al. (2013), the convergence measurement data on six different points around the drift are analyzed in order to identify the axes of the ellipse. The evolution in time of the axes' length directly gives the principal directions of deformation, the maximum and minimal wall closure and their evolution with time. Assuming that the walls' closure occurs in the vertical plane, the convergence data are used to evaluate the ellipse parameters.

In the drift network, the local coordinates have been defined with $x_1$-axis in the direction of the major horizontal principal stress N155°E (Fig. 2.8). The initial position of each monitoring point is defined by three local coordinates ($x_1, x_2, x_3$). Then, the evolution of the position of the points is related to the measurements of the five strings that connect them.

As proposed by Vu (2010), it is assumed that the movement of point 3 (located at the roof of the drift, as shown in Fig. 1.9 Part I) is oriented towards the center of the ellipse, not necessarily in a vertical way. A single reference coordinate system is then fixed, where point 3 has its initial coordinate at (0,0). With the information of the strings' initial lengths and the convergence measurements at each date, the position of each point can be described by its coordinates ($X_i, Y_i$).
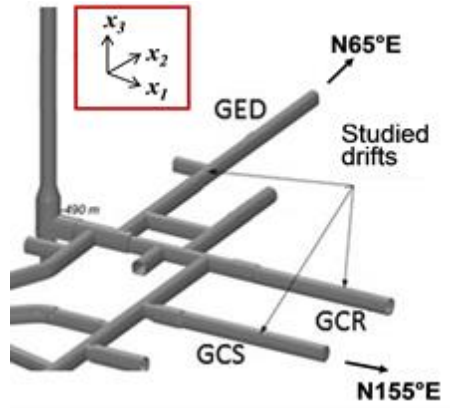
**Fig. 2. 8.** Local coordinates at the M/HM URL

Determination of the ellipse parameters:

An ellipse is defined with five parameters: the coordinates $X_c$ and $Y_c$ of the center, the minor semi-axis $a$, the major semi-axis $b$, and its orientation $\theta$ with respect to the horizontal in the reference coordinate system (Fig. 2.9). The procedure for the determination of these parameters begins with a systematic fitting of them for each convergence measurement:

- First, a fit is made on all 5 parameters. It shows that $Y_c$ (for drifts with the orientation of the major principal horizontal stress) or $X_c$ (for the drifts in the perpendicular direction) does not significantly change.
- Then, fixing $Y_c$ or $X_c$ (respectively), a second fit is made for the remaining four parameters. It shows that $\theta$ tends to stabilize with time towards an asymptotic value.
- Finally, fixing $\theta$ at this asymptotic value, a last fit is made for the three remaining parameters.
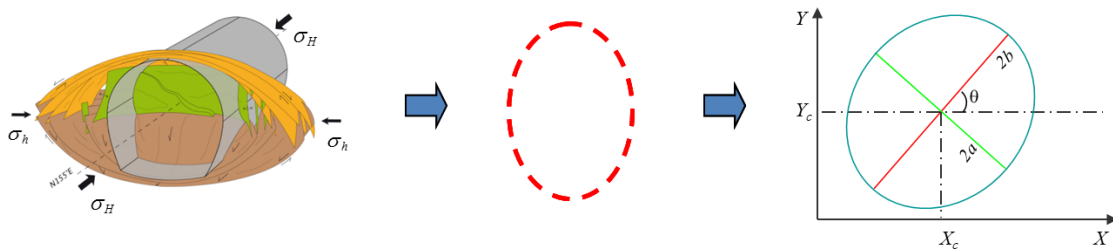


**Fig. 2. 9.** Identification of the main axes of deformation

This procedure permits to define the principal axes of the ellipse deformation and their evolution in time. Table 2.4 shows the results for the convergence measurement sections in the GCS drift. It is observed that the orientation $\theta$ of the major axis of the ellipse with respect to the horizontal

direction is about 90°, which is consistent with in-situ observations. The fracture network has a horizontal extent higher than the vertical one, as shown in Fig. 2.9. It is expected that the principal axes of the ellipse follow the vertical and horizontal orientations in the cross section. Indeed, the horizontal evolution of the ellipse is stronger than the vertical one. Therefore, the minor axis of the ellipse is horizontal and the major one is vertical. Parameters θ and $Y_c$ are kept constant as explained above and the three other parameters evolve in time. The evaluated ellipse parameters for the initial convergence measurement (using subscript *i*) and the final one (using subscript *f*) are given in Table 2.4.

The average ratio of the ellipse's vertical to horizontal axes' length evolution $(\beta = (b_f - b_i)/(a_f - a_i))$ is about 0.55. The heterogeneity of the rock formation can explain the dispersion in the deformation evolution, as mentioned before. Some other factors, such as some technical problems and site related practical difficulties, can also contribute to this dispersion. Moreover, the parameter $\beta$ for sections F (PM 52.9) and G (PM 57.7) is larger than the one of the other sections. This can be attributed to the fact that sections F and G are closer to the drift's end (at 10.4 m and 5.6 m respectively). The stress field around these sections is thus different from the other sections, and it is expected that the lateral extension of the fractured zone is smaller. As seen in Fig. 2.7a, the horizontal closure of the drift is indeed smaller in sections F and G than in the other sections, whereas the vertical closure is comparable.

**Table 2. 4.** Parameters of the fitted ellipse for GCS drift

| Section | PM | θ (°) | $Y_c$ (m) | $X_{ci}$ (m) | $a_i$ (m) | $b_i$ (m) | $X_{cf}$ (m) | $a_f$ (m) | $b_f$ (m) | $\beta$ |
|---------|------|-------|-----------|--------------|-----------|-----------|--------------|-----------|-----------|---------|
| B | 16.9 | 85 | -2.345 | -0.062 | 2.249 | 2.342 | -0.035 | 2.223 | 2.328 | 0.53 |
| C | 30.1 | 95 | -2.471 | 0.009 | 2.354 | 2.477 | -0.015 | 2.330 | 2.466 | 0.45 |
| D | 40.7 | 90 | -2.443 | -0.022 | 2.338 | 2.452 | 0.007 | 2.314 | 2.441 | 0.48 |
| E | 49.2 | 90 | -2.324 | -0.018 | 2.382 | 2.313 | -0.027 | 2.356 | 2.302 | 0.42 |
| F | 52.9 | 90 | -2.409 | 0.013 | 2.320 | 2.406 | 0.027 | 2.299 | 2.391 | 0.75 |
| G | 57.7 | 90 | -2.357 | -0.036 | 2.286 | 2.349 | 0.001 | 2.267 | 2.337 | 0.65 |

### 2.3.2.2. *Convergence evolution along the principal axes of deformation*

Using the semi-empirical law proposed by Sulem et al. (1987), presented in eq. (2.6), the convergence evolution is fitted independently for each axis of the ellipse. The total convergence in the long-term is given by eq. (2.7). The interpretation of the measured convergence must take into account the displacement that has occurred between the opening of the section and the installation of the convergence targets (i.e. 'lost convergence'). The recorded convergence is presented in eq. (2.8), where $x_0$ is the face distance for the first record reading and $t_0$ is the time elapsed since the face crossed the considered section.

$$\Delta C(x_i, t_i) = C(x_i, t_i) - C(x_0, t_0) \qquad (2.8)$$

By curve fitting of the analytical function (eq. 2.8) on the data, the optimal values of the five parameters $T$, $X$, $C_{\infty x}$, $m$ and $n$ can be obtained. This is performed independently for each axis of the ellipse and for each monitoring section of the drift. Appendix A.1 presents the method used for optimizing the fitting of these five parameters.

From the curve fitting results it is observed that for the two axes of the ellipse and for all sections, the parameters $X$, $T$, $m$ and $n$ are very close so that an average constant value can be assumed along the drift. Table 2.5 presents the results for the six sections in GCS drift. Only the parameter $C_{\infty x}$ changes in relation to local conditions in each cross section. It should be noted that the anisotropy of the convergence evolution is directly reflected in this parameter. Indeed, assuming that the parameter $m$ is the same in both directions, the ratio of the total convergence $C_{Total}$ in vertical and horizontal directions is the same as the ratio of $C_{\infty x}$. Its average value along the drift is 0.53. The evolution of the ellipse axes is very well reproduced as a function of time as well as a function of the distance to the face. Fig. 2.10 shows the convergence evolution for three different sections in GCS drift. The six different sections are presented in Appendix A.2.

**Table 2. 5.** Numerical values of the convergence law parameters in GCS drift

| | Section | | B | C | D | E | F | G |
|---|---|---|---|---|---|---|---|---|
| | PM | | 16.93 | 30.12 | 40.66 | 49.24 | 52.91 | 57.73 |
| | | | | | | | | |
| | $T$ | (days) | 6 | 6 | 6 | 6 | 6 | 6 |
| | $X$ | (m) | 4.6 | 4.6 | 4.6 | 4.6 | 4.6 | 4.6 |
| | $C_{\infty x}$ | (mm) | **14.0** | **10.9** | **11.1** | **12.7** | **9.3** | **9.7** |
| Minor axis (h) | $m$ | | 5.7 | 5.7 | 5.7 | 5.7 | 5.7 | 5.7 |
| | $n$ | | 0.3 | 0.3 | 0.3 | 0.3 | 0.3 | 0.3 |
| | $C_{Total}$ | (mm) | 93.6 | 72.8 | 74.1 | 84.9 | 62.4 | 65.1 |
| | $T$ | (days) | 6 | 6 | 6 | 6 | 6 | 6 |
| | $X$ | (m) | 4.6 | 4.6 | 4.6 | 4.6 | 4.6 | 4.6 |
| | $C_{\infty x}$ | (mm) | **7.5** | **5.0** | **5.3** | **4.8** | **6.5** | **6.4** |
| Major axis (v) | $m$ | | 5.7 | 5.7 | 5.7 | 5.7 | 5.7 | 5.7 |
| | $n$ | | 0.3 | 0.3 | 0.3 | 0.3 | 0.3 | 0.3 |
| | $C_{Total}$ | (mm) | 50.2 | 33.2 | 35.2 | 32.1 | 43.4 | 42.7 |
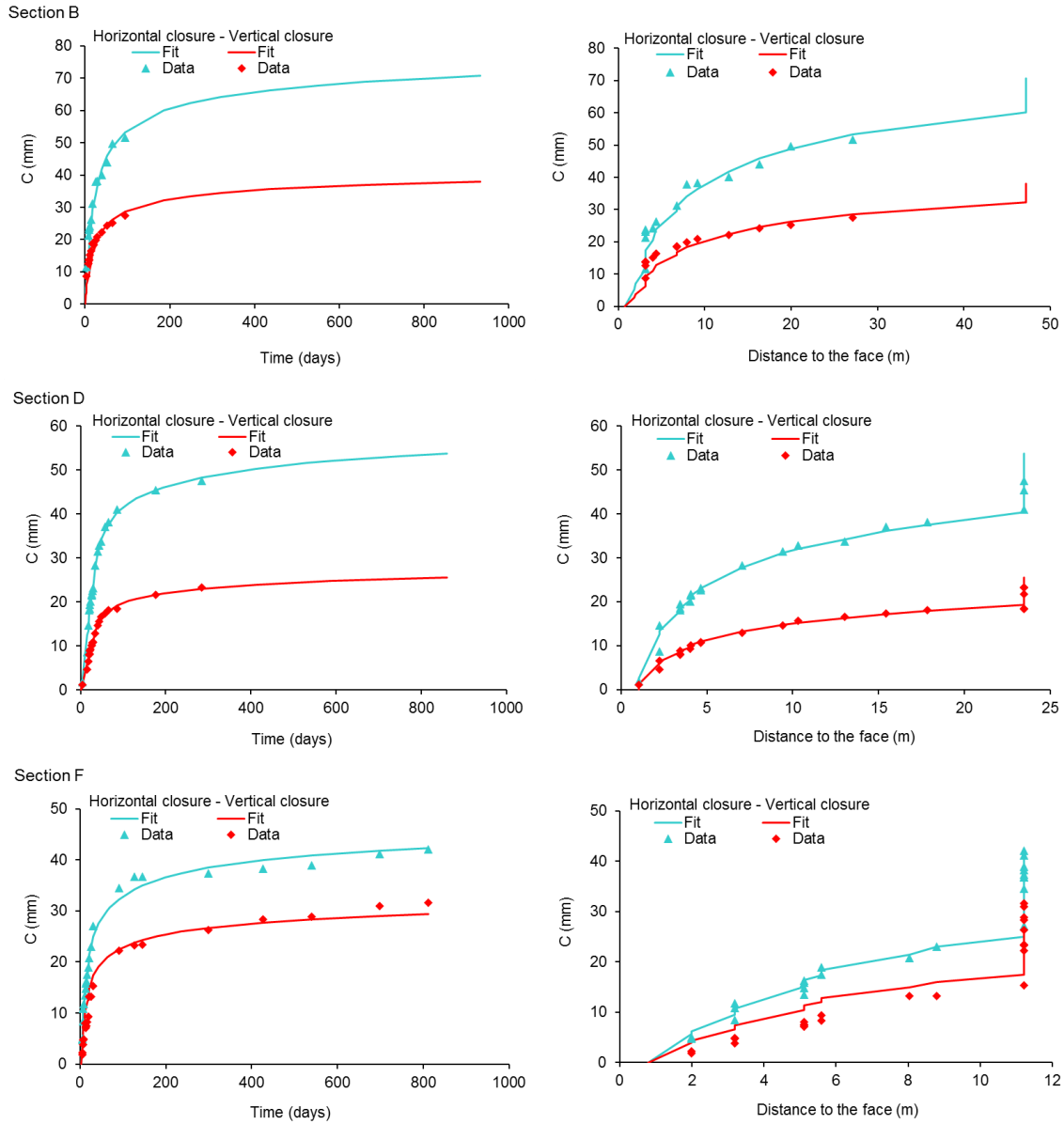
**Fig. 2. 10.** Convergence evolution in GCS drift. Left side: as function of time, Right side: as function of the distance to the face. Vertical and Horizontal convergence data as obtained by fitting an ellipse on the deformed drift section are represented with symbols. Convergence prediction as given by the convergence law (eq. 2.6 and eq. 2.8) is represented with continuous lines

Convergence predictability:

The continuous convergence monitoring during and after excavation is an important tool in the application of the observational method for tunnels design (Schubert 2008). Nevertheless, the question that arises is how much time of convergence monitoring is needed for an accurate prediction of convergence evolution in the long-term? To answer this question, for different time intervals (corresponding to the duration of convergence monitoring) from 10 to 100 days, the evolution of the ellipse axes is curve-fitted following the procedure explained above. Parameters *T, X, m* and *n* are kept constant along the drift (see Table 2.5) and only the parameter $C_{\infty x}$ is

back-calculated at each time interval. The evaluated parameters are then used to predict the long-term convergences which are presented in Fig. 2.11 for different time intervals in a section of GCS drift. The final convergence prediction and two lines corresponding to an error of ±10% are also shown in this figure. It is observed that by monitoring the convergence during about 40 days, the final closure of walls can be predicted with an error less than 10%. The other sections are presented in Appendix A.3
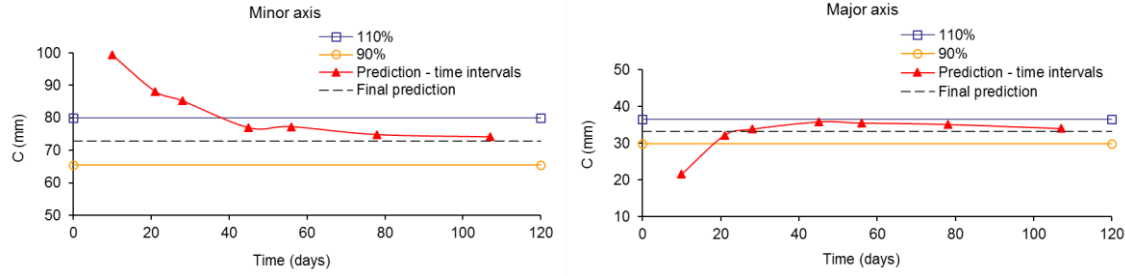


**Fig. 2. 11.** Final convergence predictions in a section of GCS drift as a function of the duration of the monitoring

### 2.3.3. Comparison with a drift following the direction of $\sigma_h$ and discussion of the results

#### 2.3.3.1. *GED drift results and comparison with GCS drift*

The same analysis of the convergence measurements, as explained in the previous section, has been performed for the GED drift. The parameters of the ellipse are summarized in Table 2.6. The initial shape of the drift is elliptic and it evolves following the same shape with the major axis forming an angle θ equal to 90° with respect to the horizontal axis (Fig. 2.12). As in the case of the GCS drift, the principal axes of the ellipse follow the vertical and horizontal orientations in the plane of the cross section. As mentioned in section 2.3.1 in the GED drift, stronger displacements are observed along the vertical axis which is in accordance with the fracture patterns observed in-situ (Fig. 2.12). The average ratio ( $\beta$ ) of ellipse vertical to horizontal axes' length evolution is about 4.1.

**Table 2. 6.** Parameters of the fitted ellipse for GED drift

| *Section* | *PM* | *θ (°)* | *$X_c$ (m)* | *$Y_{ci}$ (m)* | *$a_i$ (m)* | *$b_i$ (m)* | *$Y_{cf}$ (m)* | *$a_f$ (m)* | *$b_f$ (m)* | *β* |
|---|---|---|---|---|---|---|---|---|---|---|
| A | 19.5 | 90 | 0.028 | -2.393 | 2.089 | 2.394 | -2.325 | 2.074 | 2.325 | 4.64 |
| B | 35.5 | 90 | 0.015 | -2.343 | 2.063 | 2.343 | -2.302 | 2.046 | 2.302 | 2.47 |
| C | 51.5 | 90 | 0.000 | -2.333 | 2.301 | 2.332 | -2.273 | 2.290 | 2.273 | 5.31 |
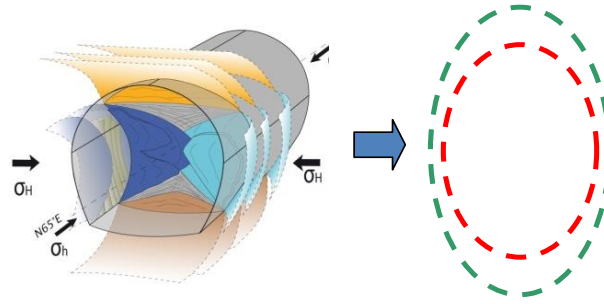
**Fig. 2. 12.** Ellipse evolution in GED drift

Concerning the values of the convergence law parameters for GED (Table 2.7) in the horizontal direction, it is obtained that $X$, $m$, $n$ and $T$ are the same as those obtained for GCS. In the vertical direction, we note that a higher value is obtained for the parameter $T$ which is in accordance with the in-situ observations. As explained above, the vertical displacement is stronger than the horizontal one. Even if the rate of convergence decreases in time, the vertical convergence continues to evolve with a higher rate than the horizontal one. To fit the data, only the parameter $C_{\infty x}$ is adjusted in each cross section, as in the GCS drift. This parameter gives a good description of the anisotropy of the convergence. Fig. 2.13 shows the convergence evolution as a function of time and as a function of the distance to the face in the GED drift. It is observed that the semi-empirical convergence law gives an excellent reproduction of the convergence evolution. This is an important result, as even if the different drifts present an anisotropic closure that depends of their orientation, it is possible to accurately predict the long-term closure of any drift section by fitting only $C_{\infty x}$. This parameter reflects the impact of the induced fractured zone on the drift closure and depends on the local conditions and drift orientation.

**Table 2. 7.** Numerical values of the convergence law parameters in GED drift

| | Section | | A | B | C |
|---|---|---|---|---|---|
| | PM | | 19.5 | 35.47 | 51.49 |
| | | | | | |
| | $T$ | (days) | 6 | 6 | 6 |
| | $X$ | (m) | 4.6 | 4.6 | 4.6 |
| | $C_{\infty x}$ | (mm) | **5.9** | **8.4** | **5.3** |
| Minor axis (h) | $m$ | | 5.7 | 5.7 | 5.7 |
| | $n$ | | 0.3 | 0.3 | 0.3 |
| | $C_{Total}$ | (mm) | 39.5 | 56.6 | 35.3 |
| | $T$ | (days) | 16 | 16 | 16. |
| | $X$ | (m) | 4.6 | 4.6 | 4.6 |
| | $C_{\infty x}$ | (mm) | **27.4** | **24.5** | **32.2** |
| Major axis (v) | $m$ | | 5.7 | 5.7 | 5.7 |
| | $n$ | | 0.3 | 0.3 | 0.3 |
| | $C_{Total}$ | (mm) | 183.8 | 163.9 | 215.5 |
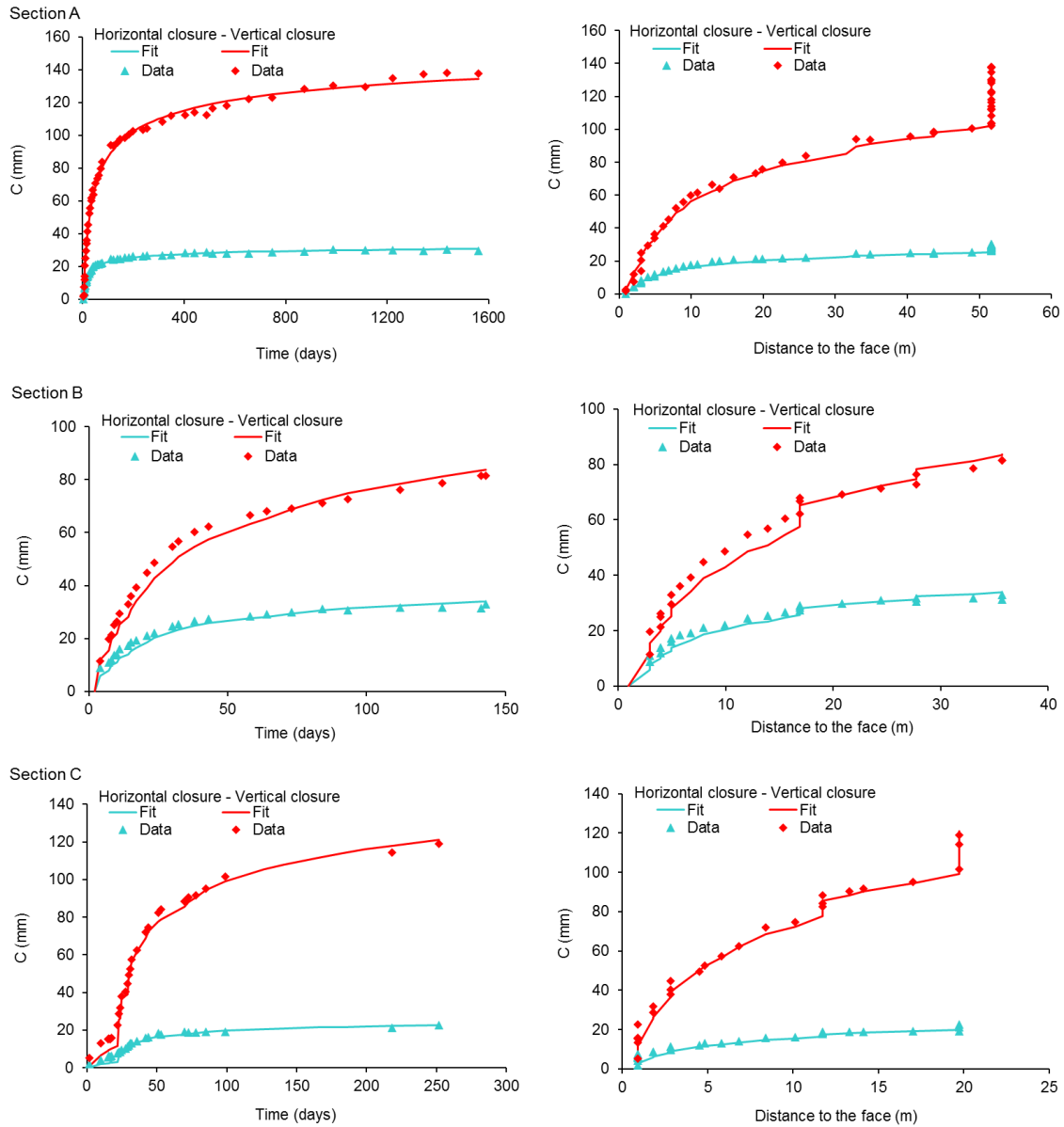
**Fig. 2. 13.** Convergence evolution in GED drift. Left side: as function of time, Right side: as function of the distance to the face. Vertical and Horizontal convergence data as obtained by fitting an ellipse on the deformed drift section are represented with symbols. Convergence prediction as given by the convergence law (eq. 2.6 and eq. 2.8) is represented with continuous lines

It should be noted that this analysis permits to reproduce very well the interruption of the excavation and its resumption after some time. This is observed by the change of slope of the convergence curves when the excavation is resumed. For example, in section C of GED drift, at about one meter from this section the excavation has been stopped during 20 days because of the installation of the SMR (see Fig. 2.13). Finally, it is found that with a convergence monitoring of about 40 days the final convergence can be predicted with an error less than 10%, as in GCS drift (Fig. 2.14). The other sections are presented in Appendix A.4.

60
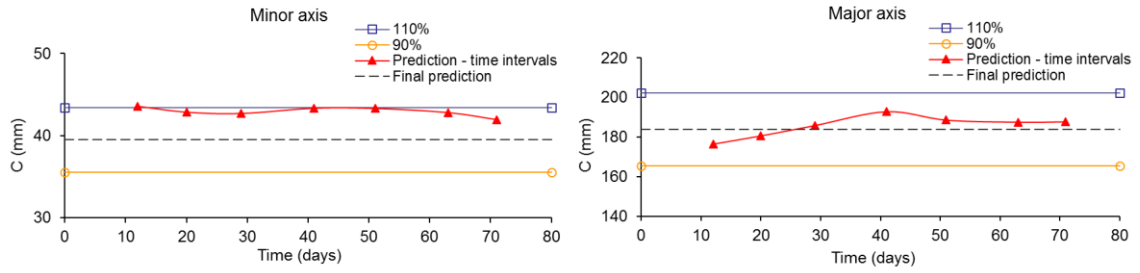
**Fig. 2. 14.** Final convergence predictions in a section of GCS drift as a function of the duration of the monitoring

### 2.3.3.2. *Face advance effect and time-dependent behavior of the ground*

Deformations due to the excavation of GCS drift have been monitored by an extensometer installed before the beginning of excavation. This extensometer is emplaced in a parallel neighboring drift and reaches GCS at PM 17.3 (Fig. 2.15). The extensometer starts to record radial displacements when the face is at 2.4 m (about one radius) ahead of the section. The deformations have then been monitored until today.
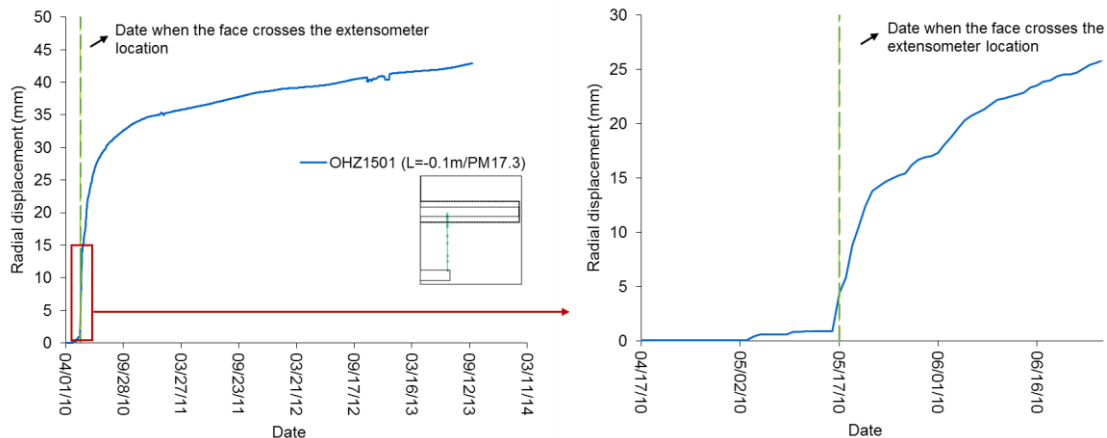


**Fig. 2. 15.** Radial displacement in GCS drift obtained from extensometer data (L - distance to GCS wall)

Section B in GCS drift is at PM 16.9, i.e. close to the extensometer. The closure data recorded in this section have been analyzed as explained in section 2.3.2. The horizontal displacement calculated by the semi-empirical convergence law, taking into account the lost convergence, has been compared to that recorded by the extensometer. The radial displacement of the drift wall is taken equal to half of the convergence. Note that, for comparing two sets of data, we have to take the same initial value, which corresponds to the date when the drift face crosses this section (May 17, 2010). At this date the radial displacement recorded by the extensometer is about 4.4 mm (Fig. 2.15). This 'initial' displacement corresponds to the one which occurs prior to the excavation of

61

the section. For the comparison, this initial displacement is subtracted from the extensometer data. It is observed that the total radial displacement obtained by the convergence law is very close to that obtained by the reinterpreted extensometer measurements, as shown in Fig. 2.16.
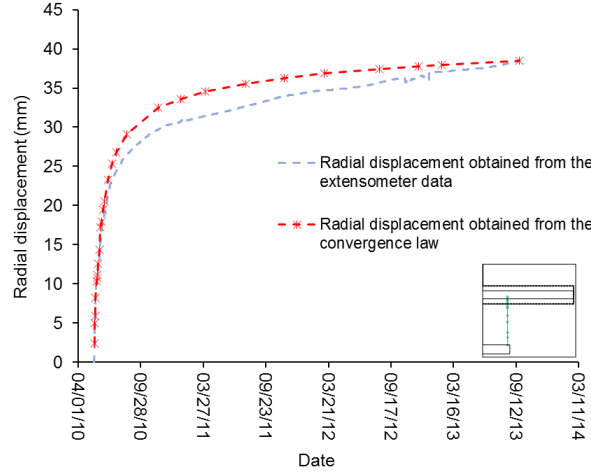


**Fig. 2. 16.** Radial displacement in GCS drift. Comparison between displacement obtained by the convergence law and displacement obtained from the extensometer data. The extensometer data are reinterpreted by subtracting the initial displacement which occurs prior to the excavation of the section

Armand et al. (2013) presented an analysis of the mine-by test and proposed a procedure to differentiate instantaneous and long-term responses for the radial displacements at the wall of GCS as recorded by the extensometer. This analysis is based on the real in-situ work sequence time schedule, with a separation of time of excavation from the other activities, such as support emplacement (shotcrete, rock bolt and concrete wedge emplacement), measurement, …. On average, the excavation time is around 15% of the full sequence of a step of excavation. In this view, the 'displacement jumps' occurring during the excavation work are separated from the continuous increase due to the deferred deformation observed in the remaining time of the excavation sequence (Fig. 2.17). The proposed convergence law also permits to distinguish between the instantaneous displacement $0.5 C_{\infty x}\left[1 - \left(X/(x+X)\right)^2\right]$, and the deferred response

$0.5\left(C(x,t) - C_{\infty x}\left[1 - \left(X/(x+X)\right)^2\right]\right)$ (Fig. 2.17). Note that, as explained above, to compare the displacements from Armand et al. (2013) to the displacements predicted from the convergence law, we have to take the same initial value. Thus, the results obtained by Armand et al. (2013) are reinterpreted. The radial displacement considered on May 17, 2010 is subtracted from the total radial displacement for the instantaneous and delayed response, respectively. It is observed that the instantaneous response obtained by the convergence law presents slightly lower values whereas the time-dependent response presents slightly higher values. This difference can be partly explained by the fact that in the methodology used by Armand et al. (2013), the recorded

displacement during each excavation step is assumed to be the sum of the instantaneous response recorded during the excavation work and time dependent displacement measured after. However, during an excavation step a time-dependent response also occurs, which is not taken into account by Armand et al. (2013). This results in a slight overestimation of the instantaneous response and an underestimation of the time-dependent response.
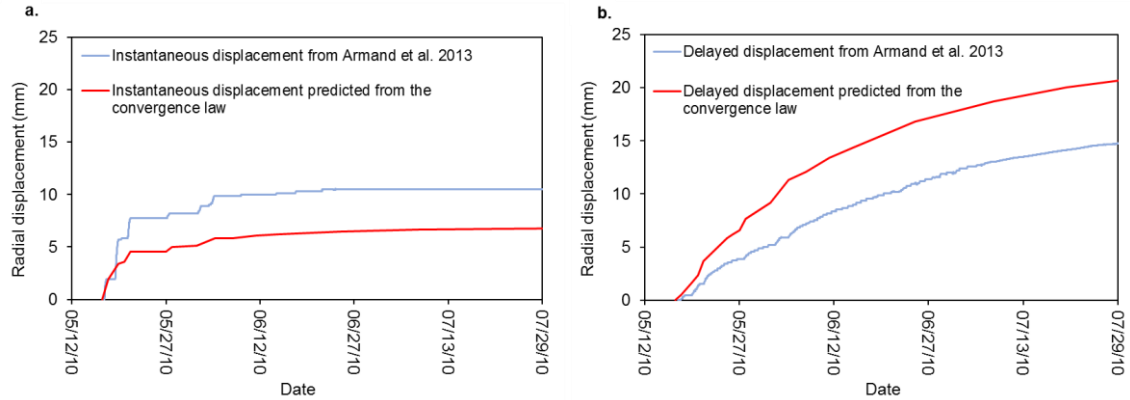


**Fig. 2. 17.** Radial displacement in GCS drift. – Results based on the convergence prediction as given by the convergence law (eq. 2.6 and eq. 2.8) compared to results obtained from Armand et al. 2013 (a. Instantaneous response. b. Delayed response). The results from Armand et al. 2013 are reinterpreted by subtracting the initial displacement which occurs prior to the excavation of the section

### 2.3.4. *Model validation*

The model is validated by comparing the predicted convergence to the one recorded in a different drift, named GCR, which is parallel to the GCS drift. As explained in section 2.1.2, this drift has the same kind of support as GCS and the support does not include yieldable concrete wedges between PM 47.5 and 58.3. Convergence has been monitored in three sections, of which, one monitoring section has been installed in the last part of the drift (with the stiffer support). This one permits to follow the influence of a different support in the convergence evolution. This stiffer support has an influence on the convergence evolution which will be reflected in a smaller value of the parameter $C_{\infty x}$. Convergence data have been analyzed as explained above by evaluating the elliptical deformation of the section. Table 2.8 summarizes the parameters of the evolution of the ellipse for GCR. The obtained ratio of vertical to horizontal convergence ( $\beta$ ) is about 0.59. Indeed, in-situ observations show that all drifts following this direction have a similar average ratio of vertical to horizontal closure.

**Table 2. 8.** Parameters of the fitted ellipse for GCR drift

| Section | PM | θ (°) | $Y_c$ (m) | $X_{ci}$ (m) | $a_i$ (m) | $b_i$ (m) | $X_{cf}$ (m) | $a_f$ (m) | $b_f$ (m) | β |
|---------|------|-----|--------|--------|-------|-------|--------|-------|-------|------|
| B | 22.1 | 80 | -2.460 | 0.006 | 2.425 | 2.457 | 0.030 | 2.406 | 2.443 | 0.74 |
| C | 43.6 | 95 | -2.520 | 0.032 | 2.623 | 2.525 | 0.024 | 2.607 | 2.516 | 0.58 |
| D | 53.2 | 90 | -2.505 | -0.024 | 2.403 | 2.526 | -0.014 | 2.389 | 2.520 | 0.46 |

The convergence law is then fitted on the data by keeping the parameters *T, X, m* and *n* constant and equal to their values obtained for GCS (Table 2.5). Only the parameter $C_{\infty x}$ is fitted on the data monitored during the first 40 days. Table 2.9 shows the results obtained for the three measurement sections in this drift.

**Table 2. 9.** Numerical values of the convergence law parameters in GCR drift (fitted on 40 days of monitoring convergence)

| | Section | | B | C | D |
|---|---|---|------|------|------|
| | PM | | 22.1 | 43.6 | 53.2 |
| | | | | | |
| | *T* | (days) | 6 | 6 | 6 |
| | *X* | (m) | 4.6 | 4.6 | 4.6 |
| Minor axis (h) | $C_{\infty x}$ | (mm) | **11.6** | **9.4** | **8.4** |
| | *m* | | 5.7 | 5.7 | 5.7 |
| | *n* | | 0.3 | 0.3 | 0.3 |
| | $C_{Total}$ | (mm) | 77.4 | 63.1 | 56.6 |
| | *T* | (days) | 6 | 6 | 6 |
| | *X* | (m) | 4.6 | 4.6 | 4.6 |
| Major axis (v) | $C_{\infty x}$ | (mm) | **9.5** | **5.4** | **3.8** |
| | *m* | | 5.7 | 5.7 | 5.7 |
| | *n* | | 0.3 | 0.3 | 0.3 |
| | $C_{Total}$ | (mm) | 63.6 | 36.3 | 25.4 |

The predictions have been compared to the convergence data, which have been recorded during six months (Fig. 2.18). In section B, the convergence measurements show a more isotropic response. It is observed that even if this section presents a different behavior in comparison with the other sections, adjusting the parameter $C_{\infty x}$ is enough to reproduce this behavior. Section D presents lower values of the convergence compared to the other sections in GCR and GCS drifts, which is due to the installation of a stiffer support. This is well reproduced by the model (smaller value of $C_{\infty x}$) and a very good prediction of the convergence is obtained (Fig. 2.18).
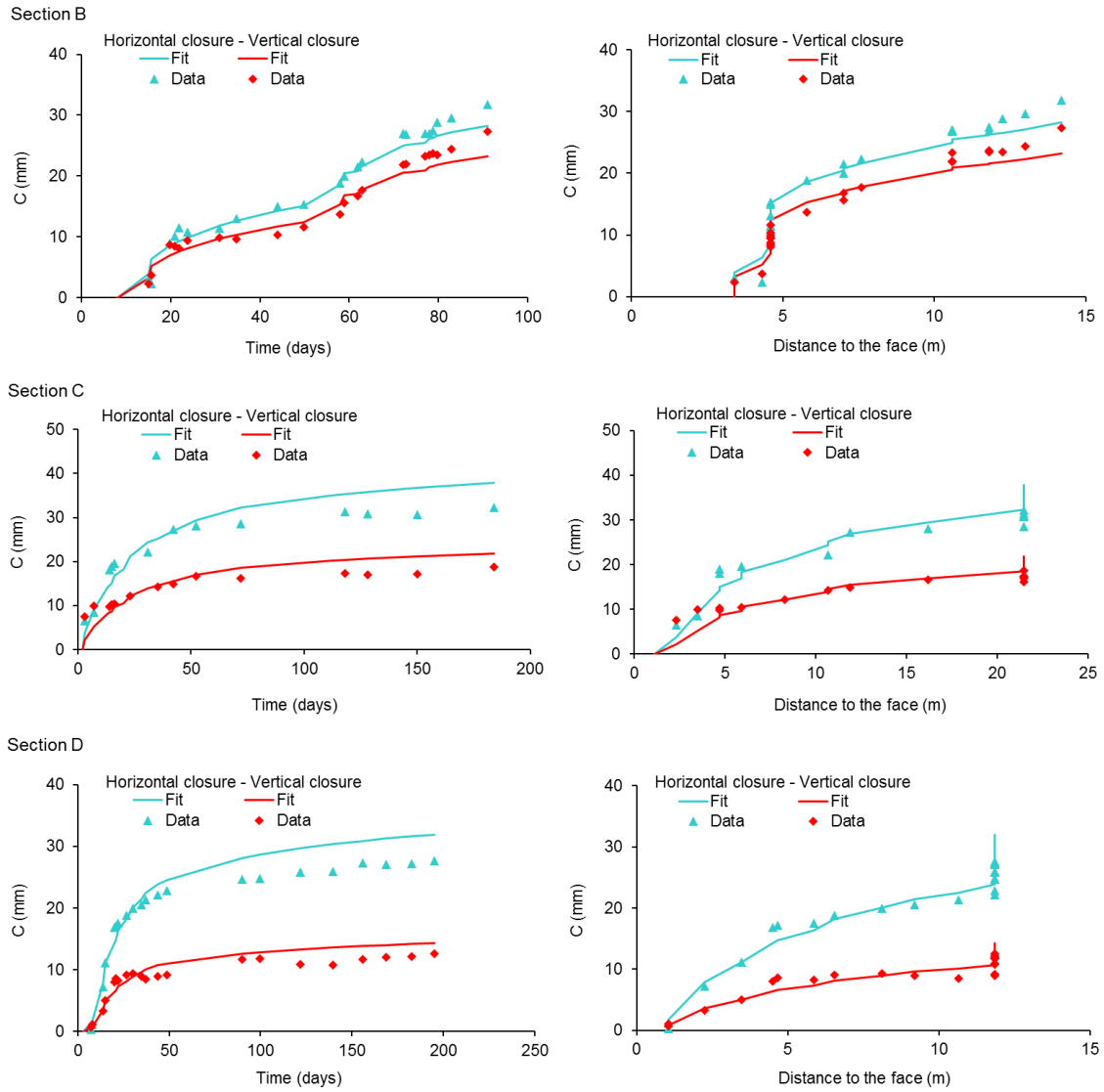
**Fig. 2. 18.** Convergence evolution in GCR drift. Left side: as function of time, Right side: as function of the distance to the face. Vertical and Horizontal convergence data as obtained by fitting an ellipse on the deformed drift section are represented with symbols. Convergence prediction as given by the convergence law (eq. 2.6 and eq. 2.8) is represented with continuous lines. Fitting of $C_{\infty x}$ is performed on the 40 first days of data

Table 2.10 shows the values of the predicted total convergence when taking into account all the convergence data (over the six months) for fitting parameter $C_{\infty x}$. The accuracy of the prediction can be quantified based on the data obtained for 40 days of monitoring. The difference is less than about 16% for all sections and for both drift directions. Thus it is concluded that, for practical applications, with only 40 days of monitoring the model can be applied for reliable predictions of the convergence evolution.

**Table 2. 10.** Numerical values of the convergence law parameters in GCR drift (fitted on six months of monitoring convergence)

| | Section | | B | C | D |
|---|---|---|---|---|---|
| | PM | | 22.1 | 43.6 | 53.2 |
| | | | | | |
| Minor axis (h) | $C_{\infty x}$ | (mm) | 12.8 | 8.4 | 7.5 |
| | $C_{Total}$ | (mm) | 85.4 | 56.0 | 50.0 |
| Major axis (v) | $C_{\infty x}$ | (mm) | 10.2 | 4.7 | 3.3 |
| | $C_{Total}$ | (mm) | 68.2 | 31.4 | 22.2 |

## 2.3.5. *Preliminary conclusions*

Convergence data of one representative drift in each direction of excavation, which has a soft support and with a diameter of about 5 m, are first analyzed through the identification of the principal axes of deformation. This is performed by fitting an ellipse on the deformed shape of the drift section as a function of time. It is observed that the principal axes of deformations follow the horizontal and vertical orientations in the plane of the drift section. Note that these principal deformation axes are in accordance with the fractures distribution around the drift (Armand et al. 2014). The evolution in time of the two axes of the ellipse is interpreted as the convergence of the drift wall along the two principal directions of deformation, and fitted using the convergence law proposed by Sulem et al. (1987). The convergence law parameters are evaluated for different drifts and for different monitoring sections in each drift. The results of the analysis, for all the monitored sections of the two drifts excavated in perpendicular directions, show that constant values for the parameters *X*, *m* and *n* can be assumed. Parameter *T* is constant along a drift and takes two different values. One value is obtained for the closure along the vertical and horizontal directions of GCS (excavated along the major horizontal stress) and along the horizontal direction of GED (excavated along the minor horizontal stress). The other value is obtained in the vertical direction of GED. This reflects the fact that the convergence recorded in the vertical direction of GED is not only stronger than the ones of GCS and GCR, but also exhibits the highest convergence rate (of about $1 \times 10^{-10} s^{-1}$ even after three years). The origin of this observation is not clearly understood, but it can be attributed to various factors such as (i) the different fracture patterns (extent and direction) of the different drifts (ii) the difference in the density of the excavation induced fractures, (iii) the influence of the drift geometry. The geometry of GED which is not perfectly circular generates stress concentration in the floor that induces a slight floor heave. A very good simulation of drifts closure is then obtained by only fitting the parameter $C_{\infty x}$. This parameter takes into account the anisotropy of the convergence and the dispersion in the deformation evolution along the different drifts. Thus, the semi-empirical convergence law permits to satisfactorily represent the anisotropic behavior of the rock mass formation by the

variation of this single parameter. We can thus consider that this single varying parameter reflects the local conditions whereas the other constant parameters are representative of the global response of the system rock mass - structure.

Moreover, the comparison of the results obtained from the analysis of the convergence measurements with the data obtained from the extensometer measurements shows that the convergence law permits to distinguish the instantaneous convergence induced by the excavation progress and the long-term convergence due to the rheological behavior of rock formation. This distinction is well reproduced by the model and a very good prediction of the convergence, and therefore the radial displacements, is obtained.

The model is validated by simulating the closure of a different drift (GCR) with the four parameters *X, m, n* and *T* obtained in GCS and by only fitting $C_{\infty x}$. It is shown that by monitoring convergence for about 40 days, the model can be applied for reliable predictions of the long-term convergence evolution.

## 2.4. Analysis of the convergence evolution for an unsupported micro-tunnel

Recent studies have been carried out to analyze the thermo-mechanical behavior of the micro-tunnels and the thermo-hydromechanical (THM) response of the surrounding rock, based on data recorded for a full scale disposal cell demonstrator developed in the M/HM URL (Morel et al. 2013). The short-term and the long-term behavior of the damage zone around micro-tunnels have been described based on an isotropic elastic-viscoplastic model (Renaud et al. 2010). However, the modeling of the anisotropic closure evolution in time remains a task to achieve. In the case of the micro-tunnels, it is observed that the ratio between the horizontal closure to the vertical one is larger than 5 and increases with time.

In this section, the convergence measurements in a micro-tunnel following the direction of the major principal horizontal stress are presented and analyzed. The horizontal convergence evolution is fitted using the law proposed by Sulem et al. (1987), as studied in the preceding section. Finally, the vertical convergence, which presents a very weak evolution in time, is analyzed independently on the basis of the closure rate.

### 2.4.1. In-situ observations

It is observed that the convergence is maximum in the horizontal direction and minimum in the vertical one. This behavior is observed for all the sections along the micro-tunnel and is similar to the observations performed in parallel drifts (with a diameter of about 5 m). Fig. 2.19 shows the data recorded for the section at PM 12 in ALC1603 micro-tunnel for the vertical, horizontal and transverse directions. The vertical and horizontal convergence data for the four sections along the micro-tunnel are presented in Fig. 2.20. It is observed that 80% of the total horizontal convergence occurs in the first six months of monitoring. Then, the deformation rate decreases with time and reaches values less than 1 mm per month after six months of monitoring. Furthermore, it is observed that the horizontal convergence is larger for the sections deeper into the rock mass. The convergence measurement section at PM 4 shows the lowest closure of walls while the monitoring section at PM 16 shows the highest closure. The origin of this observation is not clearly understood, but it can be attributed to the fact that the micro-tunnel is excavated in the lateral wall of a supported drift with a diameter of about 5 m, so that the stress field around the micro-tunnel is influenced by this drift in its vicinity (e.g. mainly in the section at PM 4). Similar observations have been performed in parallel micro-tunnels. Moreover, the discrepancy of closure evolution between the sections at PM 8, PM 12 and PM 16 can be related to the time elapsed between the excavation of the different sections. In fact, the excavation has been stopped for 31 hours at PM 13, after the opening of sections at PM 8 and PM 12 so that, there is a part of the convergence of these sections that is lost in the records. As explained above, the maximum closure rate occurs in the first days after excavation. Therefore, if the initial measurement is delayed for a section, a significant part of the total expected closure is lost. Finally, it is observed that the vertical convergence is almost nil during the first two months of monitoring and then it begins to increase with time at a rather slow rate. The data recorded for the vertical convergence will be presented in detail and analyzed independently in section 2.4.3.
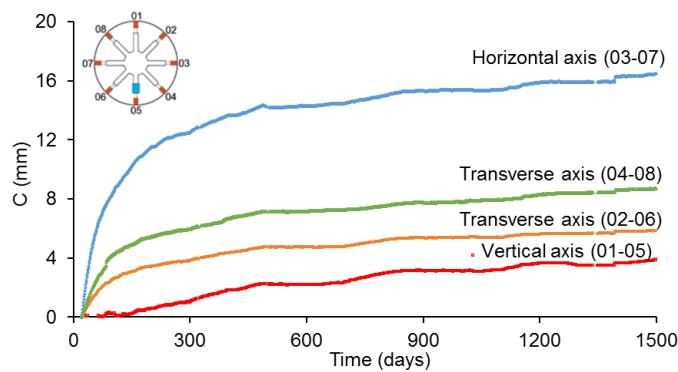


**Fig. 2. 19.** Convergence evolution in ALC1063 micro-tunnel. (Recorded in the convergence measurement section at PM 12 from the entrance of the drift)
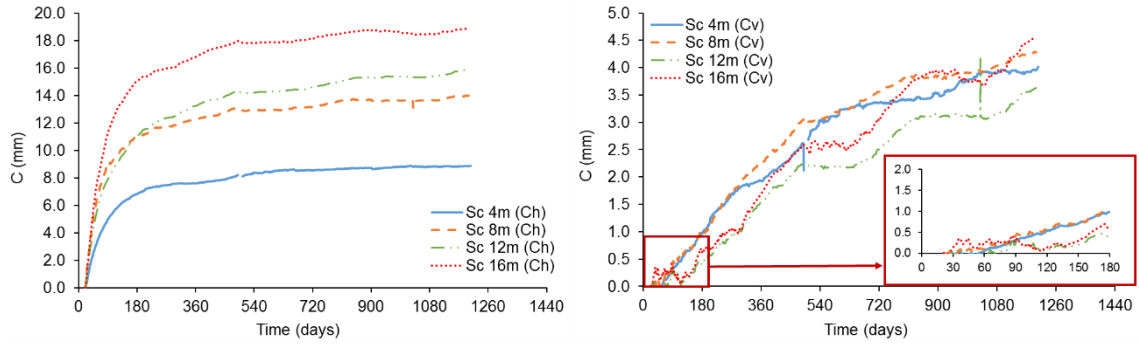
**Fig. 2. 20.** Convergence evolution in ALC1603 micro-tunnel. Left side: Horizontal convergence evolution, Right side: Vertical convergence evolution

### 2.4.2. *Analysis of the horizontal convergence of a micro-tunnel following the direction of $\sigma_H$*

As mentioned above, the convergence measurement devices have been installed three weeks after the end of the excavation. Thus, the recorded data only describe the time-dependent behavior of rock mass. As the face of the micro-tunnel is far enough from the convergence measurement sections, it has no influence on the convergence evolution. Therefore, the parameter *X*, which is directly related to the distance of influence of the face, cannot be estimated from these data. Accordingly, the recorded data will be analyzed taking only into account the part of the convergence law related to the time-dependent behavior as given in eq. (2.9).

$$C(t) = C_{\infty x} \left\{ 1 + m \left[ 1 - \left( \frac{T}{t+T} \right)^n \right] \right\} \tag{2.9}$$

The interpretation of the measured convergence must take into account the displacement that has occurred between the opening of the section and the installation of the convergence targets (the so-called 'lost convergence'). The recorded convergence is presented in eq. (2.10), where $t_0$ is the time elapsed since the face crossed the considered section. By fitting the mathematical function (eq. 2.10) to the measured data, the optimal values of the four parameters (*T*, $C_{\infty x}$, *m* and *n*) can be obtained.

$$\Delta C(t_i) = C(t_i) - C(t_0) \tag{2.10}$$

The results show similar values of parameters *T*, *m* and *n* for all sections. Thus, an average constant value of these parameters can be assumed along the micro-tunnel. Table 2.11 presents the results for the four sections in ALC1603 micro-tunnel. Only parameter $C_{\infty x}$ is fitted

independently in each cross section. This parameter reflects the impact of the induced fractured zone on the walls closure and depends on the local conditions of each section. As shown in Fig. 2.21, the evolution of the horizontal convergence is very well reproduced as a function of time for all convergence measurement sections along the micro-tunnel. Note that in this analysis the part of the instantaneous convergence induced by the excavation advance is lost.

**Table 2. 11.** Numerical values of convergence law parameters in ALC1603 micro-tunnel

| Section (PM) | *T* (days) | *m* | *n* | Horizontal convergence | |
|---|---|---|---|---|---|
| | | | | $C_{\infty x}$ (mm) | $C_{Total}$ (mm) |
| 4.0 | | | | 22.6 | 113.2 |
| 8.0 | 0.2 | 4.0 | 0.45 | 35.3 | 176.3 |
| 12.0 | | | | 38.6 | 193.3 |
| 16.0 | | | | 45.7 | 228.3 |
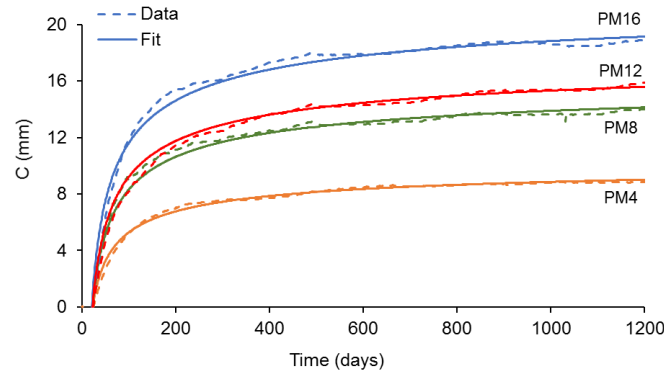


**Fig. 2. 21.** Horizontal convergence evolution in ALC1603 micro-tunnel. Convergence data are represented with dashed lines. Convergence prediction as given by the convergence law (eq. 2.9 and eq. 2.10) is represented with continuous lines. (Time-dependent response)

As explained above, the micro-tunnels and the drifts oriented along $\sigma_H$ both exhibit an anisotropic deformation with the horizontal closure stronger than the vertical one. In-situ observations show that for drifts and micro-tunnels following the direction of $\sigma_H$, the extent of the fractured zone is more developed in the horizontal direction, as explained in section 1.5.1 (Part I). Moreover, in-situ observations show that the closure anisotropy is stronger in the micro-tunnels than in the drifts. This can be related to the fact that in the vertical direction the closure of micro-tunnels is very weak and evolves very slowly in time. It is important to mention that for ALC1603 micro-tunnel, some rock blocks have fallen and breakouts were observed in due course of the excavation, mainly in the vertical direction of the cross section. This can be linked to the absence of rockbolts. A detailed description will be presented in the following for the analysis along the vertical axis of deformation.

In an attempt to compare the horizontal convergence evolution between the micro-tunnels and the parallel drifts, an analysis has been made based on the comparison of the convergence law parameters. It should be noted that the convergence monitoring in drifts started right after the passage of the front at each convergence measurement section, while for the micro-tunnels the convergence monitoring started some days after the end of excavation. Thus, the analysis of convergence evolution for the micro-tunnels differs from the analysis of the drifts, as explained above. However, a comparison can be performed based on the time-dependent response of the ground, which is described by the parameters *T*, *m* and *n* of the convergence law. A detailed comparison between all the studied drifts is presented in section 2.5.

### 2.4.3.  Convergence evolution along the vertical axis of deformation

As already mentioned, the vertical convergence presents a weak evolution in time. As shown in Fig. 2.20, after six months of monitoring the vertical convergence is about 1 mm while it is about 10 times higher in the horizontal direction. This different response in horizontal and vertical directions could be related to the different extent of the fractures network, which is mainly developed in the horizontal direction. Fig. 2.22 shows the fractures distribution around a micro-tunnel (ALC3005) excavated parallel to ALC1603. As explained by Marschall et al. (2006) and Blümling et al. (2007), the breakouts occurs mainly at locations where bedding planes are oriented tangential to the tunnel circumference; consequently, the breakouts will develop mainly in the vertical direction of the cross section. Indeed, some rock blocks fall and breakouts were observed in the upper part of the micro-tunnel, in due course of the excavation. Moreover, the occurrence of breakouts can also be related to the absence of rockbolts. As explained by Chappell (1989) and Blanco Martin et al. (2011b), rockbolts are very efficient for the stabilization of the rock mass and the improvement of its stiffness.



**Fig. 2. 22.** Induced fracture distribution around micro-tunnel ALC3005. It is observed the elliptical fracture distribution around the opening, with a larger extension in the horizontal direction. In the ascending vertical direction is observed the breakouts induced by the excavation

Moreover, it is most likely that in the first days, the measurement system is not yet in contact with the rock formation in the zones of breakouts or is disturbed by the fall of some blocks. This can explain why the vertical convergence measurements are almost zero during the first two months and then starts to increase later with a very slow rate. It is not possible to analyze this response with the above model as it is done in the horizontal direction. Therefore, an analysis based on convergence rate is proposed.

In drifts of about 5 m diameter, the convergence evolution is higher in the first days and then it stabilizes with time. After this period of time, the vertical convergence rate and the horizontal one have a similar evolution for the drifts parallel to micro-tunnels direction. As the fracture network around the excavation is similar and the main axes of deformation are in the horizontal and vertical directions for both, micro-tunnels and drifts, it is expected that the deferred vertical convergence also presents a similar response.

Taking into account the convergence recorded for more than three years, a comparison between the vertical convergence rate to the horizontal one is presented in Fig. 2.23. It is observed that after about six months of monitoring the convergence rate for the vertical and horizontal directions are comparable.
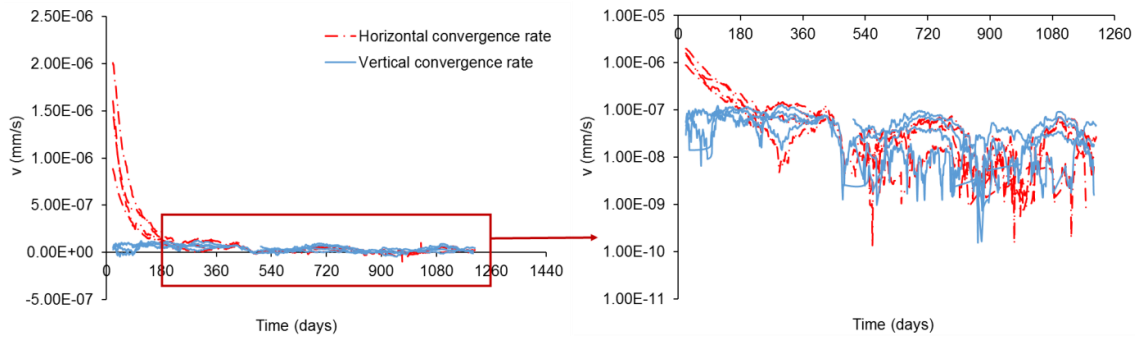


**Fig. 2. 23.** Convergence rate for vertical and horizontal evolution in ALC1603 micro-tunnel

Finally, an analysis of the vertical convergence is also performed for another micro-tunnel, ALC3005. This unsupported micro-tunnel is excavated in the face of a drift of about 5 m of diameter. The purpose of excavating this micro-tunnel in the face of a drift is to have a less disturbed initial state of stress. The excavation follows the direction of $\sigma_H$ on a length of 20 m. It is observed that the vertical displacement rate is comparable to the one observed in the parallel micro-tunnel ALC1603 (in the same time interval of monitoring), as shown in Fig. 2.24. Indeed, in-situ observations show that all micro-tunnels following this direction have a similar closure evolution. Therefore, as the deferred convergence evolution in the horizontal and vertical

directions are similar, the ratio of anisotropic closure can be directly related to the instantaneous response of the ground.
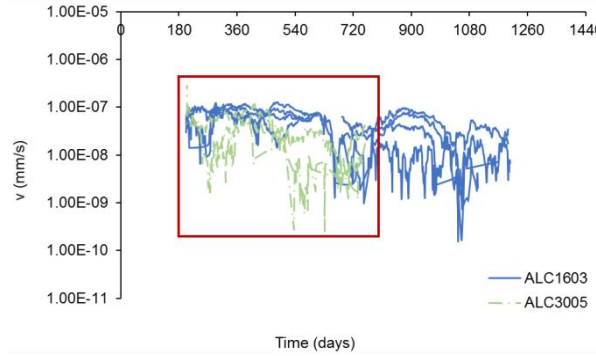


**Fig. 2. 24.** Vertical convergence rate evolution for ALC1603 and ALC3005 micro-tunnels

### 2.4.4. Preliminary conclusions

The in-situ measurements in the micro-tunnels show an anisotropic closure of walls, which evolves with time. The horizontal convergence shows stronger evolution, which is about 10 times higher than the vertical one after six months of monitoring. The ratio between the horizontal to the vertical convergence also evolves with time because the vertical convergence evolution is very weak. The first convergence measurement has been performed several days after the end of excavation. The analysis of the recorded data is thus mainly focused on the time-dependent behavior of the rock formation.

The horizontal convergence evolution is analyzed on the basis of the proposed convergence law. The four model parameters ($T$, $m$, $C_{\infty x}$ and $n$) are evaluated for different sections in the micro-tunnel. The results show close values for the parameters $T$, $m$ and $n$, which can be assumed as constant values along the micro-tunnel. A very good reproduction of convergence data can then be obtained by fitting a single parameter $C_{\infty x}$. This parameter allows to represent the dispersion observed in the different sections installed along the micro-tunnel, as it has been observed for parallel drifts of 5 m of diameter studied in the above section. A detailed comparison of the results obtained for this micro-tunnel with respect to parallel drifts with different sizes and support will be presented in the next section.

For analyzing the vertical convergence evolution, a comparison has been done between the convergence rate in the horizontal and vertical directions. It is shown that the vertical displacement rate is comparable to the horizontal one after about six months of monitoring. The disturbance induced by the excavation in the rock produces breakouts. Thus, monitoring of the

vertical convergence is disrupted if the measurement system is not in good contact with the rock formation in the breakouts zones or if it is disturbed by the falling of some rock blocks. However, it is very interesting to observe that, as for the parallel drifts, the deferred convergence evolution in the horizontal and in the vertical directions are similar. Therefore, the ratio of anisotropic closure can be directly related to the instantaneous response.

## 2.5.   Size effect on the convergence evolution

The main objective of this section is to analyze the size effect in the long-term anisotropic convergence evolution in drifts. To this aim, a direct analysis of the convergence measurements in two drifts (3.8 m and 6.3 m of diameter), excavated following the direction of the major horizontal principal stress ($\sigma_H$), is performed and compared to the analysis performed for a parallel drift of 5.2 m of diameter (GCS drift) and for a micro-tunnel of 0.74 m of diameter (ALC1603), which has been studied above. Moreover, the effect of the different support system and time of support installation will also be analyzed.

### 2.5.1.   In-situ observations

#### 2.5.1.1. *GRM3 drift*

For the first stage of excavation (3.8 m of diameter), the highest convergence is observed in the horizontal direction of the cross section, while the lowest convergence is observed in the vertical direction. Fig. 2.25a presents the horizontal and vertical convergence measurements recorded in the four SMCs installed along the drift. These observations are in accordance with the observations performed in parallel drifts at the M/HM URL (e.g. GCS drift and ALC1603 micro-tunnel). It should be noted that, for the GRM3-stage 1, the horizontal convergence is more pronounced in the low part of the section. This can be related to the fact that this drift does not have support in this part of the section, as shown in section 2.1.5. A significant scatter in the data can be observed, and this scatter is more important in the direction of stronger convergence. This is due, on one hand, to local heterogeneities of the rock formation and mainly to the scatter of the fractures' distribution around the drift. On the other hand, the convergence measurement sections were not all installed at the same distance from the face. Various factors can influence the distance or the time of installation of the convergence targets, as explained above. Finally, it should be noted that the sections close to the face (distance between 0 to 2 times the diameters) follow a partial deconfinement. Consequently, these sections exhibit less convergence (e.g. section I in GRM3).

For GRM3-stage 2, in an attempt to follow the influence of the enlargement of the cross section in the drift closure, four SMC have been installed very close to the SMC of GRM3-stage 1, as showed in Table 2.3. For the sake of simplicity, the analysis of the over-excavation in the following will be mainly based on the data recorded in the two central sections (i.e. SMC H1 and G1), to avoid the influence of proximity to the face. The measurements show a more isotropic convergence, with a higher evolution of the vertical convergence and a lower evolution of the horizontal one, as compared to GRM3-stage 1 and GCS drift. The vertical and horizontal convergence data are presented in Fig. 2.25b. In section 2.6, this data will be analyzed and compared to parallel drifts excavated in only one stage.
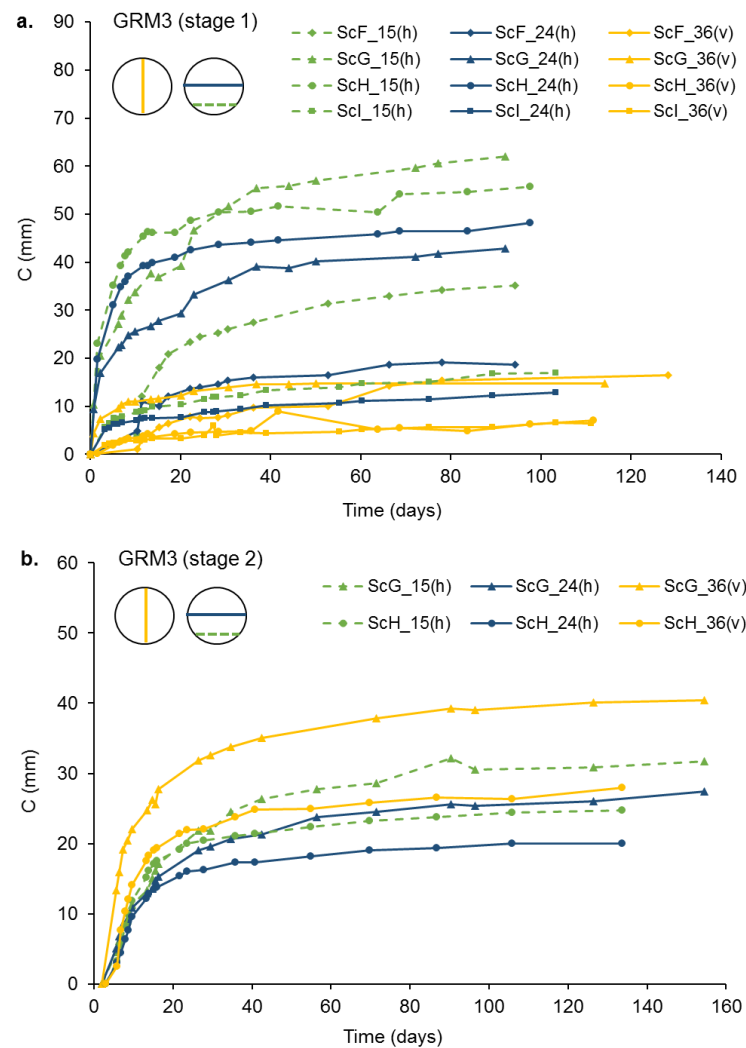


**Fig. 2. 25.** Convergence evolution in GRM3 drift: a. GRM3-stage 1. b. GRM3-stage 2

### 2.5.1.2. <u>GRD4 drift</u>

Because of the method of excavation, the convergence measurement sections were installed after the support installation. Consequently, an important part of the convergence is lost in the records. However, a horizontal extensometer was installed as a part of mine-by experiment in a neighbor drift, before the beginning of excavation. This extensometer is perpendicular to the left wall of GRD4 drift. As explained by Armand et al. (2011), the extensometers of mine-by test permit to follow the deformations of the rock mass induced by the excavation progress and their evolution in time. Therefore, in the following, the analysis of the closure evolution of this drift is based on the analysis of the radial displacements recorded by this extensometer.

The extensometer reaches GRD4 drift wall orthogonally at PM 15.7. The extensometer starts to record radial displacements when the face is at about 3 m ahead of the section (about one radius). A high displacement rate is observed during the first three weeks after excavation. This is the time elapsed between the passage of the tunnel face and the installation of support. During this period of time, a significant part of the deconfinement is done. Then, it is observed that the rock mass formation comes into contact with the support. Fig. 3.26 presents the radial displacements recorded at the drift wall, after the passage of the tunnel face. Very low rate of radial displacements are observed after the support system takes in charge the radial displacement when the complete contact between rock mass and support system is reached.
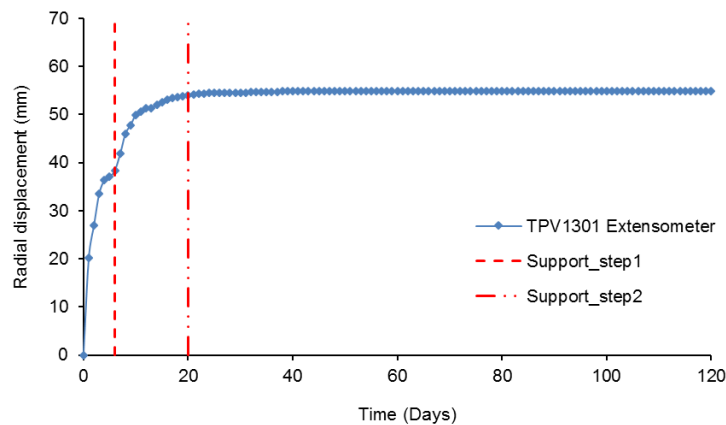


**Fig. 2. 26.** Radial displacement recorded for GRD4. Support_step1 is the time when the support installation began. Support_step2 is the time when the entire support is completed and functional

Comparing with parallel drifts (e.g. GRM3-stage 1 and GCS), at a same time after the passage of the face, and taking the radial displacement equal to half of the convergence, it is observed that

the radial displacements are higher in GRD4. This response of the rock formation can be directly related to the late installation of support in GRD4 drift.

### 2.5.2. *Analysis of the convergence evolution*

For the purpose of clarity, data analysis of GRM3-stage 1 and GRD4 drifts is performed and compared with drifts having similar support (i.e. GRM3-stage 1 compared to GCS drift and GRD4 drift compared to ALC1603 micro-tunnel). Then, in section 2.5.3, a discussion of the results and a detailed comparison between four drifts will be presented.

#### 2.5.2.1. *GRM3-stage 1 drift results and comparison with GCS drift*

From the curve fitting results in GRM3-stage 1, it is observed that for the two axes of the ellipse and for all sections along the drift, the parameters *X*, *T*, *m* and *n* are very close so that an average constant value can be assumed. Note that, parameter *X* is defined as 0.9 times the diameter of drift. Table 2.12 presents the results for the four sections in GRM3-stage 1 drift. Only the parameter $C_{\infty x}$ changes in relation to local conditions in each cross section. Therefore, as explained above, the anisotropy of the convergence evolution is directly reflected in this parameter. The ratio of the total convergence $C_{Total}$ in the vertical direction with the horizontal one is the same as the ratio of $C_{\infty x}$, which has an average value along the drift of about 0.3. The evolution of the ellipse axes is very well reproduced as a function of time as well as a function of the distance to the face. Fig. 2.27 shows the convergence evolution for two different sections in GRM3-stage 1 drift.

**Table 2. 12.** Numerical values of convergence law parameters in GRM3-stage1 drift

| Section | PM | *T* (days) | *X* (m) | *m* | *n* | Minor axis (h) | | Major axis (v) | |
|---|---|---|---|---|---|---|---|---|---|
| | | | | | | $C_{\infty x}$ (mm) | $C_{Total}$ (mm) | $C_{\infty x}$ (mm) | $C_{Total}$ (mm) |
| F | 12.9 | | | | | 13.6 | 90.9 | 3.5 | 23.3 |
| G | 25.7 | | | | | 20.8 | 139.0 | 5.7 | 38.3 |
| H | 36.2 | 6 | 3.4 | 5.7 | 0.3 | 19.0 | 127.3 | 2.3 | 15.4 |
| I | 43.7 | | | | | 6.0 | 40.2 | 2.8 | 18.7 |
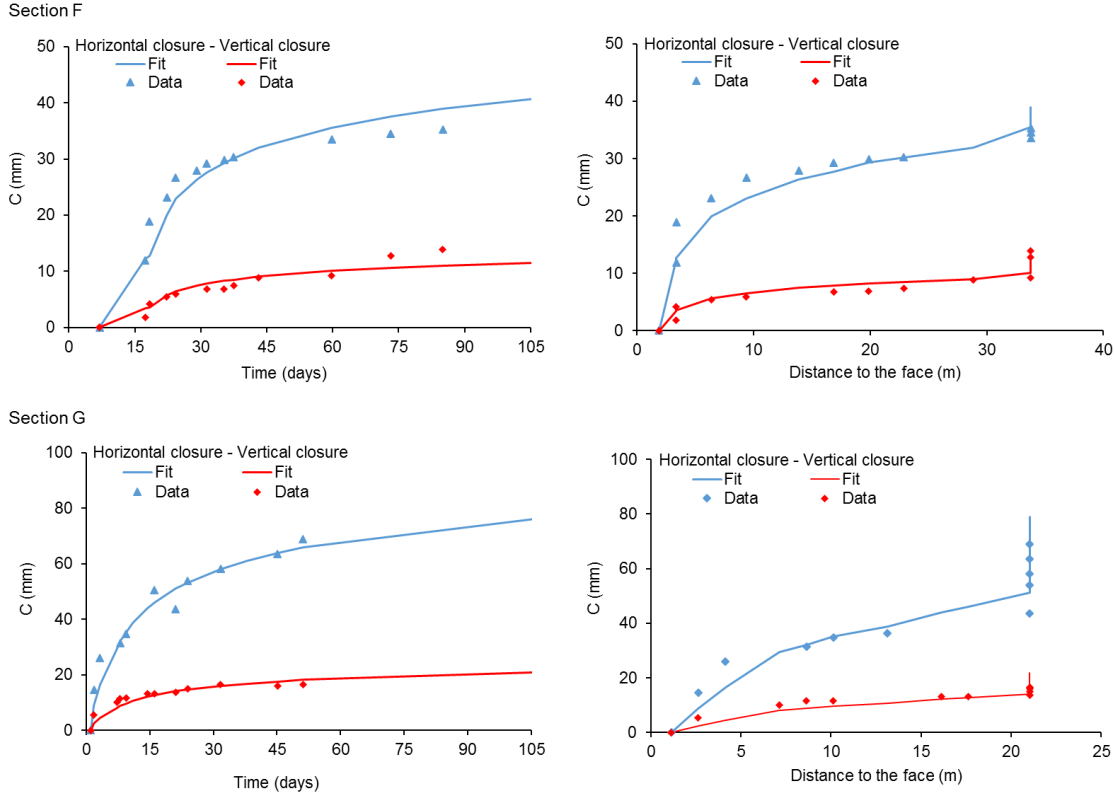
**Fig. 2. 27.** Convergence evolution in GRM3-stage1 drift. Left side: as a function of time, Right side: as function of the distance to the face. Vertical and horizontal convergence data as obtained by fitting an ellipse on the deformed section are represented with symbols. Convergence prediction as given by the convergence law (eq. 2.6 and eq. 2.8) is represented with continuous lines

Similar observations have been performed in GCS drift, which has a similar sequence of excavation and a similar support. The values of the semi-empirical law obtained for GCS drift, presented in section 2.3.2, are very close. Indeed, parameter $T$, $m$ and $n$ have the same value in both drifts and the parameter $X$ is defined as 0.9 times the diameter. Only the parameter $C_{\infty x}$ changes. Therefore, the average value of $C_{\infty x}$ ratio in vertical and horizontal directions is about 0.5 for GCS drift. The difference between the average values, which is lower in the GRM3-stage 1, can be related to the fact that this drift does not have any support in the lower part of the section. Therefore, a high horizontal convergence is observed in the lower part of GRM3-drift, while the vertical convergence presents a similar evolution in both drifts. This is reflected in the relationship between $C_{\infty x}$ and the diameter of drifts (see Table 2.14).

### 2.5.2.2. *GRD4 drift results and comparison with ALC1603 micro-tunnel*

As explained above, for GRD4 drift the analysis is based on the radial displacements recorded by a horizontal extensometer, which arrives at the drift wall at PM 15.7. Assuming that the drift

follows a similar closure in the horizontal direction of the cross section, the horizontal convergence is taken as two times the recorded data. The convergence analysis is then performed using the semi-empirical law proposed by Sulem et al. (1987). As the installation of support is performed a couple of days after the passage of the tunnel face, a high convergence rate is observed during the first days after the opening of the section. About 20 days after the passage of the face, the entire support is completed and functional. Then, it is observed that the convergence evolution stabilizes very fast with time. The analysis of the convergence evolution is thus performed in two steps: before and after the support installation.

Table 2.13 shows the evaluated values of convergence law parameters. From the curve fitting results, it is observed that before the installation of the support, the parameters are very close to those obtained for the parallel ALC1603 micro-tunnel, which is unsupported. It should be noted that for this micro-tunnel only the parameters related to the time-dependent behavior have been evaluated (Table 2.14). It is found that the values of parameters $T$ and $m$ are similar and can be kept constant. These parameters can be considered as representatives of the time-dependent behavior of drifts excavated without any support or with a late support installation. Moreover, the parameter $X$ keeps the same relation as in the parallel drifts, defined as 0.9 times the diameter of each drift. The parameter $n,$ which defines the final form of the fitted curve, presents a lower value in the drift. This can be related to the difference in the deconfinement rate which can be influenced by the excavation rate. In fact, the rate of excavation of GRD4 drift is about 3.8 m/week ($\approx$ 0.6 times the diameter per week), while it is about 0.6-0.7 m/h ($\approx$ 0.9 times the diameter per hour) for ALC1603 micro-tunnel. Finally, the parameter $C_{\infty x}$ is fitted independently in each cross section. The high deconfinement rate observed in the micro-tunnel is also reflected in a higher relationship between the instantaneous convergence and the excavation diameter.

After the support installation, it is observed that some values of convergence law parameters change. In fact, the rigid support takes in charge a part of the deconfinement, which can be reflected in a lower convergence evolution than those predicted without support. Moreover, the support controls a part of the deconfinement induced by the face advance, which is reflected in a diminution on the value of parameter $X$. The instantaneous convergence $C_{\infty x}$ will be also limited by the installation of support, as it is observed in the results (Table 2.13). Furthermore, the relationship between the total convergence and the instantaneous convergence will be lower. Therefore, the parameter $m$ also decreases. Finally, the fast stabilization in time with a very low rate of convergence can be reproduced by a higher value of parameter $n$. Then, taking into account both parameter sets, the convergence evolution is very well reproduced as a function of time and as a function to the distance to the face (Fig. 2.28).

**Table 2. 13.** Numerical values of convergence law parameters in GRD4 drift

| Support installation | $T$ (days) | $X$ (m) | $m$ | $n$ | Horizontal convergence | |
|---|---|---|---|---|---|---|
| | | | | | $C_{\infty x}$ (mm) | $C_{Total}$ (mm) |
| Before | 0.2 | 5.6 | 4.0 | 0.3 | 33.5 | 167.5 |
| After | | 1.2 | 3.7 | 0.9 | 28.0 | 131.9 |
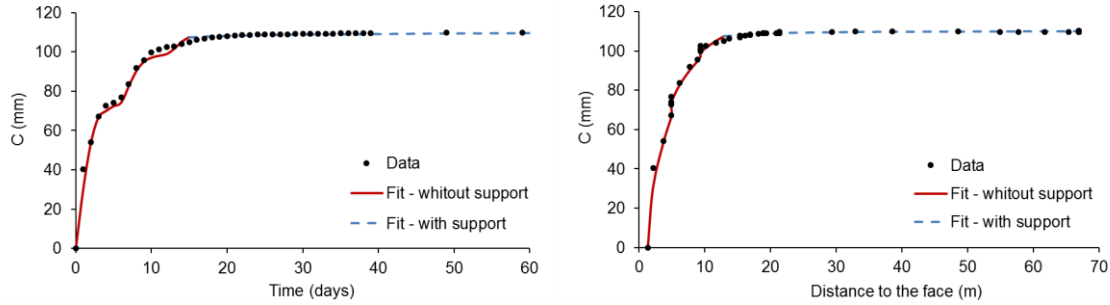


**Fig. 2. 28.** Horizontal convergence evolution in GRD4 drift. Left side: as a function of time, Right side: as function of the distance to the face. Recorded data are represented with symbols. Convergence prediction as given by the convergence law is represented with continuous lines (before the support installation) and with dashed lines (after the support installation)

## 2.5.3. Discussion of the results

The present analysis allows to improve our knowledge about the excavation size effect and the effect of the time elapsed for the installation of support in the convergence evolution in time. It is observed that for parallel drifts excavated and supported similarly, the parameters related to the time-dependent convergence evolution can be assumed as constant values. The obtained values suggest that, for drifts following the same sequence of excavation, the time-dependent behavior is size independent. Moreover, it is observed that the set of convergence law parameters for the drifts or micro-tunnels following the direction of $\sigma_H$, depends on the presence of support (Table 2.14).

Comparing the recorded data by extensometers of mine-by test for GCS drift and GRD4 drift (Fig. 2.29), it is observed that the radial displacement rate is very high for GRD4 during the first 20 days, then it stabilizes quickly with time. GCS drift, which has a flexible support, presents a different displacement rate, which is still going towards stabilization but with a lower rate than the one of GRD4 during the first few days and a higher rate later. For the comparison between the two drifts, the radial displacements are normalized to the drifts radius. The different response of the drifts is directly reflected in the values of the convergence law parameters. As GRD4 drift is unsupported during the first three weeks after the passage of tunnel face, a higher convergence rate was observed during the first days after the opening of the section and stabilization of the

80

convergence with time was faster. Therefore, lower values of *T* and *m* are obtained (Table 2.14). Furthermore, it is observed that the closure evolution is higher in the GRD4 drift than in GCS drift, which is directly reflected in the value of parameter $C_{\infty x}$. Indeed, the ratio of $C_{\infty x}$ over the diameter of the excavation is higher for GRD4 drift. This higher closure of the tunnel walls can be attributed to the fact that the GCS drift's support is installed after each step of excavation, while for GRD4 drift the support is installed when a high part of the deconfinement is already achieved.

**Table 2. 14.** Comparison of numerical values of convergence law parameters in different drifts

| Drift | *X*(m) | *T* (days) | *m* | *n* | Horizontal convergence $C_{\infty x}/D$ (%) | Vertical convergence $C_{\infty x}/D$ (%) |
|---|---|---|---|---|---|---|
| GRM3-stage1 | | 6 | 5.7 | 0.3 | $\approx 0.39$ | $\approx 0.09$ |
| GCS | $0.9 \times D$ | | | | $\approx 0.22$ | $\approx 0.11$ |
| GRD4-bs[1] | | 0.2 | 4.0 | 0.3 | $\approx 0.55$ | - |
| ALC1603 micro-tunnel | - | | | 0.45 | $\approx 5.0$ | - |

[1] Before the support installation
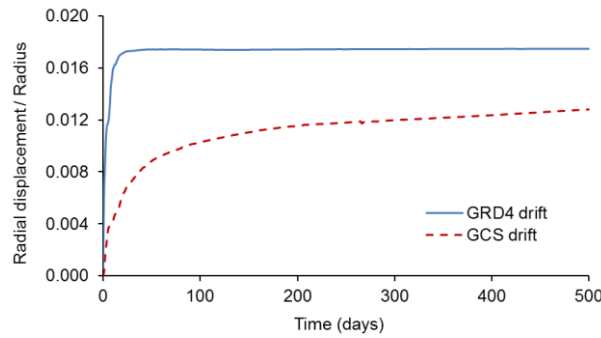


**Fig. 2. 29.** Comparison between GRD4 and GCS drifts. Radial displacement normalized to radius drift

It is important to mention that, for ALC1603 micro-tunnel and GRD4 drift, some rock blocks have fallen and breakouts were observed in due course of the excavation, as presented in the section below. This can be linked to the absence of rockbolts. Consequently, as a part of the fractured rock is fallen down in GRD4 and ALC1603, it can be expected that the remaining rock mass be less damaged and presents a lower potential for time-dependent deformations. Moreover, ALC1603 micro-tunnel and GRD4 drift present important displacement comparing to other studied drifts. Even if any significant evolution of damaged zone is not yet observed, this important wall displacement may provoke later additional damage and further time-dependent displacement. The obtained results must thus be considered with caution.

### 2.5.4. *Preliminary conclusions*

The parameters of the convergence law are evaluated for different sections in two different drifts (GRM3-stage 1 and GRD4 drifts, 3.8 m and 6.3 m of diameter respectively) and are compared to drifts studied in the previous sections (i.e. GCS drift and ALC1603 micro-tunnel, 5.2 m and 0.74 m of diameter respectively). The results show that drifts which are excavated and supported similarly present close values for the parameters related to the time-dependent behavior (*T* and *m*), which can be assumed as constant values along each drift and for all the parallel drifts. Furthermore, the parameter *X* (related to the distance of influence of the face and the extent of the decompressed zone around the drift) can be considered around 0.9 times the diameter of each drift. Thus, the obtained model parameters values are size independent for drifts with similar excavation method and support system. However, it is observed that the set of values for convergence law parameters depends on the time elapsed for the support installation and also on the change of excavation rate, which play a key role in the time-dependent convergence evolution of the ground.

## 2.6. **Effect of an enlargement of cross section on the convergence evolution**

As explained in section 2.1.5, a DPC experiment (preliminary deconfinement before tunnel excavation to the final diameter) was performed in the M/HM URL. As the analysis of convergence evolution of the first stage of excavation (e.g. GRM3-stage 1) has been presented in section above, the analysis performed for the second stage of excavation and a comparison with parallel drifts excavated in only one stage are presented in this section.

### 2.6.1. *Analysis of the convergence evolution in GRM3-stage 2*

As it is observed that the GRM3-stage 2 exhibits a more isotropic closure, the recorded data are fitted by considering a circular deformation pattern. For each convergence measurement the parameters of the fitted circle are determined: the center coordinates ($X_c$ and $Y_c$) and the radius (*r*). Then, the evolution of the circle radius is fitted to eq. (2.8), as explained above (section 2.3). It is observed that the values of parameters *T* and *m* decrease (Table 2.15). This expresses that the convergence tends to stabilize faster than the parallel drifts, which have been excavated in one single stage. Fig. 2.30 shows the convergence evolution for the two studied sections in GRM3-stage 2. It is observed that with the change of these parameters values, the convergence is very well reproduced as a function of time as well as a function of the distance to the face. This suggests that the enlargement of cross section could limit the delayed response of the ground.

**Table 2. 15.** Numerical values of convergence law parameters in GRM3-stage 2 drift

| Section | PM | *T* (days) | *X* (m) | *m* | *n* | $C_{\infty x}$ (mm) | $C_{Total}$ (mm) |
|---------|------|-----|-----|-----|-----|------|------|
| G1 | 25.9 | | | | | 8.8 | 44.2 |
| H1 | 36.2 | **2.5** | 4.6 | **4.0** | 0.3 | 8.5 | 42.4 |
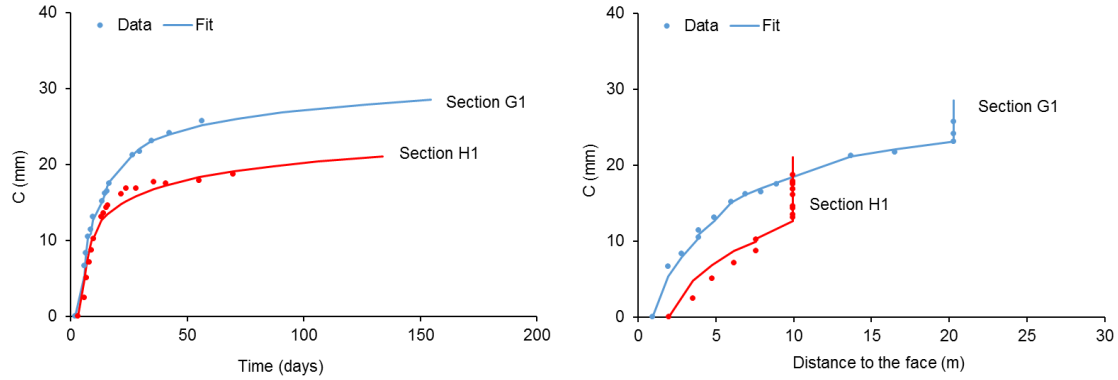


**Fig. 2. 30.** Convergence evolution in GRM3-stage 2 drift. Left side: as a function of time, Right side: as function of the distance to the face. Convergence data as obtained by fitting a circle on the deformed section are represented with symbols. Convergence prediction as given by the convergence law is represented with continuous lines

For the drifts following the same direction and with a flexible support installed after each step of excavation, 80% of the recorded convergence measurements occurs during the first 100 days after the excavation. The convergence rate then decreases with time and presents similar magnitudes in the vertical and horizontal directions, as explained above. Therefore, it is observed that the anisotropic response is mainly due to the instantaneous response induced by the excavation. In the case of the enlargement of cross section, which started three months after the end of the stage 1, a major part of the deconfinement has already occurred. Thus, the convergence rate is more isotropic.

## 2.6.2. *Comparison with parallel drifts*

In an attempt to compare the convergence evolution between drifts, an analysis has been made by normalizing the parameters of the convergence law *X*, $C_{\infty x}$ and $C_{Total}$ with the tunnel section diameter and the time with parameter *T* (Fig. 2.31). It is observed that the horizontal convergence in stage 1 is higher and has a higher dispersion than in stage 2. This can be related to the difference of supports, which are more flexible in stage 1. The vertical convergence also shows a higher dispersion along the drift in stage 1. However, it tends to be lower than in stage 2. As mentioned above, the closure of the drift in the stage 2 is more isotropic, with a higher closure in

the vertical direction of the cross section and a lower closure in the horizontal one. Comparing the results with GCS drift, which has a similar diameter (5.2 m) and a comparable support, it is observed that the horizontal convergence in stage 2 is lower. Indeed, in stage 2 the drift is already partially deconfined by the excavation of stage 1. Thus, the convergence evolution tends to stabilize faster, as explained above. The faster stabilization of convergences is reflected in a lower value of the total convergence. Table 2.16 shows the values of the convergence to diameter ratio ($C/D$).
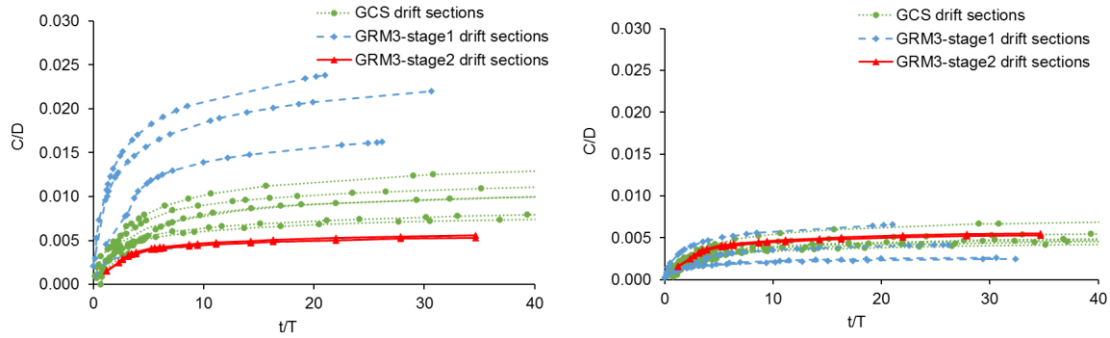


**Fig. 2. 31.** Convergence evolution to diameter of drift ratio. Comparison of GRM3-stage 2 with GRM3-stage 1 and GCS drifts, based in the convergence predictions obtained.  Left side: horizontal convergence evolution, Right side: vertical convergence evolution

**Table 2. 16.** Convergence to diameter ratio. Comparison between GRM3-stage 2 and GCS drifts

| Drift | Horizontal closure | | Vertical closure | |
|---|---|---|---|---|
| | $C_{\infty x}/D$ (%) | $C_{Total}/D$ (%) | $C_{\infty x}/D$ (%) | $C_{Total}/D$ (%) |
| GRM3-**stage2** | 0.17 | 0.83 | 0.17 | 0.83 |
| GCS | 0.22 | 1.45 | 0.11 | 0.76 |

The enlargement of the cross section can generate a different behavior of the rock formation as the extent of fractured zone around excavation is also affected, with a higher extent of the mixed fractured zone (extensional and shear fractures) near the drift wall and a lower density of the shear fractures in the depth (see Appendix A.5). Moreover, the observations show that this multi-stage excavation yields to a more important extent of the fractured zone in the vertical descending direction, as explained by Noiret et al. (2015). However, the support characteristics can have an influence on this fracture extension in the descending direction. As explained above, in the first stage of excavation, the lower part of the drift is unsupported, which induces a higher extension of the initial fracture network in the descending direction. Then, during the enlargement of the cross section, the fracture network has been remobilized. It should be noted that these results have been obtained for a monitoring period of seven months and that a continuous monitoring during a

longer period will be useful for a deeper understanding of the influence of this new methodology of excavation.

### 2.6.3. Preliminary conclusions

The influence of the enlargement of the cross section in the long-term convergence evolution has been analyzed in this section. The enlargement is performed about three months after the end of the first stage of excavation. At this moment, most of the deconfinement is already completed and convergence begins to stabilize with time. It is observed that with the enlargement of the cross section, the convergence evolution of the drift becomes more isotropic. The analysis of the convergence evolution shows that the parameters related to the time-dependent behavior of the ground ($T$ and $m$) decrease in stage 2 as compared to stage 1. This suggests that the enlargement of cross section could limit the delayed response of the ground. Then, the convergence evolution is very well reproduced by fitting a single parameter $C_{\infty x}$. It should be noted that these results have been obtained for a monitoring during about seven months. A permanent monitoring of the closure of the drift is performed in order to better assess the influence of this new methodology of excavation on the long-term convergence.

## 2.7. Influence of the convergence on the support load

As a part of the experimental program performed at the M/HM URL, different types of support have been installed in different experimental drifts. A continuous monitoring is performed by measuring the deformation and the hoop stress in the supports, as detailed in sections 1.4.5 and 1.5.5 (Part I). In this section, in-situ measurements performed in supports of GCR and GCS drifts, which are composed of a flexible support, will be presented and compared with the convergence evolution in drifts. Then, the measurements performed in the segmental lining (rigid support) installed in GRD4 drift will be discussed.

### 2.7.1. Analysis of load support evolution in GCS and GCR drifts

As explained in section 2.1, the support of these two parallel drifts is composed of radial bolts, 21 cm thick layer of fiber shotcrete, yieldable concrete wedges and welded mesh. Moreover, in the last part of the GCR drift, only fiber shotcrete has been installed without the presence of yieldable concrete wedges, which will permit to analyze the influence of the yieldable concrete wedges on the support behavior. Displacement and stress measurements have been performed independently for the layer of fiber shotcrete and for the yieldable concrete wedges.

*2.7.1.1. Monitoring of yieldable concrete wedges*

The yieldable concrete wedges have a compressive strength of about 4 MPa $\pm$ 0.5 and can support a deformation up to 40%. Beyond this level of deformation, the material hardens and the compressive strength increases up to about 30 MPa as schematically shown in Fig. 2.32.
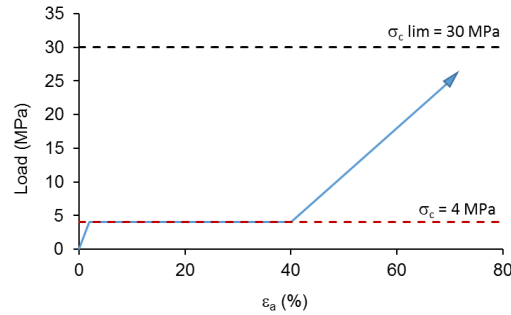


**Fig. 2. 32.** Stress-strain curve for yieldable concrete wedges

Monitoring of yieldable concrete wedges is performed in two different sections installed along drifts. In GCS drift the measurement sections are located at PM 29.5 and PM 47.5, while in GCR drift these ones are located at PM 22.3 and 43.7 (see Table 2.2). As explained in section 1.4.5 (Part I), in each measurement section four different zones have been installed around the drift cross section. Each zone is composed of one potentiometer and one pressure cell. In-situ measurements show that the maximum load supported by the wedges is in the vertical direction of the cross section (points 1 and 3 in Fig. 2.33). Accordingly, the deformation is also maximum in the vertical direction. Moreover, some dispersion is observed between different measurement sections, which could be mainly related to the time of installation of different devices in each section. This could be also related to the local heterogeneities of the rock formation and particularly to the scatter of the fractures' distribution around the drift, which influences the convergence evolution and in turn, the load transmitted to the support. Fig. 2.34 presents the load and the deformation recorded in the yieldable concrete wedges as a function of time in the section located at PM 29.5. The load is increasing rapidly up to about 4 MPa. It is also observed that the anisotropic closure of the drift section accentuates the inhomogeneity of the deformation of yieldable concrete wedges around the drift perimeter.
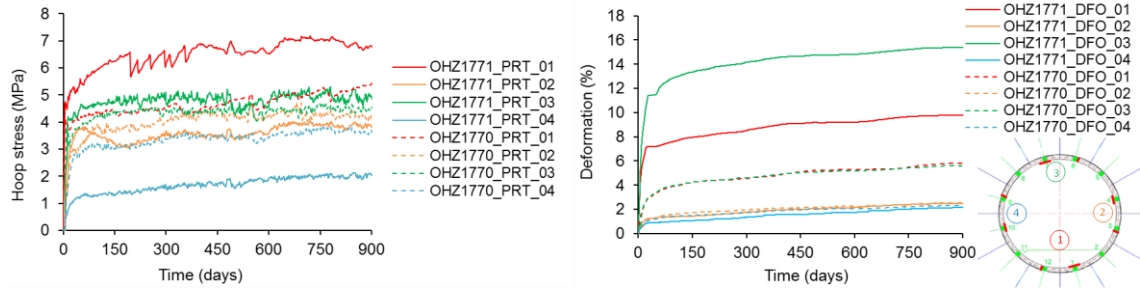
**Fig. 2. 33.** In-situ measurements performed for the yieldable concrete wedges installed in GCS drift. Load (left) and deformations (right) followed by the wedges. Section OHZ1771 (in full line) and OHZ1770 (in dotted line) are located in PM 47.5 and PM 29.5, respectively)
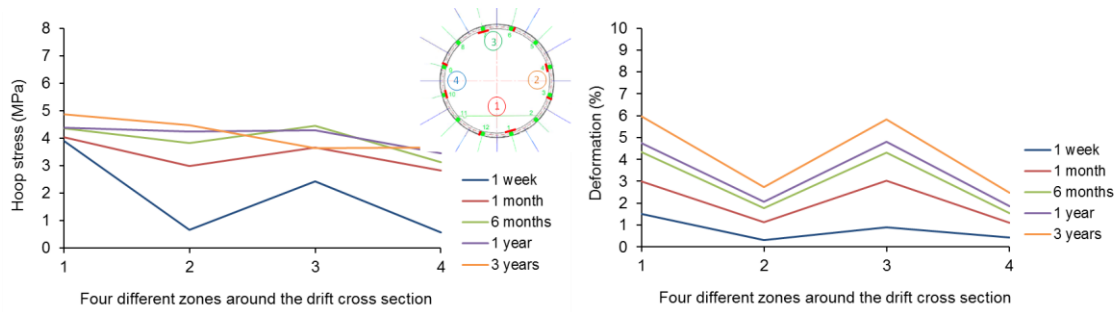


**Fig. 2. 34.** In-situ measurements performed for the yieldable concrete wedges installed in GCS drift section OHZ1770. Load (left) and deformations (right) around of drift as a function of time

### 2.7.1.2. *Monitoring of fiber shotcrete layer*

A flat jack system is used for measuring the load in the shotcrete. In-situ observations show an anisotropic distribution of the support load, which is more pronounced in the part of the GCR drift without yieldable concrete wedges (Fig. 2.35). The maximum hoop stress is measured in the upper part of the drift cross section. This is in accordance with the closure measurements of the drift which are maximum in the horizontal direction. Moreover, it is observed that the presence of the yieldable concrete wedges leads to a lower and more distributed load of the shotcrete. Thus the yieldable wedges tend to reduce the effect of the anisotropic closure, as it is expected. The monitoring of the shotcrete by a vibrating wire strain gauge shows a similar trend as for the load profile: at the intrados section, the deformation is larger in the upper part of the drift section, and the inhomogeneity of the deformation is more marked in the section of GCR drift without yieldable concrete wedges (see Appendix A.6).
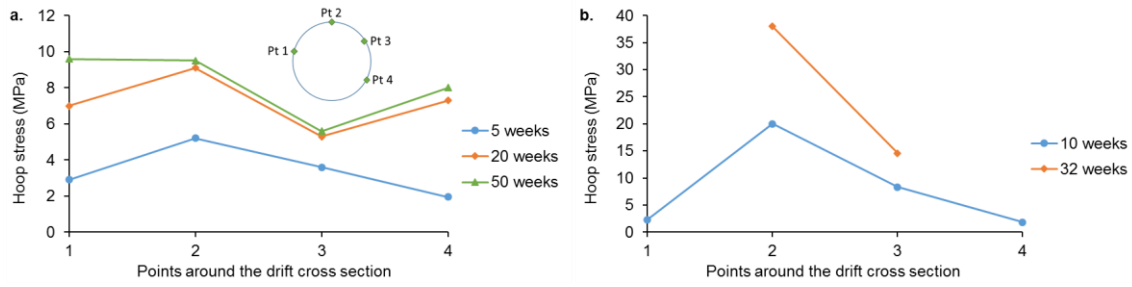
**Fig. 2. 35.** Flat jack system measurements: a. In GCS drift; b. In GCR drift, zone without yieldable concrete wedges

### 2.7.2. *Analysis of load support evolution in GRD4 drift*

Fig. 2.36 presents the hoop strain and stress distributions around the drift cross section for a measurement section of GRD4 installed in the zone with classic mortar. The support has been monitored since its installation until now (i.e. for about three years). It is observed that here again, at the intrados, the hoop stress is maximal in the upper part which reflects the larger closure of the drift section in the horizontal direction. Accordingly the highest compression strain in the support is observed in the upper part. The response at the extrados also reflects an anisotropic loading applied to the support. The measured stresses and strains are compatible with those at the intrados as they are, as expected, of opposite sign. Note that only compressive stress is measured because the total pressure cells cannot measure tensile stresses. Finally, some dispersion has been observed in the measurements of deformation and load of the support around the drift cross section. This can be related to the heterogeneity of the interface contact between the mortar and the rock.

It is observed that load acting on the support increases rapidly during the first weeks. Then, after about three months, its rate significantly decreases. These observations are in accordance with the ones performed for parallel drifts with flexible support. Indeed, as explained above, a high convergence rate is observed during the first hundred days and then it tends to stabilize with time.
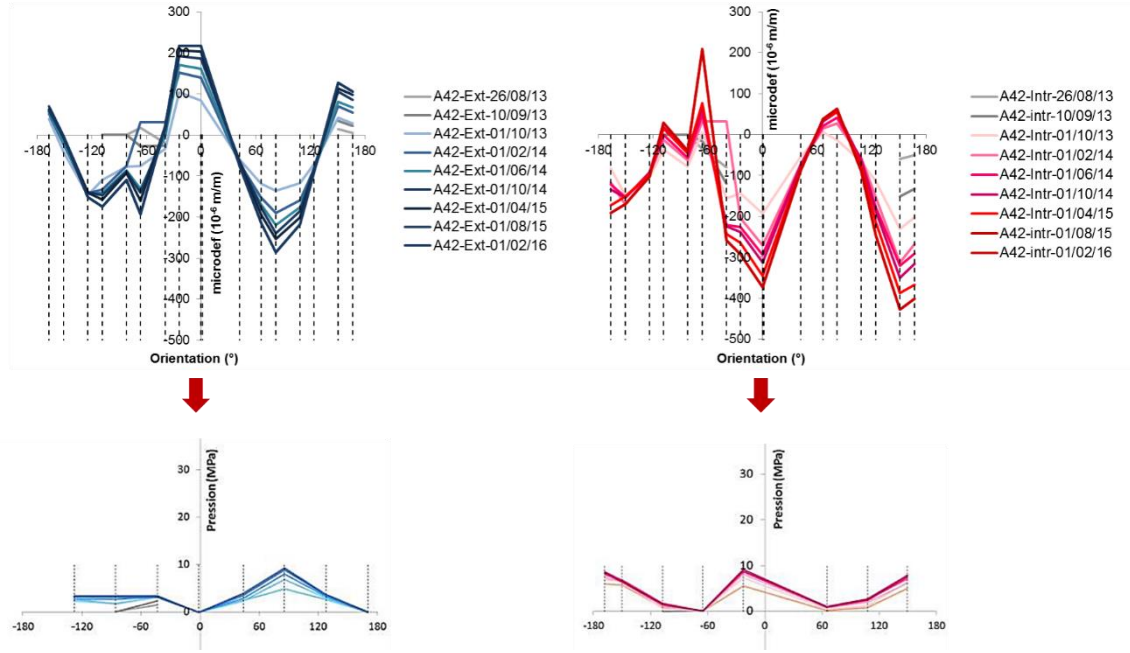
**Fig. 2. 36.** Hoop strain (up) and stress (down) measured at GRD4 drift in the zone with classic mortar. Measurements have been performed at the extrados (left) and intrados (rigth) of the support. The ceiling is considered as the initial angle 0° and the floor as 180°. The traction strain is considered as positive. And, also positive values are given for compression load

### *Discussion*

In this section, we have presented the response of three types of support installed in different drifts in the URL. In an attempt to examine the support influence on the convergence evolution and also the support response in time, an analysis is performed on the basis of the convergence rate evolution. Then, the hoop stress evolution at the support intrados is analyzed by comparing the horizontal convergence predictions, obtained by the approach proposed in this dissertation, and the in-situ hoop stress measurements at the upper part of the drift. Remind that, for the drifts studied in this section, the highest convergence is observed in the horizontal direction of the cross section. As a response of the high horizontal closure, the highest hoop stress is observed in the upper part of the drift cross section.

Fig. 2.37 shows the convergence rate evolution for GCS, GCR and GRD4 drifts (before and after the support installation). We can observe that in all cases the convergence rate decreases with time. An important difference in the convergence rate is observed between the cases in which the rock is not supported (i.e. GRD4 drift during the first 20 days) and the drifts which are supported after each step of excavation (i.e. GCS and GCR drift). As expected, it is observed that the convergence rate is higher in the unsupported opening (i.e. GRD4). When the entire support is completed and functional (about 20 days after the opening of the drift cross section), the

convergence rate is the lowest in GRD4 drift. This variation in the convergence rate clearly shows the influence of the support system on the convergence evolution in time. With the installation of the rigid support in GRD4 drift, the convergence rate becomes very low and continues to decrease in time: at about 900 days after the opening of the section, a convergence rate of about $5 \times 10^{-11}$ s$^{-1}$ is obtained for GCS and of about $5 \times 10^{-13}$ s$^{-1}$ for GRD4. As it is observed in Fig. 2.37, the highest convergence rate is observed in GCS drift (soft support) and the lowest one in GRD4 drift (rigid support).
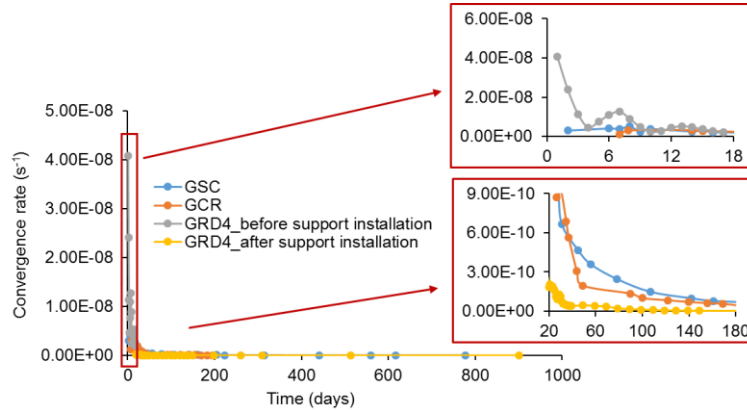


**Fig. 2. 37.** Convergence rate evolution in time. Comparison performed based in the convergence predictions obtained by using the semi-empirical law (eq. 2.6 and eq. 2.8)

Considering the convergence predictions obtained and in an attempt to predict the maximum hoop stress in each support, a simple analysis is performed taking into account a linear behavior of the support. Table 2.17 presents the hoop stress measured in the upper part of the drift cross section and the horizontal convergence obtained at the same dates. It should be noted that it concerns the convergence measured after the installation of the support. Note that the highest convergence is observed in GCS, and the lowest in GRD4, whereas the highest hoop stress at the support intrados is measured in GCR. Fig. 2.38 presents the hoop stress, at the intrados, measured in the upper part at different dates for the three studied drifts. The high hoop stress observed in GCR drift clearly reflects the effect of the absence of yieldable concrete wedges and the installation of the support very close to the drift face.

**Table 2. 17.** Horizontal convergence and hoop stress measurements in the upper part of the drift cross section

| Time (days) | GCS drift (shotcrete with yielding elements) | | GCR drift (shotcrete without yielding elements) | | GRD4 drift (rigid support) | |
|---|---|---|---|---|---|---|
| | Convergence (mm) | Hoop stress (MPa) | Convergence (mm) | Hoop stress (MPa) | Convergence with support (mm) | Hoop stress (MPa) |
| 35 | 31.94 | 5.2 | | | 1.57 | 4 |
| 70 | | | 26.69 | 20 | | |
| 140 | 45.34 | 9.1 | | | 2.00 | 7.5 |
| 224 | | | 32.54 | 38 | | |
| 350 | 50.83 | 9.5 | | | 2.15 | 8.5 |
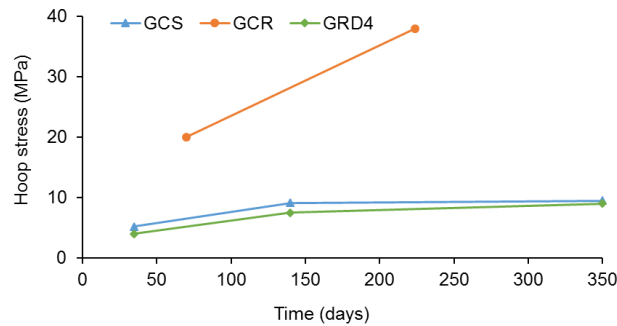


**Fig. 2. 38.** Hoop stress at the upper part of the drift cross section

Considering GCS and GRD4 drifts, which show lower stress level, an extrapolation of the hoop stress in the long term can be obtained from the convergence predictions. For that, the ratio of the convergence at a given date with respect to the total convergence predicted after 100 years is calculated. Then, assuming a linear behavior of the support, an estimation of the hoop stress evolution at a given date can be obtained. Table 2.18 summarizes the predictions up to 30 years. It should be noted that in GRD4 drift, the ratio between the convergences at different dates and the total convergence predicted for 100 years is very close to 1. In fact, when the support is installed, the convergence is blocked as it has been observed in the in-situ measurements.

For these two drifts (GCS and GRD4), the predictions seem to indicate acceptable values for the long-term stress in both cases. However, letting the rock mass unsupported for a short period after the excavation might lead to an extension of the fracture zone as it is observed for GRD4 (see appendix A.5). Thus, it is observed that the type of supports and the conditions of its installation (date and distance to the face) are of major importance for the long-term response.

**Table 2. 18.** Hoop stress measurements (35 to 350 days) and predictions (up to 350 days) at the upper part of the drift (considering a linear behavior of the support)

| Time (days) | GCS drift | | GRD4 drift | |
|---|---|---|---|---|
| | $C_{(x,t)} / C_{(100\ years)}$ | Hoop stress (MPa) | $C_{(x,t)} / C_{(100\ years)}$ | Hoop stress (MPa) |
| 35 | 0.52 | 5.2 | 0.9943 | 4.0 |
| 140 | 0.72 | 9.1 | 0.9980 | 7.5 |
| 350 (1 year) | 0.80 | 9.5 | 0.9992 | 8.5 |
| 730 (2 years) | 0.85 | 10.7 | 0.9996 | 8.9 |
| 1825 (5 years) | 0.90 | 11.5 | 0.9998 | 9.1 |
| 3650 (10 years) | 0.93 | 12.0 | 0.9999 | 9.2 |
| 10950 (30 years) | 0.97 | 12.6 | 0.9999 | 9.3 |

### 2.7.3. *Preliminary conclusions*

The monitoring of the support response of drifts following the direction of $\sigma_H$ has shown a higher hoop stress and hoop strain in the vertical axis of the drift cross section, at the support intrados (mainly in the upper part of the section), which is compatible with the higher convergence in the horizontal direction of the cross section. An extrapolation of the hoop stress in the long term has been proposed on the basis of the convergence evolution law. The key role of the installation conditions of the support has been demonstrated as well as the importance of a yielding support system (as for example with the presence of the yielding blocks) in order to control the long-term stresses.

This approach shows that the monitoring and analysis of the convergence evolution can provide reliable information for the design of support structures. The present analysis was based on a simple linear response of the support and should be extended to a more realistic behavior taking into account the non-linear and time-dependent behavior of the concrete. More information is also needed on the behavior of the yieldable concrete wedges and the limit strain that they can support. Another important point to take into account is the influence of the radial bolts, especially on the extension of the fracture zone around drifts, which in turn will influence the stress transmitted to the supports.

## 2.8. Conclusions

The convergence measurements of different drifts (various sizes and type of supports) with axis following the two drifts' directions, corresponding to the minor and the major in-situ horizontal stresses, have been analyzed. In-situ measurements show an anisotropic closure of walls, with a higher convergence evolution in the horizontal direction and a lower one in the vertical, for drifts excavated along the major horizontal stress ($\sigma_H$). Whereas, for drifts excavated along the minor horizontal stress ($\sigma_h$), a higher convergence evolution in the vertical direction and a lower one in the horizontal are observed. The convergence evolution is analyzed based on the convergence law proposed by Sulem et al. (1987). The parameters of the semi-empirical law are evaluated for different sections in each drift. The results show that drifts which are excavated and supported similarly present close values for the parameters related to the time-dependent behavior (*T*: related to the time-dependent properties of the system rock – support, *m*: related to the ratio between the time-dependent convergence and the instantaneous convergence), which can be assumed as constant values along each drift and for all the parallel drifts. Furthermore, the parameter *X* (related to the distance of influence of the face and the extent of the decompressed zone around the drift) can be considered around 0.9 times the diameter of each drift. Thus, the obtained values suggest that the time-dependent closure of drifts is size independent. It should be noted that, according with the obtained results of the analysis in a drift following the direction of $\sigma_h$ (i.e. GED drift), a higher value of parameter *T* is observed for the vertical closure evolution. This reflects the fact that the convergence recorded in the vertical direction of this drift is not only stronger than the ones of drifts following the direction of $\sigma_H$ (e.g. GCS and GCR drifts), but also exhibits the highest convergence rate (of about $1\times10^{-10}$ s$^{-1}$ even after three years).

Moreover, it is observed that the set of values for convergence law parameters depends on the time elapsed for the support installation and also on the change of excavation rate, which play a key role in the time-dependent convergence evolution of the ground. Finally, a very good reproduction of convergences can be performed by fitting a single parameter $C_{\infty x}$ (instantaneous convergence). This parameter takes into account the anisotropy of the convergence and the dispersion in the deformation evolution along the different drifts.

The influence of the enlargement of the cross section, on the long-term convergence evolution is also analyzed. The enlargement is performed about three months after the end of the first stage of excavation. At this moment, most of the deconfinement is already completed and convergence begins to stabilize with time. It is observed that with the enlargement of the cross section, the convergence evolution of the drift becomes more isotropic. The analysis of the convergence

evolution shows that the parameters related to the time-dependent behavior of the ground (*T* and *m*) decrease in stage 2 as compared to stage 1. This suggests that the enlargement of cross section could limit the delayed response of the ground. Then, the convergence evolution is very well reproduced by fitting a single parameter $C_{\infty x}$. It should be noted that these results have been obtained for a monitoring during about seven months. A permanent monitoring of the closure of the drift is performed in order to better assess the influence of this new methodology of excavation on the long-term convergence.

Finally, it has been shown that the analysis of the convergence evolution can give valuable insights for the design of support structures. The long-term predictions of the drift closure permit the extrapolation of the stresses in the lining. The proposed analysis was based on a simple linear interaction between the rock mass and the support and could be extended in the future by taking into account the non-linear and time-dependent response of the concrete. The long-term interaction between the effect of the support and the extension of the fracture zone is also an open question.

# PART III: PORE PRESSURE EVOLUTION INDUCED BY DRIFTS EXCAVATION

Interpretation of the observed pore pressure variations around underground excavations is a challenging task, especially in the formations like claystones with a very low permeability ($<10^{-19}$ m$^2$). Recent studies have been carried out on the analysis of the pore-pressure evolutions induced by excavation: analysis of measurements around undergrounds excavations in claystones (Armand et al. 2011 and 2014; Corkum and Martin 2007; Marschall et al. 2008; Noiret et al. 2011), coupled modeling of the excavation damaged zone based on strain localization analysis (Pardoen et al. 2015a and 2015b; Salehnia et al. 2015), coupled modeling of the thermal impact on the hydro-mechanical behavior of the rock mass (Bian et al. 2012), and unsaturated hydro-mechanical modeling of the excavation (Charlier at al. 2013).

In the M/HM URL, continuous monitoring around drifts during and after the excavation showed an anisotropic pore pressure field around the drifts with zones of marked overpressure. For drifts parallel to the horizontal major principal stress, even though the initial stress state in the drift section is quasi-isotropic, the pore pressure evolution and the mechanical response are anisotropic. These observations suggest that the intrinsic anisotropy of the material plays a key role in the response of rock formation. In this part, a poroelastic analysis of the pore pressure change induced by drift excavation is performed. The main goal is to simulate the main trends of the pore pressure evolution with a simple model taking into account the inherent anisotropy of the material. Moreover, a failure analysis is performed in an attempt to understand the role of the hydro-mechanical coupling in the extension of the failed zone around the drifts.

## 3.1. In-situ pore pressure measurements

Boreholes devoted to the pore pressure measurements have been installed before the beginning of drift excavation as a part of mine-by-tests. As explained in section 1.4 (Part I), the mine-by experiment is performed to characterize the excavation-induced deformation and the hydro-mechanical response of the rock formation during and after excavation. Therefore, all the performed measurements (deformation, pore pressure, permeability and damage evolution as a function of time) are followed over years to study the long-term response of the rock formation.

The measurements show an anisotropic pore pressure distribution around the drifts, which depends on the drifts orientations. For drifts following the direction of $\sigma_H$, lateral overpressures

(i.e. in the horizontal direction) have been measured before the front passage. The pore pressure drops down at the vicinity of the drift wall when the drift's face passes by the monitored section. The in-situ observations do not show a significant overpressure in the vertical direction. Drifts following the direction of $\sigma_h$ show also lateral overpressure in far field. However, the monitoring of the pore pressure field around drifts in this direction is more recent and more data will be available in a near future. The amplitudes of the overpressure and of the pressure drop depend on the distance to the wall and to the face (along the axis of the drift).

In both directions of excavation, the distance of influence of the tunnel face on the pore pressure field is about 20 m ($\approx$ 4 diameters), which is twice the distance of influence observed for the monitored displacements. It should be noted that similar observations have been made for excavations performed in Boom clay and Opalinus clay formations (e.g. Vaunat et al. 2013; Giger et al. 2015).

Fig. 3.1 and 3.2 present the recorded data in horizontal and vertical directions of a drift excavated following $\sigma_H$ (GCS drift). It is observed that, in the horizontal direction of the cross section, an overpressure is induced by the excavation advance (Fig. 3.1). Chamber (1), is located ahead of the face and has been destroyed when the face reaches PM 35.7. This chamber recorded an overpressure before the passage of the face with a peak observed when the face is at a distance of about 1 diameter. Then this overpressure drops when the face is very close (at about 0.5 diameter), which can be related to the fact that the face hits the borehole, as explained by Armand et al. (2011). Similar records have been obtained from chambers (2) and (3) which are located very close to the drift wall: a peak of overpressure is observed ahead of the face and then the pore pressure drops down when the face reaches the location of each chamber. After the passage of the face, the pore pressure increases inside the rock mass up to a distance from the drift wall of about 4.8 m (chamber (4)), when the face is at a distance of about one diameter ahead. Moreover, at a distance of about 9 m from the drift wall (chamber (5)), a very slow rate of overpressure increase is observed even after the end of the excavation. In the vertical direction (Fig. 3.2), a small overpressure is developed before the passage of tunnel face. Then, after the passage of the face, no overpressure is observed.
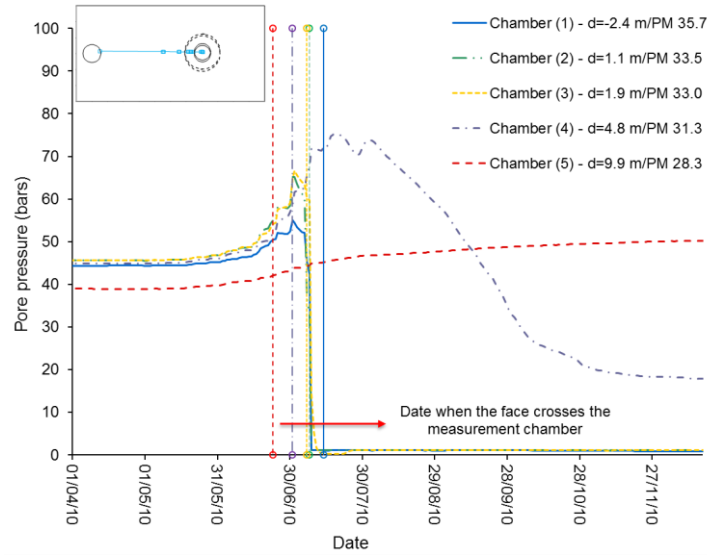
**Fig. 3. 1.** Pore pressure evolution in the horizontal direction of the drift cross section. Measurements recorded during GCS excavation (adapted from Armand et al. 2011). d: distance to the drift wall. PM: metric point from the entrance of the drift
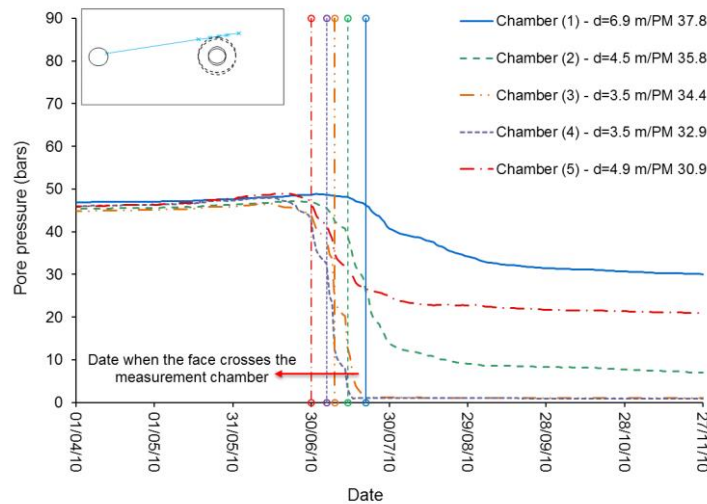


**Fig. 3. 2.** Pore pressure evolution in the vertical direction of the drift cross section. Measurements recorded during GCS excavation (adapted from Armand et al. 2011). d: distance to the drift wall. PM: metric point from the entrance of the drift

## 3.2. Poro-elasticity framework

A fully coupled poroelastic analysis is performed using the finite element method to simulate the pore pressure evolution induced by drift excavation. The main goal of this analysis is to reproduce and understand the main trends of the fractures development with a simple model taking into account the influence of the inherent anisotropy of the material. The fundamental bases of

97

poroelasticity theory have been presented in several textbooks and reference papers (e.g. Coussy 2004; Detournay and Cheng 1993). In this analysis, it is assumed that the porous material is fully saturated and under isothermal conditions.

The equilibrium equation reads:

$$\nabla \cdot \sigma + f = 0 \tag{3.1}$$

where, $\sigma$ is the stress tensor and $f$ is the body force. The poroelastic constitutive equation is given by:

$$\mathrm{d}\sigma_{ij} = C_{ijkl}\mathrm{d}\varepsilon_{kl} - b_{ij}\mathrm{d}p \tag{3.2}$$

where $C_{ijkl}$ is the drained stiffness tensor, $\varepsilon_{kl}$ the strain tensor, $p$ the pore pressure and $b_{ij}$ the Biot effective stress coefficient tensor (Biot 1941; Biot and Willis 1957). For the case of transverse isotropy (Cheng 2016), the drained elastic stiffness tensor $C_{ijkl}$ is given by:

$$C_{ijkl} = \begin{bmatrix} M_{xx} & M_{xy} & M_{xz} & 0 & 0 & 0 \\ M_{xy} & M_{yy} & M_{xy} & 0 & 0 & 0 \\ M_{xz} & M_{xy} & M_{xx} & 0 & 0 & 0 \\ 0 & 0 & 0 & G & 0 & 0 \\ 0 & 0 & 0 & 0 & (M_{xx}-M_{xz})/2 & 0 \\ 0 & 0 & 0 & 0 & 0 & G \end{bmatrix} \tag{3.3}$$

where,

$$M_{xx} = \frac{E_x(E_y - E_x v_{yx}^2)}{(1+v_{xz})(E_y - E_y v_{xz} - 2E_x v_{yx}^2)}$$

$$M_{xz} = \frac{E_x(E_y v_{xz} + E_x v_{yx}^2)}{(1+v_{xz})(E_y - E_y v_{xz} - 2E_x v_{yx}^2)}$$

$$M_{xy} = \frac{E_x E_y v_{yx}}{(E_y - E_y v_{xz} - 2E_x v_{yx}^2)} \tag{3.4}$$

$$M_{yy} = \frac{E_y^2(1 - v_{xz})}{(E_y - E_y v_{xz} - 2E_x v_{yx}^2)}$$

where $E_x$ and $E_y$ are the drained Young's moduli in the plane of isotropy and in the direction perpendicular to it respectively; $v_{xz}$ and $v_{yx}$ are the drained Poisson's ratio for effect of the stresses in the plane of isotropy and in the direction normal to it on the strain in the plane of isotropy, respectively; $G$ is the shear modulus normal to the plane of isotropy.

Biot effective stress coefficient for an isotropic porous material is given by $b = 1 - K_d/K_s$, where $K_d$ is the drained bulk modulus and $K_s$ is the unjacketed bulk modulus. For the case of transverse isotropy, two different Biot effective stress coefficients $b_x$ and $b_y$ in the plane of isotropy and in the direction perpendicular to it respectively have to be considered (Cheng 1997, 2016). They can be expressed in terms of the drained elastic constants of the anisotropic solid and of the unjacketed modulus:

$$b_x = 1 - \frac{M_{xx} + M_{xy} + M_{xz}}{3K_s}$$

$$b_y = 1 - \frac{2M_{xy} + M_{yy}}{3K_s}$$

(3.5)

The variation of the Lagrangian porosity $\phi$ is given by the following relation (Coussy 2004),

$$\mathrm{d}\phi = b_{ij}\mathrm{d}\varepsilon_{ij} + \frac{\mathrm{d}p}{N}$$

(3.6)

where $N$ is Biot's skeleton modulus. For an isotropic porous material the modulus $N$ is given by $1/N = b/K_s - \phi_0/K_\phi$ (Berryman 1992; Ghabezloo 2011), where $K_\phi$ is the unjacketed pore bulk modulus (Berryman 1992; Ghabezloo et al. 2008) and $\phi_0$ the porosity at the reference state. The modulus $K_\phi$ is generally very difficult to evaluate experimentally (Ghabezloo et al. 2008), however, for a porous material made up of a homogeneous solid phase $K_\phi = K_s$ and the expression of the Biot modulus is reduced to the well-known relation $1/N = (b - \phi_0)/K_s$ (Coussy 2004). For the case of transverse isotropy the modulus $N$ is given by (Aichi and Tokunaga 2011 and 2012; Ghabezloo and Hemmati 2011):

$$\frac{1}{N} = 2(1-b_x)\left[\frac{(1-v_{xz})b_x}{E_x} - \frac{v_{yx}b_y}{E_y}\right] + \frac{(1-b_y)}{E_y}(b_y - 2v_{yx}b_x) - \frac{\phi_0}{K_\phi}$$

(3.7)

where, $b_x$ and $b_y$ are the Biot coefficients in the plane of isotropy and in the plane normal to it respectively.

The fluid mass conservation leads to the following relation:

$$\frac{\mathrm{d}m_f}{\mathrm{d}t} + \nabla \cdot q = 0 \tag{3.8}$$

where $m_f = \rho_f \phi$ is the fluid mass per unit volume of the porous material, $q$ is the fluid mass discharge and $\rho_f$ is the fluid density. The fluid mass discharge is given by Darcy's law,

$$q = -\rho_f \frac{k}{\mu} \nabla p \tag{3.9}$$

with $k$ the intrinsic permeability having dimension of length squared and $\mu$ the fluid dynamic viscosity. The variation of fluid mass is defined by,

$$\mathrm{d}m_f = \rho_f \mathrm{d}\phi + \mathrm{d}\rho_f \phi_0 \tag{3.10}$$

The variations of fluid density are given by $\mathrm{d}\rho_f = \rho_f \, \mathrm{d}p / K_f$ where $K_f$ is the bulk modulus of the fluid. Inserting Eq. (3.9) in Eq. (3.8) and Eq. (3.2) in Eq. (3.1), the system of equations to solve is obtained:

$$\begin{cases} \nabla \cdot \left( C_{ijkl} \mathrm{d}\varepsilon_{kl} - b_{ij} \mathrm{d}p \right) = 0 \\ b_{ij} \dfrac{\mathrm{d}\varepsilon_{ij}}{\mathrm{d}t} + \left( \dfrac{1}{N} + \dfrac{\phi_0}{K_f} \right) \dfrac{\mathrm{d}p}{\mathrm{d}t} - \dfrac{1}{\rho_f} \nabla \cdot \left( \rho_f \dfrac{k}{\mu} \nabla p \right) = 0 \end{cases} \tag{3.11}$$

To perform the coupled hydro-mechanical modeling, Eqs. (3.11) are implemented in the finite element code FreeFem++ (Hecht 2012; Hecht et al. 2013). FreeFem++ is a free software (GPL) with a programming language focused on solving partial differential equations using the finite element method in 2D and 3D. FreeFem++ is written in C++ and developed and maintained by Université Pierre et Marie Curie and Laboratoire Jacques-Louis Lions in France.

## 3.3. Influence of the cross-anisotropy of rock formation on the short-term ground response

As explained above, in-situ measurements show that for drifts following the direction of $\sigma_H$, even if the initial stress state is quasi-isotropic in the plane of the drift section, the pore pressure evolution and the mechanical response are anisotropic. These observations indicate that the intrinsic anisotropy of the material plays a key role in the response of the rock formation. The influence of the inherent anisotropy of the rock on the pore pressure field evolution around the drift is analyzed by a numerical simulation performed under plane strain conditions. The size of the finite element model is 100 m × 100 m considering a radius (*r*) of the drift of 2.6 m. Fig. 3.3 shows the model geometry, the finite element mesh, and the initial and boundary conditions. It should be mentioned that analytical solutions have been developed for tunnels excavated in saturated poroelastic isotropic rock (e.g. Wang 2000; Bobet 2010) and for elastic transversely isotropic rock (Bobet 2011) taking into account a static or quasi-static load. These analytical solutions have been developed for steady state conditions. The present numerical analysis allows to study the pore pressure evolution in time. A validation of the code is presented in Appendix B.1.
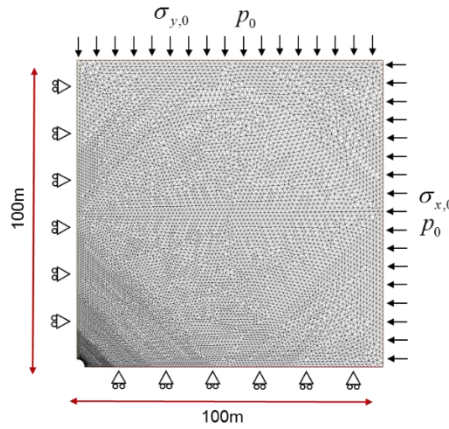


**Fig. 3. 3.** Initial conditions for two-dimensional numerical model ( $\sigma_{x,0}$ and $\sigma_{y,0}$ are the initial stress state in horizontal and vertical directions of the drift cross section; and $p_0$ is the initial pore pressure)

For the purpose of clarity, the analysis has been performed taking into account different features that can influence the pore pressure evolution around the drifts. First, for the instantaneous response (at $t = 1$ second) induced by an instantaneous excavation imposing a zero pore pressure at the drift wall, a parametric study is performed in order to highlight the influence of the anisotropy of hydro-mechanical properties of the rock mass formation, and to propose a set of optimal parameters to reproduce the main trends of the pore pressure evolution observed in-situ.

Once the set of parameters is fixed, the evolution in time of the pore pressure is analyzed for the two directions of excavation.

### 3.3.1. Anisotropy of the hydro-mechanical properties of the rock mass formation

For the analysis of an instantaneous excavation with zero pore pressure imposed at the drift wall, various simulations with different settings have been performed in order to analyze the pore pressure change due to the excavation, taking into account the anisotropy of the initial stress state, the anisotropy in the permeability of the rock formation and finally the anisotropy of the mechanical parameters. To this aim, four cases are studied:

- Case 1: isotropic mechanical properties, permeability and initial stress state
- Case 2: isotropic mechanical properties and permeability, anisotropic initial stress state
- Case 3: isotropic mechanical properties, anisotropic permeability and anisotropic initial stress state
- Case 4: anisotropic mechanical properties, permeability and initial stress state

Table 3.1 summarizes the set of drained elastic mechanical and hydraulic parameters used in each case. The Biot effective stress coefficient is taken as an isotropic parameter, then a detailed analysis of its influence on the pore pressure response is presented in section 3.3.1.2. Fig. 3.4 presents the pore pressure response to the instantaneous excavation for the different studied cases. Concerning the boundary conditions, the initial stress state ($\sigma_{x,0}$ and $\sigma_{y,0}$) and the initial pore pressure ($p_0$) are imposed at the external boundaries, the normal displacements and the water flux are set to zero on the symmetry axes. A zero pore pressure is imposed on the drift wall, in order to simulate drained boundary condition. The analysis is performed for each direction of excavation.

**Table 3. 1.** Mechanical and hydraulic parameters for the 2D model

| | Direction parallel to: | $\sigma_{x,0}$ (MPa) | $\sigma_{y,0}$ (MPa) | $E_x$ (MPa) | $E_y$ (MPa) | $v_{xz}$ | $v_{yx}$ | $G$ (MPa) | $b$ | $k_x$ (m²) | $k_y$ (m²) | $\phi_0$ |
|---|---|---|---|---|---|---|---|---|---|---|---|---|
| Case 1 | $\sigma_H$ / $\sigma_h$ | 12.4 | | 4000 | | 0.3 | | 1540 | 0.6 | 2.7×10⁻²⁰ | | 0.18 |
| Case 2 | $\sigma_H$ / $\sigma_h$ | 12.4 / 16.1 | 12.7 | 4000 | | 0.3 | | 1540 | 0.6 | 2.7×10⁻²⁰ | | 0.18 |
| Case 3 | $\sigma_H$ / $\sigma_h$ | 12.4 / 16.1 | 12.7 | 4000 | | 0.3 | | 1540 | 0.6 | 4×10⁻²⁰ | 1.33×10⁻²⁰ | 0.18 |
| Case 4 | $\sigma_H$ / $\sigma_h$ | 12.4 / 16.1 | 12.7 | 5200 | 4000 | 0.2 | 0.3 | 1700 | 0.6 | 4×10⁻²⁰ | 1.33×10⁻²⁰ | 0.18 |

One can see that for the drifts following the direction of $\sigma_H$, the results obtained for cases 1, 2 and 3 are very close (Fig. 3.4a). Indeed, the initial stress state is quasi-isotropic and the difference with respect to the fully isotropic case (case 1) is not significant. Moreover, it is observed that considering the very low permeability, the slight anisotropy of the permeability (case 3) does not have a significant influence on the instantaneous rock response. On the other hand, the anisotropy of the elastic moduli (case 4) significantly influences the value of the maximum pore pressure. In this case, an overpressure of 22% is observed in the horizontal direction of the cross section, while in the vertical direction no overpressure is observed.

For drifts following the direction of $\sigma_h$, the anisotropy of the initial stress state is the main cause of the overpressures observed in the vertical direction (case 2). As explained above, the anisotropy of the permeability does not have a significant influence, thus the results obtained in cases 2 and 3 are very close (Fig. 3.4b). However, taking into account the anisotropy of the elastic stiffness (case 4), it is obtained that the peak of overpressure is lower than in cases 2 and 3. This observation shows that the anisotropy of the elastic properties plays a key role on the pore pressure evolution for both directions of excavation.
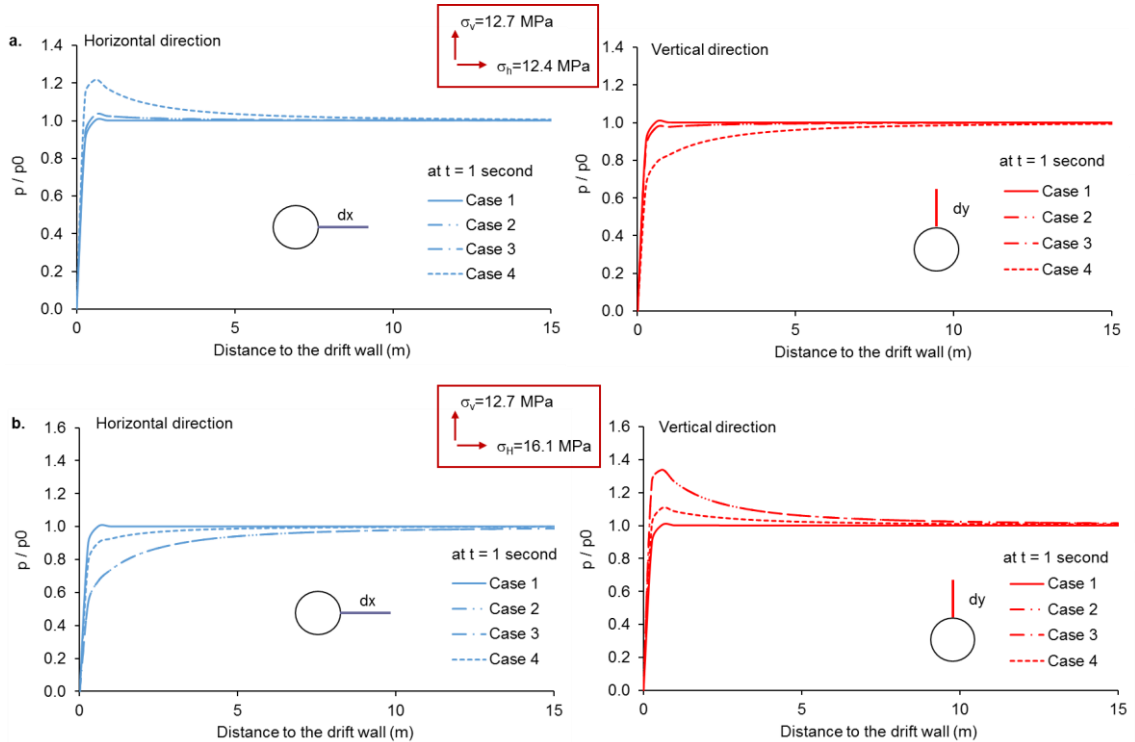


**Fig. 3. 4.** Instantaneous pore pressure change induced by an instantaneous excavation in drained conditions: a. Case of a drift following the direction of $\sigma_H$. b. Case of a drift following the direction of $\sigma_h$. Left side: horizontal pore pressure evolution, Right side: vertical pore pressure evolution

### *3.3.1.1. Influence of the anisotropy of the elastic moduli*

Armand et al. (2013) have shown that the Young's modulus anisotropy ratio $(E_\parallel / E_\perp = E_x / E_y)$ for the Callovo-Oxfordian claystone varies between 1.2 to 2.0. In an attempt to highlight the influence of the degree of elastic anisotropy on the pore pressure evolution around drifts, various numerical computations with an anisotropy ratio ranging between 1.2 and 2.0 have been performed. The results presented in Fig. 3.5 show that by considering a higher anisotropy of the elastic stiffness, the overpressure induced by the excavation is better reproduced for drifts following the direction of $\sigma_H$. However, for drifts following the direction of $\sigma_h$, the overpressure is lower. Indeed, when the anisotropy ratio is about 1.4, a quasi-isotropic response is observed around the drift, with negligible overpressure. For ratios higher than 1.4, an overpressure develops in the horizontal direction whereas the pore pressure is reduced in the vertical direction. Thus, the influence of the anisotropy of the initial stress state (at least for the stress anisotropy ratio of the considered site) is rather limited whereas the influence of the elastic stiffness anisotropy prevails.
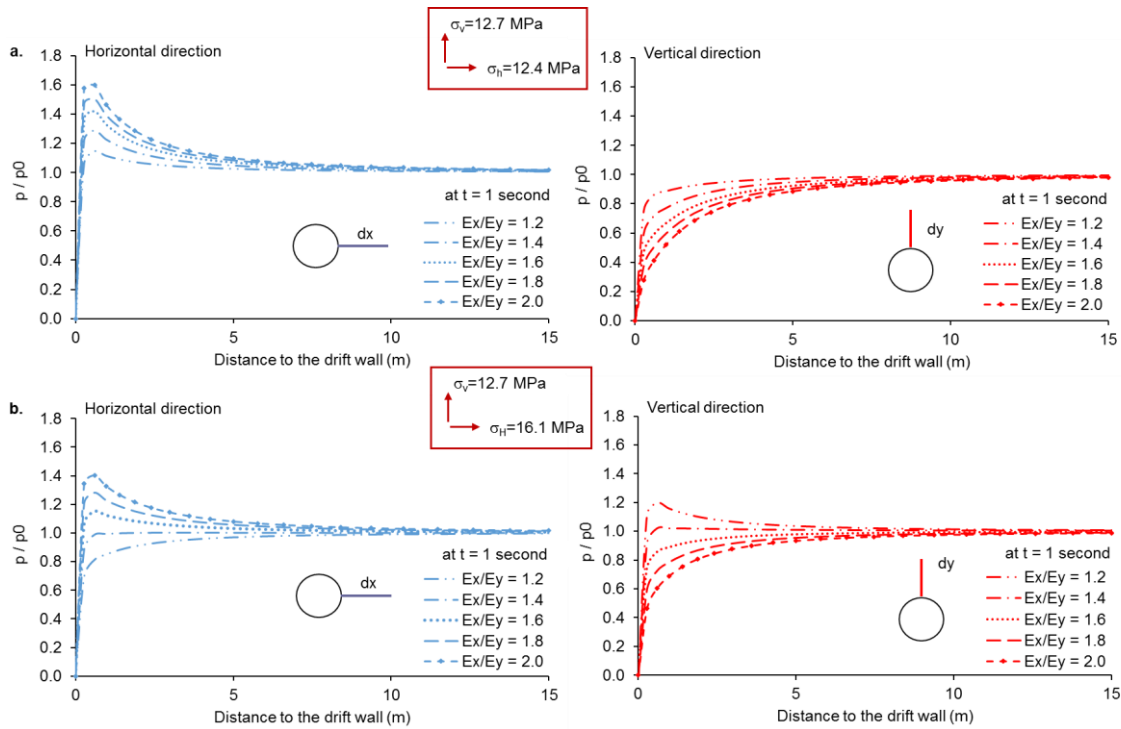


**Fig. 3. 5.** Instantaneous pore pressure response, for various ratios of the Young's modulus in *x* and *y* direction $(E_x / E_y)$ : a. Case of a drift following the direction of $\sigma_H$ . b. Case of a drift following the direction of $\sigma_h$ . Left side: horizontal pore pressure evolution, Right side: vertical pore pressure evolution

Monitoring of the pore pressure field around drifts following the direction of $\sigma_h$ has started recently. Therefore, little information is available at this moment and it is difficult to compare the

above observations with in-situ data. In an attempt to represent the main trends of the pore pressure evolution (following the two directions of excavation), as well as the influence of the overpressures on the failure zone around the drifts, three different ratios $(E_x / E_y)$ are considered. These different ratios are selected in order to reproduce the three possible scenarios of the pore pressure response for drifts following the orientation of $\sigma_h$: (1) overpressure in the vertical direction of the drift cross section $(E_x / E_y = 1.2)$; (2) overpressure in the horizontal direction of the drift cross section $(E_x / E_y = 1.6)$; and (3) quasi-isotropic response of the pore pressure field with a negligible overpressure developed around the drift $(E_x / E_y = 1.4)$. For drifts following the orientation of $\sigma_H$, an overpressure is always obtained in the horizontal direction (as recorded in-situ). A higher value of this anisotropy ratio value will induce a higher overpressure in the horizontal direction. A detailed analysis of the failure initiation around drifts, corresponding to different ratios of anisotropy will be presented in section 3.5.

### 3.3.1.2. *Influence of Biot's effective stress coefficient*

As explained in section 1.1 (Part I), in the literature one can find a rather large range of values (between 0.3 to 1) for the Biot's coefficient of Callovo-Oxfordian claystone. The average value of the Biot's coefficient, commonly used for the Callovo-Oxfordian Claystone, is about 0.6. For an isotropic porous material, with the elastic characteristics of Case 1, this corresponds to an unjacketed bulk modulus of $K_s = 8.5$ GPa. However, in a more recent laboratory work performed by Belmokhtar et al. (2016) on saturated samples, the authors obtained a value of the Biot's coefficient of about 0.85 and an unjacketed bulk modulus $K_s = 21.7$ GPa. Considering the mentioned uncertainty of Biot's coefficient, it is interesting to explore its influence on the pore pressure evolution around the drifts. To this aim, a simulation using the value $b = 0.85$ is performed and compared with another one performed with $b = 0.6$. The comparison is performed considering the cases 4 and 5 (presented in Table 3.1 and 3.2, respectively). Note that the value of $N$ has been updated accordingly for each case. It is observed that the pore pressure evolution in the two cases are very similar, with a slightly higher overpressure developed for the higher value of the Biot's coefficient (Fig. 3.6a and 3.6b).
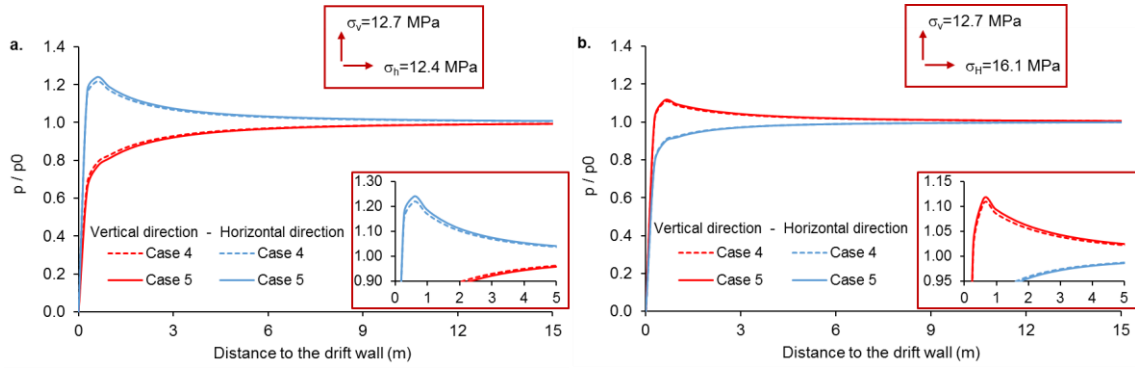
**Fig. 3. 6.** Instantaneous pore pressure response (at t = 1 second), depending on the Biot's coefficient: a. Case of a drift following the direction of $\sigma_H$ . b. Case of a drift following the direction of $\sigma_h$

In the following we analyze the influence of the anisotropy of the Biot's coefficient on the pore pressure response by considering different values in *x*- in *y*- directions. This corresponds to Case 6 $(E_x / E_y = 1.6)$, Case 7 $(E_x / E_y = 1.4)$ and Case 8 $(E_x / E_y = 1.2)$ (Table 3.2). When the Young's modulus anisotropy ratio is low (Case 8), the value of the Biot's coefficient is practically unchanged and therefore the pore pressure profile is very similar to that of case 5 (isotropic value of Biot's coefficient). However, a higher value of this anisotropy ratio (Cases 6 and 7) leads to more significant differences: a higher overpressure is observed in the horizontal direction of the cross section and a lower one in the vertical direction, for both directions of excavation (Fig. 3.7).
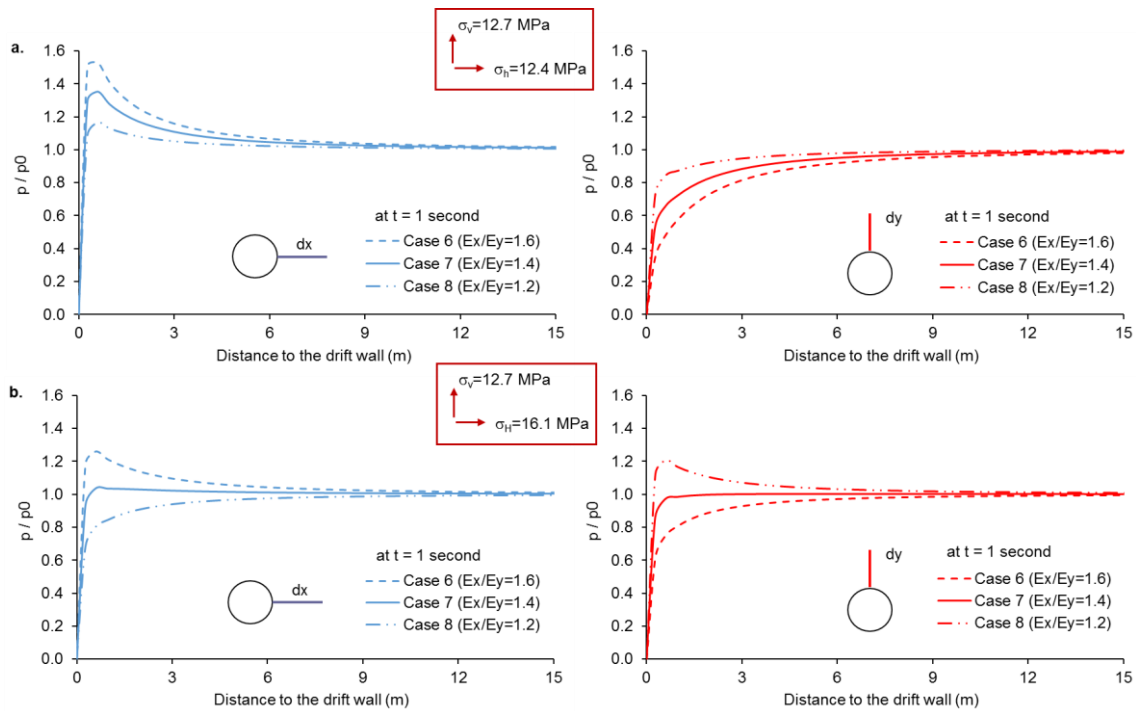


**Fig. 3. 7.** Instantaneous pore pressure response for the three cases studied: a. Case of a drift following the direction of $\sigma_H$ . b. Case of a drift following the direction of $\sigma_h$ . Left side: horizontal pore pressure evolution, Right side: vertical pore pressure evolution

**Table 3. 2.** Mechanical and hydraulic parameters, considering the anisotropy of the Biot's coefficient

| | Direction parallel to: | $\sigma_{x,0}$ (MPa) | $\sigma_{y,0}$ (MPa) | $E_x$ (MPa) | $E_y$ (MPa) | $\nu_{xz}$ | $\nu_{yx}$ | $G$ (MPa) | $b_x$ | $b_y$ | $k_x$ (m²) | $k_y$ (m²) | $\phi_0$ |
|---|---|---|---|---|---|---|---|---|---|---|---|---|---|
| Case 5 | $\sigma_H$ | 12.4 | 12.7 | 5200 | 4000 | 0.2 | 0.3 | 1700 | 0.85 | 0.85 | $4\times10^{-20}$ | $1.33\times10^{-20}$ | 0.18 |
| | $\sigma_h$ | 16.1 | | | | | | | | | | | |
| | $\sigma_h$ | 16.1 | | | | | | | | | | | |
| Case 6 | $\sigma_H$ | 12.4 | 12.7 | 6400 | 4000 | 0.2 | 0.3 | 1800 | 0.75 | 0.79 | $4\times10^{-20}$ | $1.33\times10^{-20}$ | 0.18 |
| | $\sigma_h$ | 16.1 | | | | | | | | | | | |
| Case 7 | $\sigma_H$ | 12.4 | 12.7 | 5600 | 4000 | 0.2 | 0.3 | 1750 | 0.80 | 0.82 | $4\times10^{-20}$ | $1.33\times10^{-20}$ | 0.18 |
| | $\sigma_h$ | 16.1 | | | | | | | | | | | |
| Case 8 | $\sigma_H$ | 12.4 | 12.7 | 4800 | 4000 | 0.2 | 0.3 | 1650 | 0.84 | 0.84 | $4\times10^{-20}$ | $1.33\times10^{-20}$ | 0.18 |
| | $\sigma_h$ | 16.1 | | | | | | | | | | | |

## 3.4. Time evolution of the pore pressure distribution around drifts

For the sake of simplicity, the analysis of the time evolution of the pore pressure distribution is performed taking into account only one set of parameters, presented in case 7. The pore pressure at different times, in vertical and horizontal directions around the drift and for the two directions of excavation are presented in Fig. 3.8. It is observed that, for drifts following the direction of $\sigma_H$, the instantaneous response (after 1s) presents an overpressure close to the wall in the horizontal direction. While, for drifts following the direction of $\sigma_h$, a more isotropic response is obtained with a negligible overpressure in the horizontal direction. This overpressure remains almost constant during the first hours. The quasi-undrained response during the first hours is linked to the very low permeability of the material. To confirm this point some computations have been performed by imposing a zero-flux boundary condition at the drift wall. The numerical results are presented in Fig. 3.9 and compared with the previous results obtained by imposing a zero pore pressure at the drift wall. Indeed, one can see that the instantaneous responses are very similar. As explained above, the instantaneous pore pressure difference between horizontal and vertical directions of the cross section is due to the elastic stiffness anisotropy and also to the orientation of excavation (i.e. the initial stress state). Then this overpressure decreases with time at a very slow rate due to the very low permeability of the rock mass.
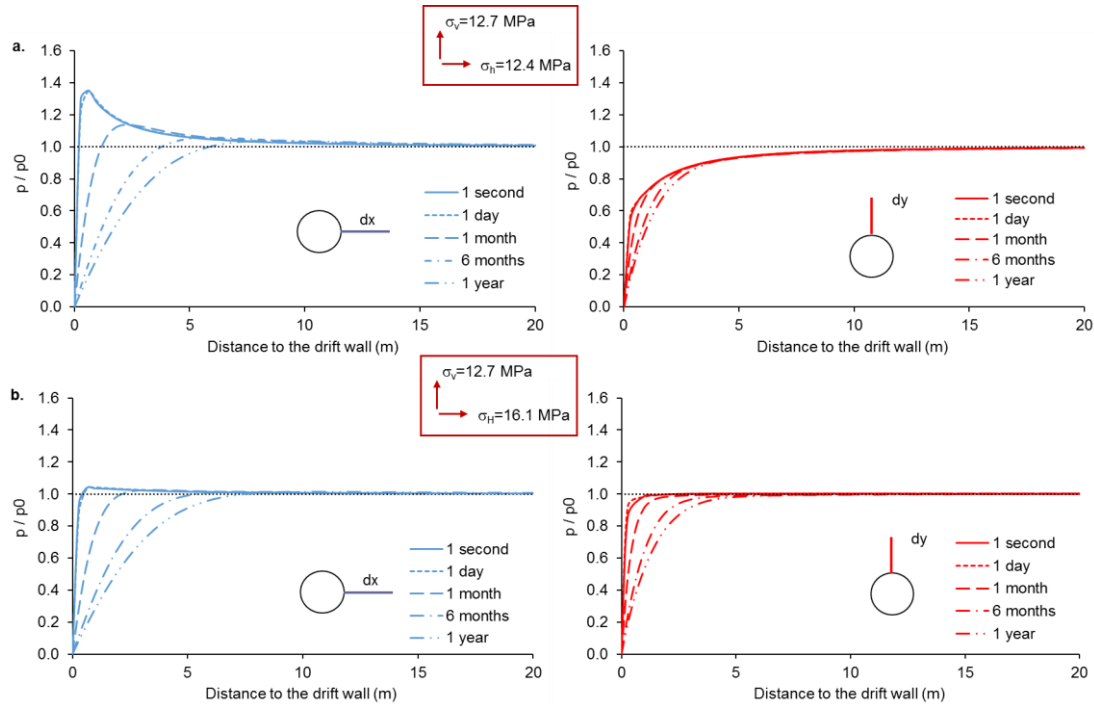


**Fig. 3. 8.** Pore pressure evolution in time: a. Case of a drift following the direction of $\sigma_H$. b. Case of a drift following the direction of $\sigma_h$. Left side: horizontal pore pressure evolution, Right side: vertical pore pressure evolution
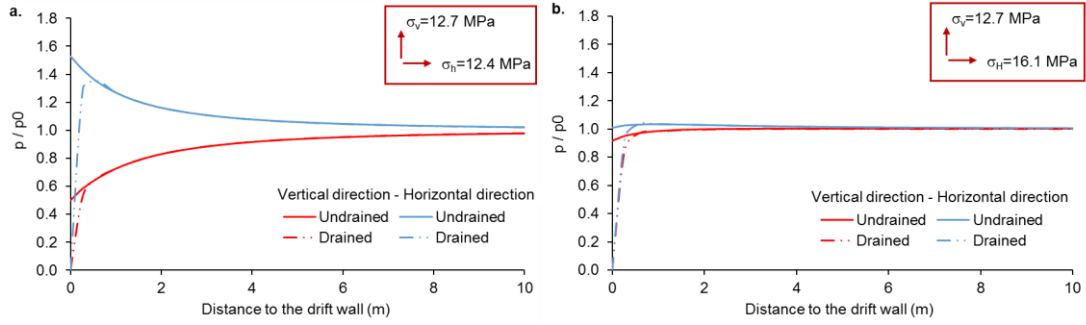
**Fig. 3. 9.** Comparison of instantaneous pore pressure response to instantaneous excavation, in undrained and drained boundary conditions (at t = 1 second): a. Case of a drift following the direction of $\sigma_H$ . b. case of a drift following the direction of $\sigma_h$

The above numerical results are qualitatively in accordance with the in-situ observations for drifts following the direction of $\sigma_H$. Indeed, the overpressures are mainly generated in the horizontal direction of the cross section and can be observed during several months after the excavation at some meters from the drift wall, as shown in Fig. 3.8. However, it should be noted that the overpressures measured in-situ can reach values as high as $1.6 \times p_0$, whereas in the numerical simulations, we obtain $1.35 \times p_0$ for case 7, $1.53 \times p_0$ for case 6 and $1.16 \times p_0$ for case 8. Moreover, the maximum overpressure measured in-situ is situated at about 1 to 1.5 diameters from the wall (e.g. Fig. 11 in Armand et al. 2015b, see Appendix B.2), whereas it is obtained much closer to the wall in the numerical results. Another significant difference is that in-situ measurements show substantial overpressures rather far inside the rock mass (see Fig. 7 in Armand et al. 2015b, see Appendix B.2). The simple poroelastic model used here cannot reproduce these observations. The effect of non-linear and time-dependent behavior of the rock mass as well as the effect of the anisotropic fracture network around the excavation might significantly influence the evolution of the pore pressure field.

### 3.5. Failure initiation analysis around the drifts

In an attempt to highlight the influence of the hydro-mechanical couplings in the initiation of the fractures around drifts, an analysis of the failure conditions is performed based on the Terzaghi effective stress distribution ($\sigma'_{ij} = \sigma_{ij} + p$) around the excavations (for cases 6, 7 and 8, presented in Table 3.2).

The principal stresses around the excavation ($\sigma'_1$ and $\sigma'_3$) are calculated in the case of an instantaneous excavation in undrained boundary conditions, by imposing a zero-flow boundary condition at the drifts wall. This analysis allows to estimate the zones where a tensile effective

radial stress can be actually found around the drift. As the in-situ observations show the presence of a mixed fracture network (extensional and shear fractures), for the short term response, failure is approached by using an interpolation between the Fairhurst's generalized Griffith fracture criterion and the Mohr-Coulomb shear failure criterion. The Fairhurst's generalized Griffith fracture criterion (Fairhurst 1964), which is a generalization of the Griffith criterion (Griffith 1921 and 1924), allows to analyze the tensile failure based on the ratio of compressive to tensile strength $n = \sigma_c / |\sigma_t|$ (Hoek and Martin 2014). For $n \geq 3$ the failure criterion is presented in Eq. 3.12 (a detailed derivation is given in Appendix B.3):

$$\sigma_1' = \frac{(2\sigma_3' + A|\sigma_t|) + \sqrt{(2\sigma_3' + A|\sigma_t|)^2 - 4(\sigma_3'^2 - A|\sigma_t|\sigma_3' + 2AB\sigma_t^2)}}{2}$$

with,

$$A = 2(w-1)^2$$

$$B = [(w-1)/2]^2 - 1 \tag{3.12}$$
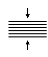
$$w = \sqrt{\sigma_c / |\sigma_t| + 1}$$

The Mohr-Coulomb failure criterion describes the shear failure initiation, presented in Eq. 3.13:
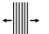
$$\sigma_1' = \frac{1 + \sin\phi}{1 - \sin\phi}\sigma_3' + \frac{2C\cos\phi}{1 - \sin\phi} \tag{3.13}$$

where, $C$ is the cohesion and $\phi$ the friction angle of the rock mass formation. The Mohr-Coulomb failure criterion parameters for the studied rock are presented in Table 3.3. Combination of the Fairhurst and the Mohr-Coulomb failure criteria permits to distinguish between zones around the excavation which exhibit extension failure and those which exhibit shear failure. It should be noted that the tensile strength and the cohesion are considered to be anisotropic and vary with the angle between the normal to bedding planes and the direction of loading (Table 3.3 and 3.4). Fig. 3.10 and 3.11 present the failure criteria for the three studied cases, as well as the principal stresses in the three orientations analyzed for drifts following the direction of $\sigma_H$ and $\sigma_h$, respectively.

**Table 3. 3.** Mohr-Coulomb failure criterion parameters (Andra database)

| | *0°* | *90°* | *45°* |
|---|---|---|---|
| $C$ (MPa) | 6.6 | 5.9 | 5.6 |
| $\phi$ | | 23° | |

**Table 3. 4.** Tensile strength values (Andra database)

| | 0° | 90° | 45° |
|---|---|---|---|
| |  |  |  |
| $\sigma_t$ (MPa) | -1.5 | -1.2 | -1.3 |



**Fig. 3. 10.** Major and minor principal effective stress ( $\sigma'_1$ and $\sigma'_3$ ) in the horizontal, vertical and diagonal directions of the drift cross section for a drift following the orientation of $\sigma_H$ : a. Case 8. b. Case 7. c. Case 6. The Fairhurst's failure criterion is represented with continuous lines and the Mohr-Coulomb failure criterion is represented with dashed lines. Continuity of the slope between the two failure criterion is imposed
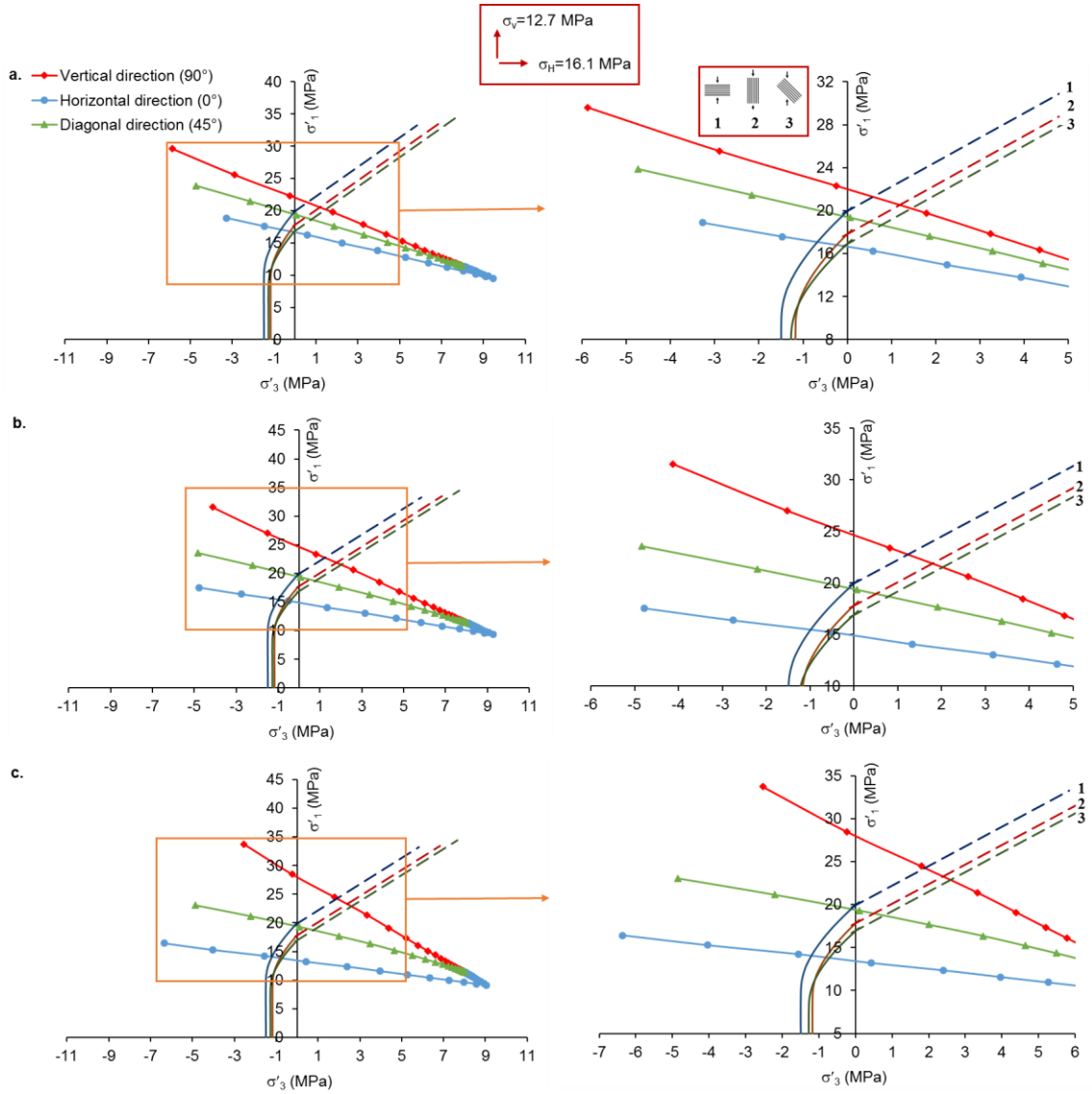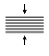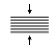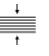
**Fig. 3. 11.** Major and minor principal effective stress ( $\sigma_1'$ and $\sigma_3'$ ) in the horizontal, vertical and diagonal directions of the drift cross section for a drift following the orientation of $\sigma_h$ : a. Case 8. b. Case 7. c. Case 6. The Fairhurst's failure criterion is represented with continuous lines and the Mohr-Coulomb failure criterion is represented with dashed lines. Continuity of the slope between the two failure criteria is imposed

It is observed that for the two orientations of drifts excavation and for all the studied cases, tensile failure occurs in the horizontal direction of the drift cross section (0°). On the other hand, in the diagonal and vertical directions (45° and 90°) the failure mode depends on the degree of elastic anisotropy and on the orientation of drifts. Indeed, for the drifts following the orientation of $\sigma_H$ in the diagonal direction (45°), tensile failure is first reached in the three cases studied, while in the vertical direction (90°) tensile failure is obtained for case 8 $(E_x/E_y = 1.2)$ and shear failure is obtained for case 7 $(E_x/E_y = 1.4)$ and for case 6 $(E_x/E_y = 1.6)$. On the contrary, for the drifts following the orientation of $\sigma_h$, it is observed that in the diagonal (45°) and vertical direction

112

(90°) shear failure is first reached. Table 3.5 summarizes the extension of the zones where tensile and shear failure criteria are reached. For comparing with the in-situ observations (summarized in Table 1.3 in Part I), the extension of these zones is normalized with the diameter of excavation.

**Table 3. 5.** Extension of failure zone around drifts

| $E_x / E_y$ ratio | | | 1.2 (Case 8) | | | 1.4 (Case 7) | | | 1.6 (Case 6) | | |
|---|---|---|---|---|---|---|---|---|---|---|---|
| *Zone extension (normalized with diameter) of :* | | *0°* | *90°* | *45°* | *0°* | *90°* | *45°* | *0°* | *90°* | *45°* |
| $\sigma_H$ | Tensile failure | 0.12×D | 0.10×D | 0.12×D | 0.14×D | - | 0.12×D | 0.16×D | - | 0.11×D |
| | Shear failure | - | - | - | - | 0.08×D | - | - | 0.07×D | - |
| $\sigma_h$ | Tensile failure | 0.07×D | - | - | 0.09×D | - | - | 0.11×D | - | - |
| | Shear failure | - | 0.17×D | 0.14×D | - | 0.16×D | 0.14×D | - | 0.15×D | 0.13×D |

It should be noted that the extension of the failure zone around drifts also depends on the degree of elastic anisotropy and on the orientation of drifts (Fig. 3.12). It is observed that for drifts following the orientation of $\sigma_H$ the highest extension of the failure zone is obtained in the horizontal direction and the lowest in the vertical direction, as observed in-situ. The anisotropy of the failure zone is more pronounced for a higher degree of elastic anisotropy. On the contrary, for drifts following the orientation of $\sigma_h$ the highest extension of the failure zone is observed in the vertical direction and the lowest one in the horizontal direction, as observed in-situ. With the increase of the degree of elastic anisotropy, the extension of the failure zone around the drift becomes more isotropic. We however emphasize that only the onset of failure is analyzed here without considering its progressive propagation (see Pardoen et al. 2015a and 2015b).

The observed discrepancy on the extension of fracture network around drifts, between the results of the numerical simulation and the in-situ observations, can be attributed to the simplicity of the performed analysis, which is based on a linear poroelasticity. However, it is observed that the shape of the failure zones around the drift is qualitatively reproduced. Furthermore, the performed analysis clearly shows that the hydro-mechanical couplings play a key role in the rock mass response.

It should be noted that the presence of the fracture network can explain the anisotropic convergences observed in drifts, which correspondingly present a higher closure in the horizontal and vertical directions of the cross section respectively for drifts following the direction of $\sigma_H$ and $\sigma_h$, as explained in the above Part of the dissertation (Section 2.3). This is in accordance with results obtained by Salehnia et al. (2015), who explain that the pore pressure evolution in the

vicinity of drift is consistent with the mechanical anisotropic convergence and the shearing pattern.
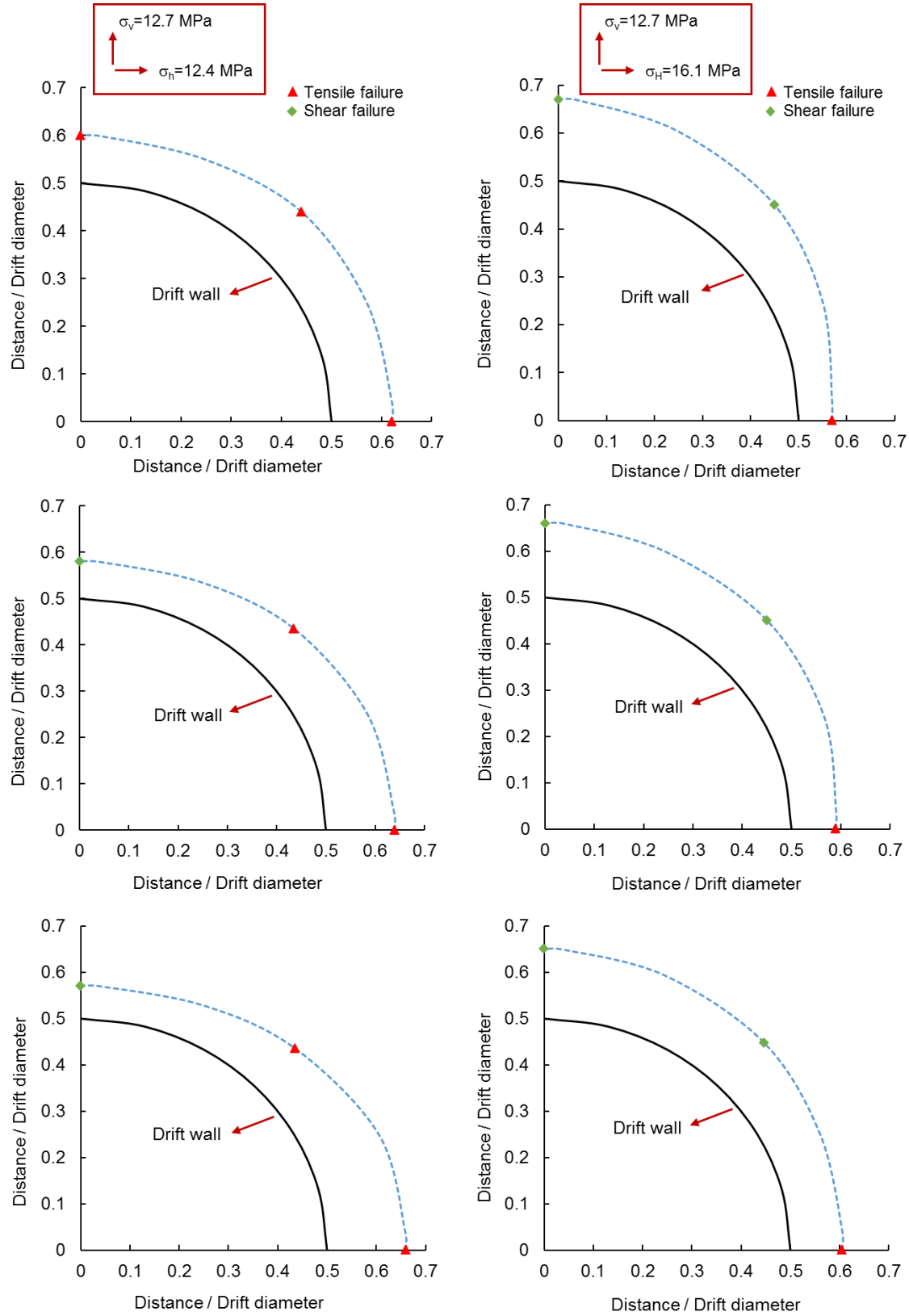


**Fig. 3. 12.** Extension of the failure zone around the drifts. a. Case 8. b. Case 7. c. Case 6. Left side: case of a drift following the orientation of $\sigma_H$ , Right side: case of a drift following the direction of $\sigma_h$

## 3.6. Conclusions

The influence of the anisotropy of the rock mass formation on the pore pressure evolution induced by tunnel excavation has been analyzed by means of a fully coupled poroelastic model. It is shown that the main trends of the pore pressure evolution can be simulated and analyzed based on an efficient and simple poroelastic model under plane strain conditions. Taking into account the inherent anisotropy of the material, it is observed that the anisotropy of the pore pressure response around the drifts can be directly related to the anisotropy of the elastic stiffness and also to the anisotropy of the in-situ stress state. For the particular case of Meuse/Haute-Marne Underground Research Laboratory, it is found that the anisotropy of the Biot effective stress coefficient has little influence on the pore pressure response. Moreover, it is observed that because of the very low permeability of the material, overpressure develops around drifts and persists during several months. It is interesting to note that lateral overpressure (i.e. in the horizontal direction of the drift cross section) is measured both for drifts excavated in the direction of the major or minor horizontal stress. This can be reproduced in the proposed poroelastic analysis by considering an anisotropy ratio of the Young's modulus ($E_h/E_v$) greater than about 1.4.

It is also obtained that a significant pore overpressure can induce tensile effective radial stresses. Based on a failure analysis, it is found that the hydro-mechanical coupling can play a key role in the development of the failed zone around the drifts. Moreover, it is observed that the failure zone also depends on the degree of mechanical anisotropy (stiffness and resistance) and on the anisotropy of the in-situ stress state. The in-situ extension of the failed zone is only qualitatively reproduced, due to the simplified assumptions of the constitutive model. However, its shape and the different failure modes can be well reproduced for both directions of excavation (following $\sigma_H$ or $\sigma_h$). It is worth to emphasize that this analysis based on a poroelastic behavior of the rock mass only provides information on the onset of failure. More advanced analysis is necessary to accurately reproduce the fracture networks. Two different approaches can be developed based on fractures mechanics for modeling crack initiation and propagation (e.g. Hauseux et al. 2016 for crack initiation) or on strain localization analysis accounting for the non-linear behavior of porous material (e.g. Pardoen et al. 2015a and 2015b). The onset and propagation of fractures and/or dilatant localized shear zones will significantly affect the local pore pressure field.

# CONCLUSIONS

A continuous monitoring of the hydro-mechanical response of the rock mass formation, around different experimental drifts excavated at the Meuse/Haute-Marne Underground Research Laboratory (M/HM URL), has been performed from the excavation until now (i.e. during several months or years depending on the drift). One of the main goals is to explore the hydro-mechanical behavior of the Callovo-Oxfordian claystone and to understand its response to the excavation works. In-situ observations show an anisotropic response of the rock formation to the excavation progress which is mainly evidenced in: the anisotropic extension of the fracture network around drifts induced by the excavation progress; the anisotropic time-dependent closure of drifts; the anisotropic pore pressure field and the marked overpressures developed around excavation openings.

Different drifts have been excavated following two main orientations, corresponding to the major and the minor in-situ horizontal stresses ( $\sigma_H$ and $\sigma_h$ ). Stress measurements have shown that the vertical stress is very close to the minor horizontal stress and that the ratio between the major horizontal stress with the minor one is about 1.3. The in-situ measurements show an anisotropic closure of walls, with a higher convergence evolution in the horizontal direction for drifts excavated along $\sigma_H$ . Whereas, for drifts excavated along $\sigma_h$ , a higher convergence evolution in the vertical direction is observed. Therefore, it has been observed that the principal axes of deformations follow the horizontal and vertical directions in the plane of the drift cross section. Moreover, these principal deformation axes are in accordance with the fractures distribution around drifts. These observations suggest that, in addition to the effect of the initial stress state, the rock anisotropy plays a key role in the ground response to excavation.

In this work, the question of the anisotropic closure of drifts has been studied by means of a direct analysis of the in-situ measurements using the semi-empirical law proposed by Sulem et al. (1987). By considering an elliptical deformation of the drift cross section, the parameters of this semi-empirical law are evaluated in the principal directions of deformation, for different sections in each studied drift. As the excavation has been performed with different characteristics (e.g. methods, rate and size excavation, support systems…), the anisotropy and the variability of the closure have been analyzed taking into account the influence of the excavation characteristics.

The main results show that:

All the studied drifts excavated in the direction of $\sigma_H$, which are excavated and supported similarly, present close values for the parameters related to the time-dependent behavior (*T*: related to the time-dependent properties of the system (rock mass formation – support), *m*: related to the ratio between the time-dependent convergence and the instantaneous convergence, *n*: exponent which describes the form of the fitted curve), which can be assumed as constant values along each drift and for all the parallel drifts. Furthermore, the parameter *X* (related to the distance of influence of the face and the extent of the decompressed zone around the drift) can be considered as 0.9 times the diameter of each drift. Thus, the obtained values suggest that the time-dependent convergence of drifts is size independent.

Comparing between drifts excavated in the direction of $\sigma_H$ and drifts excavated in the direction of $\sigma_h$, which are excavated and supported similarly, it is observed that constant values for the parameters *X*, *m* and *n* can be assumed. Parameter *T* is constant along a drift and takes two different values. One value is obtained for the closure along the vertical and horizontal directions for drifts following $\sigma_H$ orientation (e.g. GCS drift) and along the horizontal direction for drifts following $\sigma_h$ orientation (e.g. GED drift). The other value is obtained in the vertical direction of GED. This reflects the fact that the convergence recorded in the vertical direction of GED is not only stronger than the ones of GCS and GCR, but also exhibits the highest convergence rate (of about $1 \times 10^{-10} s^{-1}$ even after three years). The origin of this observation is not clearly understood, but it can be attributed to various factors such as (i) the different fracture patterns (extent and direction) of the different drifts, (ii) the difference in the density of the excavation induced fractures, (iii) the influence of the drift geometry. The geometry of GED which is not perfectly circular generates stress concentration in the floor that induces a slight floor heave.

It is shown that by monitoring convergence for about 40 days, the model can be applied for reliable predictions of the long-term convergence evolution.

The time elapsed for the support installation and also the change of excavation rate play a key role in the time-dependent convergence evolution of the ground. It is observed that the set of values for convergence law parameters are highly dependent on these changes. Note that in all cases, the four parameters of the convergence law are fixed (*T*, *X*, *m* and *n*) along each drift and a very good reproduction of convergence curve can be performed by fitting a single parameter $C_{\infty x}$ (i.e. the instantaneous convergence). This parameter takes into account the anisotropy of the convergence and the heterogeneity of the deformation along the different drifts.

The influence of the enlargement of the cross section could be studied for one drift excavated in the direction of the major principal stress. It was observed that, after the enlargement of the section, the convergence evolution of the drift is less anisotropic, and stabilizes faster in time. The enlargement was performed about three months after the end of the first stage of excavation. At this moment, most of the deconfinement is already completed and convergence begins to stabilize with time. The analysis of the convergence evolution shows that the parameters related to the time-dependent behavior of the ground ($T$ and $m$) decrease in stage 2 as compared to stage 1. This suggests that the enlargement of the cross section could limit the delayed response of the ground. It should be noted that these results have been obtained during a short period (about seven months). A permanent monitoring of the closure of the drift is performed in order to better assess the influence of this new methodology of excavation on the long-term convergence.

Finally, the comparison of the results obtained from the analysis of the convergence measurements with the data obtained from the extensometer measurements shows that the convergence law permits to distinguish the instantaneous convergence induced by the excavation progress and the long-term convergence due to the rheological behavior of rock formation. This distinction is well reproduced by the model and a very good prediction of the convergence, and therefore of the radial displacements, is obtained.

*This complete treatment of the recorded data allows for reliable predictions of the convergence evolution in the long term. The monitoring and analysis of the convergence data provide reliable information of the interaction between rock mass and support, which is a key issue for the design of support structures for future CIGEO project facilities.*

Furthermore, the continuous monitoring of the rock formation show an anisotropic pore pressure field around the drifts, with lateral overpressure (i.e. in the horizontal direction of the drift cross section) observed for both drifts excavated in the direction of the major or minor horizontal stress. In an attempt to understand the influence of the hydromechanical coupling in the anisotropic response evidenced in the rock mass formation, a fully coupled poroelastic finite element simulation has been performed, taking into account the inherent anisotropy of the material. It is shown that:

The anisotropy of the pore pressure response around the drifts can be related to the anisotropy of the elastic stiffness and also to the anisotropy of the in-situ stress state. Moreover, it is observed that because of the very low permeability of the material, overpressure develops around drifts and persists during several months. Furthermore, it has been found that by considering an anisotropy ratio of the Young's modulus ($E_h/E_v$) greater than about 1.4, the lateral overpressure observed can

be reproduced in the proposed poroelastic analysis for both directions of excavation. Therefore, it is shown that the main trends of the pore pressure evolution can be simulated and analyzed based on an efficient and simple poroelastic model under plane strain conditions.

It is observed that the hydro-mechanical coupling plays a key role in the development of the failed zone around the drifts. Indeed, a significant pore overpressure can induce tensile effective radial stresses. Therefore, based on a failure analysis, it is obtained that the failure zone also depends on the degree of mechanical anisotropy (stiffness and resistance) and on the anisotropy of the in-situ stress state. Even if the in-situ extension of the failed zone is only qualitatively reproduced, due to the simplified assumptions of the constitutive model, its shape and the different failure modes can be well reproduced for both directions of excavation (following $\sigma_H$ or $\sigma_h$). It is worth to emphasize that this analysis based on a poroelastic behavior of the rock mass only provides information on the onset of failure. More advanced analysis is necessary to accurately reproduce the fractures network. The onset and propagation of fractures and/or dilatant localized shear zones will significantly affect the local pore pressure field.

*Outlooks*

During the development of the studies presented in this dissertation, as the M/HM URL is in continuous development, new questions arose with the new excavations performed (with variations in excavation and constructions methods). Principal outlooks based on this work are presented in following.

### *New and future drifts excavated at the M/HM URL*

For the new excavated drifts, a monitoring for a longer period of time is needed to better understand the influence of the different methods of excavation and system supports implemented. It is the case of GRM3 and GRD4 drifts where, because of the sequence and method of excavation, differences on the rock response are observed, as for example, different extent of fractured network around excavation. A continuous monitoring and also the possibility to compare with future drifts excavated with similar method of excavation and similar support will help to better assess the influence of the new methodologies implemented on the long-term behavior of the drifts.

For future works, especially for drifts excavated by the road header under shield technique (for which, because of the excavation process, the measurement sections have been installed far from the drift face), the monitoring of the rock response by means of mine-by tests performed from neighboring drifts will help to better understand the evolution of the deformation around the excavated drifts. This will be of great importance in the upper part of the drift cross section where a higher extension of the fracture network has been observed.

On the other hand, it is interesting to analyze the role of the radial bolts on the response of the rock as it has been observed that they limit the extension of the fracture network around drifts, mainly in the upper part of the drift cross section.

As the construction of the CIGEO project facilities will be performed in an incremental way, a continuous monitoring of the convergence evolution in time will help to optimize the design of future works. As it has been shown, the monitoring during few weeks permits a very good prediction of the long-term convergence evolution. Note that, as the main part of the convergence happens during the first days, the time delayed for the monitoring sensors installation plays a key role in the lost convergence and also in the dispersion of the data observed between different sections. Reducing this time can reduce this dispersion and better assess the role of the heterogeneity of the rock mass formation.

Finally, a monitoring of the excavation with new techniques as the TBM machine, which will be used for the excavation of the shaft access, should take into account that the convergence evolution will be highly influenced by the rate of excavation which will be higher and by the delayed installation of the support.

### *Improvement on the convergences analysis using the semi-empirical law proposed by Sulem et al. (1987)*

It has been observed that in the case of the M/HM URL the semi-empirical convergence law proposed by Sulem et al. (1987) allows for reliable predictions of the convergence evolution in the long term. Moreover, it has been observed that a set of parameters values can be fixed for drifts excavated and supported similarly. New insights can be obtained by relating the parameters of this law to the ground parameters. In a recent paper, Tran-Manh et al. (2016) have proposed this approach for the case of the Saint-Martin-la-Porte access adit in France within the framework of a constitutive model with time-dependent degradation of the rock mass. Therefore, this

approach can be extended for anisotropic closure and performed as a next step of the present work.

Moreover, the long-term predictions of the drifts closure permit the extrapolation of the stresses in the lining. The analysis presented in this dissertation should be extended taking into account the non-linear and time-dependent response of the concrete, for realistic prediction of the long-term stresses in the support.

<u>*Analysis of the hydro-mechanical response to the excavation works*</u>

Field monitoring during the excavation progress shows pore pressure changes around drifts, with overpressures developed in the horizontal direction of the cross section, as explained above. It is obtained that the overpressure peak observed in the ground depends upon several factors, such as the orientation of the drift regarding major principal stress, the distance to the drift wall and also the distance to the face. Therefore, an analysis of the face advance effect on the pore pressure change around drifts and also in the development of the failed zone around the drifts, should be taken into account. In order to better assess the influence of the three dimensional effects on the rock response to drift excavation, a 3D model is necessary. However, one of the principal advantages of the convergence-confinement method used for 2D models is its simplicity. Further research should be developed on these questions: how the pore pressure change induced by the drift advance, can be taken into account in a simplified 2D model? How the mechanical deconfinement rate can be related to the pore pressure change?

Moreover, as explained above, more advanced analysis is necessary to accurately reproduce the fractures network. Future works should be developed in order to reproduce the onset and the propagation of the different fracture modes around drifts, accounting for the non-linear behavior of the porous material.

# REFERENCES

Aichi M & Tokunaga T (2011). Thermodynamically consistent anisotropic constitutive relations for a poroelastic material saturated by two immiscible fluids, *International Journal of Rock Mechanics and Mining Sciences, 48(4),* pp 580–584

Aichi M & Tokunaga T (2012). Material coefficients of multiphase thermoporoelasticity for anisotropic micro-heterogeneous porous media. *International Journal of Solids and Structures, 49(23-24),* pp 3388–3396

Anagnostou G & Cantieni L (2007). Design and analysis of yielding support in squeezing ground. *Proc. 11th ISRM Congress.* Lisbon, July 2007, 4 p

Andra (2005). Synthesis argile: evaluation of the feasibility of a geological repository in argillaceous formation. http://www.andra.fr/international/download/andra-international-en/document/editions/ 266va.pdf

Andra (2009). Stockage réversible profond - Options de conception du stockage en formation géologique profonde. *Dossier 2009.* C.NSY.ASTE.08.0429.A

Andra (2013a). Everything you ever wanted to know about radioactive waste management. *Edition Andra – Programmes de recherche. Brochure, Sept 2013, ref : 337JVA*, 16 p

Andra (2013b). Bilan des recherches conduites par l'Andra de 2010 à 2012. *Edition Andra – Programmes de recherche. Brochure, Oct 2013, ref : 537*, 87 p

Amadei B (1983). Rock anisotropy and the theory of stress measurements. *Lecture notes in Engineering Series. vol. 2. New York: Springer-Verlag*, 478 p. ISBN-13:978-3-540-12388-0

Amadei B (1996). Importance of anisotropy when estimating and measuring in situ stresses in rock. *International Journal of Rock Mechanics and Mining Sciences & Geomechanics Abstracts, 33(3)*, pp. 293–325. doi:10.1016/0148-9062(95)00062-3

Armand G, Wileveau Y, Morel J, Cruchaudet M & Rebours H (2007). Excavated Damaged Zone (EDZ) in the Meuse Haute-Marne underground research laboratory. In: *Ribeiro e Sousa L Olalla C and Grossmann N (eds.), The Second Half Century of Rock Mechanics. Proc. 11th ISRM Congress. Lisbon, July 2007*, pp 33–36

Armand G, Noiret A, Cruchaudet M & Conil N (2011). Mine by experiment performed in the Callovo-Oxfordian Claystone at the Meuse Haute Marne underground research laboratory (France). In: *Q. Qian & Y. Zhou (eds), Harmonising Rock Engineering and the Environment, Proc. 12th ISRM Congress. Beijing, Oct 2011*, pp 157-162

Armand G, Noiret A, Zghondi J & Seyedi D (2013). Short- and long-term behaviors of drifts in the Callovo-Oxfordian claystone at the Meuse/Haute-Marne Underground Research Laboratory. *Journal of Rock Mechanics and Geotechnical Engineering, 5(3)*, pp 221–230. doi:10.1016/j.jrmge.2013.05.005

Armand G, Leveau F, Nussbaum C, de La Vaissiere R, Noiret A, Jaeggi D, Landrein P & Righini C (2014). Geometry and properties of the excavation induced fractures at the

Meuse/Haute-Marne URL drifts. *Rock Mechanics and Rock Engineering, 47(1)*, pp 21-41. doi:10.1007/s00603-012-0339-6

Armand G, Dewonck S, Bosgiraud JM & Richard-Panot L (2015a). Development and new research program in the Meuse Haute-Marne Underground Research Laboratory (France). *Proc. 13th ISRM Congress. Montréal, Mai 2015*. ISB number 978-1-926872-25-4

Armand G, Noiret A, Morel J & Seyedi D (2015b). Pore pressure change during the excavation of deep tunnels in the Callovo Oxfordian claystone. *Proc. 13th ISRM Congress. Montréal, Mai 2015*. ISB number 978-1-926872-25-4

Armand G, Conil N, Talandier J & Seyedi DM (2016). Fundamental aspects of the hydromechanical behaviour of Callovo-Oxfordian claystone: From experimental studies to model calibration and validation. *Computers and Geotechnics – COx claystone excavations special issue*. doi:10.1016/j.compgeo.2016.06.003

Arnould A, Toussaint A, Baudouy L, Righiniwaz C & Dotessi A (2016). Suivi géologique du creusement des galeries du CMHM : de l'observation à la modélisation 3D / Geological survey of the excavation-induced fracture network at URL drifts: from observation to 3D modelling. *Proc. Journées Nationales de Géotechnique et de Géologie de l'Ingénieur. Nancy, July 2016*

Belmokhtar M, Delage P, Ghabezloo S, Tang AM, Menaceur H & Conil N (2016). Poroelasticity of the Callovo-Oxfordian claystone. *Rock Mechanics and Rock Engineering*. doi:10.1007/s00603-016-1137-3

Bemer E, Longuemare P, Vincké O (2004). Poroelastic parameters of Meuse/Haute Marne argillites: Effect of loading and saturation states. *Applied Clay Science, 26(1)*, pp 359-366

Bernier F, Li XL, Verstricht J, Barnichon JD, Labiouse V, Bastiaens W, Palut JM, Ben Slimane JK, Ghoreychi M, Gaombalet J, Huertas F, Galera JM, Merrien K, Elorza FJ & Davies C (2003). CLIPEX: Clay Instrumentation Programme for the Extension of an Underground Research Laboratory. EUR 20619 EN (2003), Luxembourg: Commission of the European Communities

Berryman J (1992). Effective stress for transport properties of inhomogeneous porous rock. *Journal of Geophysical Research, 97,* pp 17409–17424

Bian HB, Jia Y, Armand G, Duveau G & Shao JF (2012). 3D numerical modelling thermo-hydromechanical behaviour of underground storages in clay rock. *Tunnelling and Underground Space Technology, 30,* pp 93–109. doi:10.1016/j.tust.2012.02.011

Biot MA (1941). General theory for three-dimensional consolidation. *Journal of Applied Physics, 12,* pp 155-164

Biot MA, Willis DG (1957). The elastic coefficients of the theory of consolidation. *Journal of Applied Mechanics, 24,* pp 594-601

Blanco Martín L, Hadj-Hassen F, Tijani M & Armand G (2011a). New numerical modelling of the mechanical long-term behaviour of the GMR gallery in ANDRA's Underground Research Laboratory. *Journal of Physics and Chemistry of the Earth, 36(17-18)*, pp 1872–1877. doi:10.1016/j.pce.2011.07.027

Blanco Martin L, Hadj-hassen F, Tijani M & Noiret A (2011b). A new experimental and analytical study of fully grouted rockbolts. *In: 45th US Rock Mechanics / Geomechanics Symposium, Jun 2011, San Francisco, United States*, pp.ARMA 11-242

Blümling P, Bernier F, Lebon P & Derek Martin C (2007). The excavation damaged zone in clay formations time-dependent behaviour and influence on performance assessment. *Journal of Physics and Chemistry of the Earth, 32(8-14)*, pp 588–599. doi:10.1016/j.pce.2006.04.034

Bobet A (2010). Characteristic Curves for Deep Circular Tunnels in Poroplastic Rock. *Rock Mechanics and Rock Engineering, 43(2)*, pp 185–200. doi:10.1007/s00603-009-0063-z

Bobet A (2011). Lined Circular Tunnels in Elastic Transversely Anisotropic Rock at Depth. *Rock Mechanics and Rock Engineering, 44(2)*, pp 149–167. doi:10.1007/s00603-010-0118-1

Boidy E (2002). Modélisation numérique du comportement différé des cavités souterraines. *PhD Thesis, Université Joseph Fourier – Grenoble I*, France, 315 p

Bonnet-Eymard T, Thiriat F, Piedevache M, Prouvot J, Richard-Panot L, Armand G, Laviguerie R & Martin F (2011). Soutènement souple pour le creusement de galeries dans les argilites du CMHM. *Proc. Int. Congress, AFTES, Underground spaces for tomorrow. Lyon, Oct 2011*, 7 p

Chappell B. A (1989). Rock Bolts and Shear Stiffness in Jointed Rock Masses. *Journal of Geotechnical Engineering, 115(2)*, pp 179–197

Charlier R, Collin F, Pardoen B, Talandier J, Radu JP & Gerard P (2013). An unsaturated hydro-mechanical modelling of two in-situ experiments in Callovo-Oxfordian argillite. *Engineering Geology, 165*, pp 46–63. doi:10.1016/j.enggeo.2013.05.021

Chen L, Shao JF & Huang HW (2010). Coupled elastoplastic damage modeling of anisotropic rocks. *Computers and Geotechnics, 37(1-2)*, pp 187–194. doi:10.1016/j. compgeo. 2009. 09.001

Cheng A H-D (1997). Material coefficients of anisotropic poroelasticity. *International Journal of Rock Mechanics and Mining Sciences, 34(2)*, pp 199–205. doi:10.1016/S0148-9062(96)00055-1

Cheng A H-D (2016). Poroelasticity. *Cham, Switzerland: Theory and Applications of Transport in Porous Media Berlin, Vol. 27*. Springer International Publishing

Chiarelli AS (2000). Étude expérimentale et modélisation du comportement mécanique de l'argilite de l'est. *PhD thesis, Université Lille I*, France, 334 p

Chiarelli, AS, Shao JF & Hoteit N (2003). Modeling of elastoplastic damage behavior of a claystone. *International Journal of Plasticity, 19(1)*, pp 23–45. doi:10.1016/S0749-6419(01)00017-1

Collin F & Pardoen B (2013). Excavation damaged zone modelling in claystone with coupled second gradient model. In: *Q. Yang, J.M. Zhang, H. Zheng, & Y. Yao (Eds.), Constitutive Modeling of Geomaterials Springer Series in Geomechanics and Geoengineering, Springer Berlin Heidelberg*, pp 313–317. doi:10.1007/978-3-642-32814-5_42

Corkum AG & Martin CD (2007). Modelling a mine-by test at the Mont Terri rock laboratory, Switzerland. *International Journal of Rock Mechanics and Mining Sciences, 44(6)*, pp 846–859. doi:10.1016/j.ijrmms.2006.12.003

Cornet FH & Röckel T (2012). Vertical stress profiles and the significance of "stress decoupling." *Tectonophysics, 581*, pp 193–205. doi:10.1016/j.tecto.2012.01.020

Coussy O (2004). Poromechanics. *John Wiley & Sons, Chichester,* 298 p

Delaloye D, Diederichs MS, Walton G & Hutchinson J (2015). Sensitivity testing of the newly developed elliptical fitting method for the measurement of convergence in tunnels and shafts. *Rock Mechanics and Rock Engineering, 48(2),* pp 651-667. doi:10.1007/s00603-014-0566-0

Delay J, Vinsot A, Krieguer JM, Rebours H & Armand G (2007). Making of the underground scientific experimental programe at the Meuse/Haute-Marne underground research laboratory, North Eastern France. *Journal of Physics and Chemistry of the Earth, 32(1-7)*, pp 2–18. doi:10.1016/j.pce.2006.04.033

Delay J, Bossart P, Ling LX, Blechschmidt I, Ohlsson M, Vinsot A, Nussbaum C & Maes N (2014). Three decades of underground research laboratories: what have we learned? *Geological Society, London, Special Publications, 400(August 2016),* pp 7–32. doi:10.1144/SP400.1

Detournay E & Cheng A H-D (1988). Poroelastic Response of a Borehole in a Non-hydrostatic Stress Field. *International Journal of Rock Mechanics and Mining Sciences Abstracts, 25(3),* pp 171–182. doi:10.1016/0148-9062(88)92299-1

Detournay E & Cheng A H-D (1993). Fundamentals of Poroelasticity. Chapter 5 in Comprehensive Rock Engineering: Principles, Practice and Projects. *Vol. II, Analysis and Design Method, ed. C. Fairhurst, Pergamon Press,* pp. 113-171

Escoffier S (2002). Caractérisation expérimentale du comportement hydromécanique des argilites de Meuse Haute-Marne. *PhD Thesis, Institut National Polytechnique de Lorraine,* France, 457 p

Fabre G & Pellet F (2006). Creep and time-dependent damage in argillaceous rocks. *International Journal of Rock Mechanics and Mining Sciences, 43 (6),* pp 950–960. doi:10.1016/j.ijrmms.2006.02.004

Fairhurst C (1964). On the validity of the "Brazilian" test for brittle materials. *International Journal of Rock Mechanics and Mining Sciences Abstracts, 1(4),* pp 535-546

Fierz T, Piedevache M, Delay J, Armand G & Morel J (2007). Specialized Instrumentation for Hydromechanical Measurements in Deep Argillaceous Rock. *Proc. FMGM 2007,* pp 1-12. doi:10.1061/40940(307)33

Gasc-Barbier M, Chanchole S & Bérest P (2004). Creep behaviour of Bure clayey rock. *Applied Clay Science, 26 (1-4),* pp 449–58. doi:10.1016/j.clay.2003.12.030

Gaucher G, Robelin C, Matray J.M, Négrel G, Gros Y, Heitz J.F, Vinsot A, Rebours H, Cassagnabère A & Bouchet A (2004). ANDRA underground research laboratory: interpretation of the mineralogical and geochemical data acquired in the Callovian-

Oxfordian formation by investigative drilling. *Physics and Chemistry of the Earth, 29*, pp 55-77

Gay O, Allagnat D, Morel J & Armand G (2010). HA Cells monitoring at the Underground Research Laboratory (URL) in the CMHM (Andra). *Tunnels et Espace Souterrain, 221*, pp 371–382

Ghabezloo S, Sulem J, Guédon S, Martineau F & Saint-Marc J (2008). Poromechanical behaviour of hardened cement paste under isotropic loading. *Cement and Concrete Research, 38,* pp 1424–1437

Ghabezloo S (2011). Micromechanics analysis of thermal expansion and thermal pressurization of a hardened cement paste. *Cement and Concrete Research, 41,* pp 520–532

Ghabezloo S & Hemmati S (2011). Poroelasticity of a micro-heterogeneous material saturated by two immiscible fluids. *International Journal of Rock Mechanics and Mining Sciences, 48(8),* pp 1376–1379

Giger SB, Marschall P, Lanyon B & Martin CD (2015). Hydromechanical response of Opalinus clay during excavation works – A synopsis from the Mont Terri URL. In: *Schubert & Kluckner (Eds.), Future development of Rock Mechanics, Proc. ISRM regional symposium Eurock 2015 & 64th Geomechanics colloquium. Salzburg, October 2015,* pp 609-614. ISBN 978-3-9503898-1-4

Griffith AA (1921). The phenomena of rupture and flow in solids. *The Philosophical Transactions of the Royal Society London (Series A), 221,* pp 163-198

Griffith AA (1924). Theory of rupture. In: *Proc. 1st international Congress of applied mechanics. Delft, 1924,* pp 55-63

Gunzburger Y & Cornet FH (2007). Rheological characterization of a sedimentary formation from a stress profile inversion. *Geophysical Journal International, 168*, pp 402–418

Haimson BC (1993). The Hydraulic Fracturing Method of Stress Measurement: Theory and Practice. In: *Hudson, J. (Ed.), Comprehensive Rock Engineering, vol. 3. Pergamon Press, Oxford*, pp 395– 412

Hauseux P, Roubin E, Seyedi DM & Colliat JB (2016). FE modelling with strong discontinuities for 3D tensile and shear fractures: Application to underground excavation. *Computer Methods in Applied Mechanics and Engineering, 309*, pp 269–287. doi:10.1016/j.cma.2016.05.014

Hecht F (2012). New development in FreeFem++. *Journal of Numerical Mathematics, 20(3-4),* pp 251–265. doi:10.1515/jnum-2012-0013

Hecht F, Auliac S, Pironneau O, Morice J, Le Hyaric A & Ohtsuka K (2013). FreeFEM++, Third Edition, v3.25, www.freefem.org

Hingant P & Guerpillon Y (1986). La construction du tunnel autoroutier de Chamoise. *Tunnels et Ouvrages Souterrains, 77*, pp 206–221

Hoek E & Martin CD (2014). Fracture initiation and propagation in intact rock – A review. *Journal of Rock Mechanics and Geotechnical Engineering, 6(4),* pp 287–300. doi:10.1016/j.jrmge.2014.06.001

Homand F, Shao J, Giraud A & Auvray C (2006). Pétrofabrique et propriétés mécaniques des argilites. *C. R. Geoscience, 338*, pp 882–891. doi:10.1016/j.crte.2006.03.009

Hoxha D, Giraud A, Homand F & Auvray C (2007a). Saturated and unsaturated behaviour modelling of Meuse-Haute/Marne argillite. *International Journal of Plasticity, 23*, pp 733–766

Hoxha D, Auvray C, Giraud A, Homand F & Su K (2007b). Elastoviscoplastic behavior of Meuse/Haute-Marne argillite: laboratory tests and modelling. In: *Proc. of Clays in natural & engineered barriers for radioactive waste confinement, International meeting, Lille, Sept 2007,* pp 613-614

Hu DW, Zhang F & Shao JF (2014). Experimental study of poromechanical behavior of saturated claystone under triaxial compression. *Acta Geotechnica, 9*, pp 207–214. doi:10.1007/s11440-013-0259-y

Jia Y (2006). Contribution à la modélisation thermo-hydro-mécanique des roches partiellement saturées: application au stockage des déchets radioactifs. *PhD Thesis, Université des Sciences et Technologies de Lille*, France, 144 p

Jia Y, Bian H, Duveau G, Su K & Shao JF (2008). Hydromechanical modelling of shaft excavation in Meuse/Haute-Marne laboratory. *Physics and Chemistry of the Earth, 33*, pp 422–435. doi:10.1016/j.pce.2008.10.030

Kleine A (2007). Modélisation numérique du comportement des ouvrages souterrains par une approche viscoplastique. *PhD Thesis, Institut National Polytechnique de Lorraine*, France, 318 p

Laigle F (2004). Modèle Conceptuel pour le Développement de Lois de Comportement adaptées à la Conception des Ouvrages Souterrains. *PhD Thesis, Centre d'Ingénierie Hydraulique & École Centrale de Lyon,* France

Mánica MA, Gens A, Vaunat J & Ruiz DF (2015). Anisotropic failure criterion for an argillaceous rock: formulation and application to an underground excavation case. In: *E. Oñate, D. R. J. Owen, D. Peric, & M. Chiumenti (Eds.), Computational Plasticity XIII – Fundamentals and Applications. International Center for Numerical Methods in Engineering (CIMNE). Proc. of the XIII International Conference on Computational Plasticity – Fundamentals and Applications, Barcelona, Sept 2015,* pp 654-660

Mánica MA, Gens A, Vaunat J & Ruiz DF (2016). A time-dependent anisotropic model for argillaceous rocks. Application to an underground excavation in Callovo-Oxfordian claystone. *Computers and Geotechnics – COx claystone excavations special issue*. doi:10.1016/j.compgeo.2016.11.004

Marschall P, Distinguin M, Shao H, Bossart P, Enachescu C & Trick T (2006). Creation and Evolution of Damage Zones Around a Microtunnel in a Claystone Formation of the Swiss Jura Mountains. *SPE International Symposium and Exhibition on Formation Damage Control held in Lafayette, Louisiana, 15-17 Feb 2006,* 10 p

Marschall P, Trick T, Lanyon GW, Delay J & Shao H (2008). Hydro-Mechanical Evolution of Damaged Zones around a Microtunnel in a Claystone Formation of the Swiss Jura Mountains. *Conference paper, 42nd US Rock Mechanics Symposium and 2nd US – Canada Rock Mechanics symposium, San Francisco, June 29 – July 2, 2008,* 11 p

Martin CD, Lanyon GW, Blumling P & Mayor JC (2002). The excavation disturbed zone around a test tunnel in the Opalinus Clay. In: *Hammah R, Baden W, Curran J, Telesnicki M (Eds.), NARMS/TAC 2002. Proc. of the 5th North American Rock Mechanics Symposium and 17th Tunnelling Association of Canada Conference. Toronto, July 2002*, pp 1581–1588. ISBN 0772767084, 9780772767080

Menaceur H, Delage P, Tang AM & Conil N (2016). On the Thermo-Hydro-Mechanical Behaviour of a Sheared Callovo-Oxfordian Claystone Sample with Respect to the EDZ Behaviour. *Rock Mechanics and Rock Engineering, 49(5),* pp 1875–1888. doi:10.1007/s00603-015-0897-5

Morel J, Renaud V & Armand G (2010). Feasibility of excavation of disposal cells in 500 meter deep clay formation. In: *I. Vrkljan (Ed.), Rock Engineering in Difficult Ground Conditions – Soft Rocks and Karst. Proc. ISRM regional symposium EUROCK 2009. Dubrovnik, Oct 2009*, pp 561-566. ISBN 9780415804813

Morel J, Bumbieler F, Conil N & Armand G (2013). Feasibility and behavior of a full scale disposal cell in a deep clay layer. In: *Kwaśniewski, M. & Łydżba, D. (eds) Rock Mechanics for Resources, Energy and Environment, CRC Press 2013*, pp 621–626

NEA (2001). Going underground for testing, characterization and demonstration (A Technical position Paper). NEA/RWM (2001)6/rev1

Noiret A, Armand G, Cruchaudet M & Conil N (2011). Mine-by experiments in order to study the hydromechanical behavior of the Callovo-Oxfordian claystone at the Meuse Haute-Marne underground research laboratory (France). *Proc. 8th international symposium on field measurements in geomechanics, FMGM. Berlin, Sep 2011*, pp 12–16

Noiret A, de la Vaissière R, Armand G, Carraretto S, Righini C (2015). Impact of the time dependent behavior of claystone on the fracture development for a drift excavated in three steps. In: *Schubert & Kluckner (Eds.), Future development of Rock Mechanics, Proc. ISRM regional symposium EUROCK 2015 & 64th Geomechanics colloquium. Salzburg, Oct 2015*, pp 609-614. ISBN 978-3-9503898-1-4

Ozanam O, Armand G & Hoorelbeke JM (2016). Echelles de temps et démarche de conception du projet CIGEO / Time scales and design process for the CIGEO project. *Proc. Journées Nationales de Géotechnique et de Géologie de l'Ingénieur, Nancy*, 8 p

Panet M (1979) Time-dependent deformations in underground works. *Proc. 4th ISRM Congress, Montreux,* vol. 3, pp 279-290

Panet M & Guenot A (1983). Analysis of convergence behind the face of a tunnel: Tunnelling 82, *Proc. 3rd international symposium, Brighton, June 1982,* pp 197–204. Pub London: IMM, 1982. In: *International Journal of Rock Mechanics and Mining Sciences & Geomechanics Abstracts* (Vol. 20, No. 1, p. A16)

Panet M (1995). Le calcul des tunnels par la methode convergence–confinement. *Presses de L'Ecole Nationale des Ponts et Chaussees, Paris*. 178 p. ISBN 2-85978-230-3

Panet M (1996). Two case histories of tunnels through squeezing rocks. *Rock Mechanics and Rock Engineering, 29(3),* pp 155–164. doi:10.1007/BF01032652

Pardoen B (2015). Hydro-mechanical analysis of the fracturing induced by the excavation of nuclear waste repository galleries using shear banding. *PhD Thesis, University of Liège - Faculty of Applied Sciences*, Belgium, 263 p

Pardoen B, Levasseur S & Collin F (2015a). Using local second gradient model and shear strain localisation to model the Excavation Damaged Zone in unsaturated Claystone. *Rock Mechanics and Rock Engineering, 48(2)*, pp 691-714. doi:10.1007/s00603-014-0580-2

Pardoen, B, Seyedi DM & Collin F (2015b). Shear banding modelling in cross-anisotropic rocks. *International Journal of Solids and Structures, 72*, pp 63-87. doi:10.1016/j.ijsolstr.2015.07.012

Pardoen B & Collin F (2016). Modeling the influence of strain localization and viscosity on the behavior of underground drifts drilled in claystone. *Computers and Geotechnics – COx claystone excavations special issue*. doi:10.1016/j.compgeo.2016.05.017

Pham QT (2006). Effets de la désaturation et de la resaturation sur l'argilite dans les ouvrages souterrains. *PhD Thesis, Ecole Polytechnique,* France, 202 p

Plassart R (2011). Modélisation hydromécanique du comportement des ouvrages souterrains avec un modèle elastoviscoplastique. *PhD Thesis, Institut National Polytechnique de Lorraine*, France, 207 p

Plassart R, Fernandes R, Giraud A, Hoxha D & Laigle F (2013). Hydromechanical modelling of an excavation in an underground research laboratory with an elastoviscoplastic behaviour law and regularization by second gradient of dilation. *International Journal of Rock Mechanics and Mining Sciences, 58*, pp 23–33. doi:10.1016/j.ijrmms.2012.08.011

Pouya A, Trivellato E, Seyedi DM & Vu MN (2016). Apport des modèles d'endommagement sur la géométrie de la zone de rupture autour des ouvrages profonds dans des roches quasi-fragiles. *Journées Nationales de Géotechnique et de Géologie de l'Ingénieur, Nancy, Juillet 2016*, 9 p

Renaud V & Morel J (2010). Calculs 3D prédictifs pour la conception d'alvéoles de stockage de déchets radioactifs HAVL / 3D predictive calculations for the design of highly-active radioactive waste storage cells. *Tunnels et Espace Souterrain, 221*, pp 383–390

Robinet JC (2008). Minéralogie, porosité et diffusion dans l'argilite du Callovo-Oxfordien de Bure (Meuse/Haute-Marne,France) de l'échelle centimétrique à micrométrique. *PhD thesis, Université de Poitiers*, France, 247 p

Robinet JC, Sardini P, Coelho D, Parneix JC, Prêt D, Sammartino S, Boller E & Altmann S (2012). Effects of mineral distribution at mesoscopic scale on solute diffusion in a clay-rich rock: Example of the callovo-oxfordian mudstone (Bure, France). *Water Resources Research, 48(5)*, 17 p. doi:10.1029/2011WR011352

Robinet JC, Sardini P, Siitari-Kauppi M, Prêt D & Yven B (2015). Upscaling the porosity of the Callovo-Oxfordian mudstone from the pore scale to the formation scale; insights from the 3H-PMMA autoradiography technique and SEM BSE imaging. *Sedimentary Geology, 321*, pp 1–10. doi:10.1016/j.sedgeo.2015.02.007

Robinet R, Plas F, Imbert C & Robinet JC (2015). The initial damage/fractured excavation zone around deep underground facilities in Callovo-Oxfordian formation: modelling of

fractures network using an anisotropic damage approach funded on shear and extension properties of argillites. *Proc. of 6th International Conference of Clay in natural and engineered barriers for radioactive waste confinement. Brussels, March 2015*

Salehnia F, Collin F, Li XL, Dizier A, Sillen X & Charlier R (2015). Coupled modeling of Excavation Damaged Zone in Boom clay: Strain localization in rock and distribution of contact pressure on the gallery's lining. *Computers and Geotechnics, 69,* pp 396–410. doi: 10.1016/j.compgeo.2015.06.003

Sammartino S, Bouchet A, Prêt D, Parneix JC & Tevissen E (2003). Spatial distribution of porosity and minerals in clay rocks from the Callovo–Oxfordian formation (Meuse/Haute-Marne, Eastern France)—implications on ionics species diffusion and rock sorption capability. *Applied Clay Science, 23 (1–4)*, pp 157–166

Schubert W (2008). The development of the observational method. *Geomechanics and Tunelling: 1(5),* pp 352-357. doi:10.1002/geot.200800035

Seyedi DM, Vu MN, Armand G & Noiret A (2015). Numerical modeling of damage patterns around drifts in the Meuse/Haute-Marne URL. *Proc. 13th ISRM Congress. Montréal, Mai 2015*. ISBN 978-1-926872-25-4

Seyedi DM, Armand G & Noiret A (2016). "Transverse Action" – A model benchmak exercise for numerical analysis of the Callovo-Oxfordian claystone hydromechanical response to excavation operations. *Computers and Geotechnics – COx claystone excavations special issue*. doi:10.1016/j.compgeo.2016.08.008

Shao JF, Zhou H & Chau KT (2005). Coupling between anisotropic damage and permeability variation in brittle rocks. *International Journal for Numerical and Analytical Methods in Geomechanics, 29(12),* pp 1231–1247. doi:10.1002/nag.457

Shao JF, Jia Y, Kondo D & Chiarelli AS (2006a). A coupled elastoplastic damage model for semi-brittle materials and extension to unsaturated conditions. *Mechanics of Materials, 38(3)*, pp 218–232. doi:10.1016/j.mechmat.2005.07.002

Shao JF, Chau KT & Feng XT (2006b). Modeling of anisotropic damage and creep deformation in brittle rocks. *International Journal of Rock Mechanics and Mining Sciences*, *43(4),* pp 582–592. doi:10.1016/j.ijrmms.2005.10.004

Song Y, Davy CA, Troadec D, Blanchenet AM, Skoczylas F, Talandier J & Robinet JC (2015). Multi-scale pore structure of COx claystone: Towards the prediction of fluid transport. *Marine and Petroleum Geology, 65*, pp 63–82. doi:10.1016/j.marpetgeo.2015.04.004

Souley M, Su K, Armand G & Ghoreychi M (2009). A viscoplastic model including damage for argillaceous rocks. In: *1st International Symposium on computational geomechanics (COMGEO 2009), IC2E. Rhodes, Juan-les-Pins, France, April 2009*, pp 146-157

Souley M, Armand G, Su K & Ghoreychi M (2011). Modeling the viscoplastic and damage behavior in deep argillaceous rocks. *Journal of Physics and Chemistry of the Earth, 36(17-18)*, pp 1949–1959. doi:10.1016/j.pce.2011.10.012

Steiner PR (2007). Displacement measurements ahead of a tunnel face using the RH Extensometer. In: *Proc. 7th international symposium on field measurements in geomechanics, FMGM. Boston, Sep 2007*, 8 p

Su K (Ed) (2003). Constitutive Models for the Meuse/Haute-Marne Argillites – MODEX- REP, European Commission – Nuclear science and technology, Contract n° FIKW-CT2000-00029, Deliverable 2-3

Su K (Ed) (2007). Development of Hydro-mechanical Models of the Callovo-Oxfordian Argillites for the Geological Disposal of Radioactive Waste – MODEX- REP, European Commission – Nuclear science and technology, Contract n° FIKW-CT-2000-00029, Final report

Sulem J (1983). Comportement différé des galeries profondes. *PhD Thesis, Ecole Nationale des Ponts et Chaussées*, France, 159 p

Sulem J, Panet M & Guenot A (1987). Closure analysis in deep tunnels. *International Journal of Rock Mechanics and Mining Sciences Abstracts, 24(3)*, pp 145–154. doi:10.1016/0148-9062(87)90522-5

Tran-Manh H, Sulem J & Subrin D (2016). Progressive degradation of rock properties and time-dependent behavior of deep tunnels. *Acta Geotechnica, 11(3)*, pp 693-711. doi: 10.1007/s11440-016-0444-x

van den Eijnden B (2015). Multiscale modelling of the hydromechanical behaviour of argillaceous rocks. *PhD Thesis, Université Grenoble Alpes,* France, 263 p

van den Eijnden AP, Bésuelle P, Chambon R & Collin F (2016a). A FE$^2$ modelling approach to hydromechanical coupling in cracking-induced localization problems. *International Journal of Solids and Structures*, *97-98*, pp 475-488. doi:10.1016/j.ijsolstr.2016.07.002

van den Eijnden B, Bésuelle P & Collin F (2016b). Modeling the strain localization around an underground gallery with a hydro-mechanical double scale model; effect of anisotropy. *Computers and Geotechnics – COx claystone excavations special issue*. doi:10.1016/j.compgeo.2016.08.006

Vaunat J, Gens A & De Vasconcelos R (2013). Anisotropic effects in a deep excavation in stiff clays. In: *Computational plasticity XII: Fundamentals and applications – Proc. of the 12th International Conference on Computational Plasticity, COMPLAS 2013, Barcelona, Spain, September 2013,* 8 p

Vincké O, Longuemarre P, Boutéca M & Deflandre JP (1998). Investigation of the poromechanical behavior of shales in elastic domain. *SPE/ISMR 47589*, pp 515–520

Vu TM (2010). Comportement des tunnels en terrains tectonisés – application à la liaison ferroviaire Lyon-Turin. *PhD Thesis, Université Paris-Est,* France, 222 p

Vu TM, Sulem J, Subrin D, Monin N & Lascols J (2013). Anisotropic Closure in Squeezing Rocks: The Example of Saint-Martin-la-Porte Access Gallery. *Rock Mechanics and Rock Engineering, 46 (2)*, pp 231–246. doi:10.1007/s00603-012-0320-4

Wang HF (2000). Theory of linear poroelasticity with applications to geomechanics and hydrogeology. *Princeton University Press, Princeton*

Wileveau Y, Cornet F.H, Desroches J & Blumling P (2007). Complete in situ stress determination in an argillite sedimentary formation. *Journal of Physics and Chemistry of the Earth, 32(8-14)*, pp 866–878. doi:10.1016/j.pce.2006.03.018

Yao C, Jiang QH & Shao JF (2015). Numerical simulation of damage and failure in brittle rocks using a modified rigid block spring method. *Computers and Geotechnics, 64*, pp 48–60. doi:10.1016/j.compgeo.2014.10.012

Yao C, Jiang QH, Shao JF & Zhou CB (2016a). A discrete approach for modeling damage and failure in anisotropic cohesive brittle materials. *Engineering Fracture Mechanics, 155*, pp 102–118. doi:10.1016/j.engfracmech.2016.01.012

Yao C, Shao JF, Jiang QH & Zhou CB (2016b). Numerical study of excavation induced fractures using an extended rigid block spring method. *Computers and Geotechnics – COx claystone excavations special issue*. doi: 10.1016/j.compgeo.2016.11.023

Yven B, Sammartino S, Geroud Y, Homand F & Villieras F (2007). Mineralogy texture and porosity of Callovo-Oxfordian claystones of the Meuse/Haute-Marne region (eastern Paris Basin), *Mémoires de la Société géologique de France*. *ISSN 0249-7549, 17*, pp 73-90

Zhang C & Rothfuchs T (2004). Experimental study of the hydro-mechanical behaviour of the Callovo-Oxfordian argillite. *Applied Clay Science*, *26(1-4),* pp 325–336. doi:10.1016/j.clay.2003.12.025

Zhang CL, Czaikowski O & Rothfuchs T (2010). Thermo-hydro-mechanical behaviour of the Callovo-Oxfordian clay rock. Final Report. GRS – 266. ISBN 978-3-939355-42-7

Zhang CL (2015). Deformation of clay rock under THM conditions. *Geomechanik Und Tunnelbau, 8(5),* pp 426–435. doi:10.1002/geot.201500025

Zhou H, Jia Y & Shao JF (2008). A unified elastic–plastic and viscoplastic damage model for quasi-brittle rocks. *International Journal of Rock Mechanics and Mining Sciences, 45(8)*, pp 1237–1251. doi:10.1016/j.ijrmms.2008.01.004

## A – Analysis of the convergence evolution in drifts

### A.1 – Optimization method

Fitting of the five parameters of the convergence law ($T$, $X$, $m$, $n$ and $C_{\infty x}$), proposed by Sulem et al. (1987), is performed by a gradient optimization method which looks to determine the local minimal. Therefore, the optimization allows to obtain the set of numerical values, for these five parameters, that gives the minimal margin of error between the in-situ measured convergence and the predicted convergence (see Vu 2010):

$$S^{opt} = \min_{T,X,C_{\infty x},m,n} S(T,X,C_{\infty x},m,n) = S(T^{opt},X^{opt},C_{\infty x}^{\ opt},m^{opt},n^{opt})$$

*where* (A.1)

$$S(T,X,C_{\infty x},m,n) = \sum_{x,t} \left[ C(T,X,C_{\infty x},m,n) - C_m(x,t) \right]^2$$

where, $C_m(x,t)$ is the measured convergence in a time ($t$) after the passage of the face and a distance ($x$) of the face; $C(T,X,C_{\infty x},m,n)$ is the convergence predicted by the semi-empirical law; $S(T,X,C_{\infty x},m,n)$ is the error obtained for the convergence predicted with respect to the in-situ convergence; and $S^{opt}$ is the minimal margin of error obtained, which corresponds to the best fit using the optimal parameters value: $T^{opt}$, $X^{opt}$, $C_{\infty x}^{\ opt}$, $m^{opt}$ and $n^{opt}$.

It should be noted that a wide range of parameters values must be analyzed in order to determine the set of parameters most relevant for an accurate reproduction and prediction of the convergence evolution.

*A.2 – Convergence evolution obtained in different sections of GCS drift*
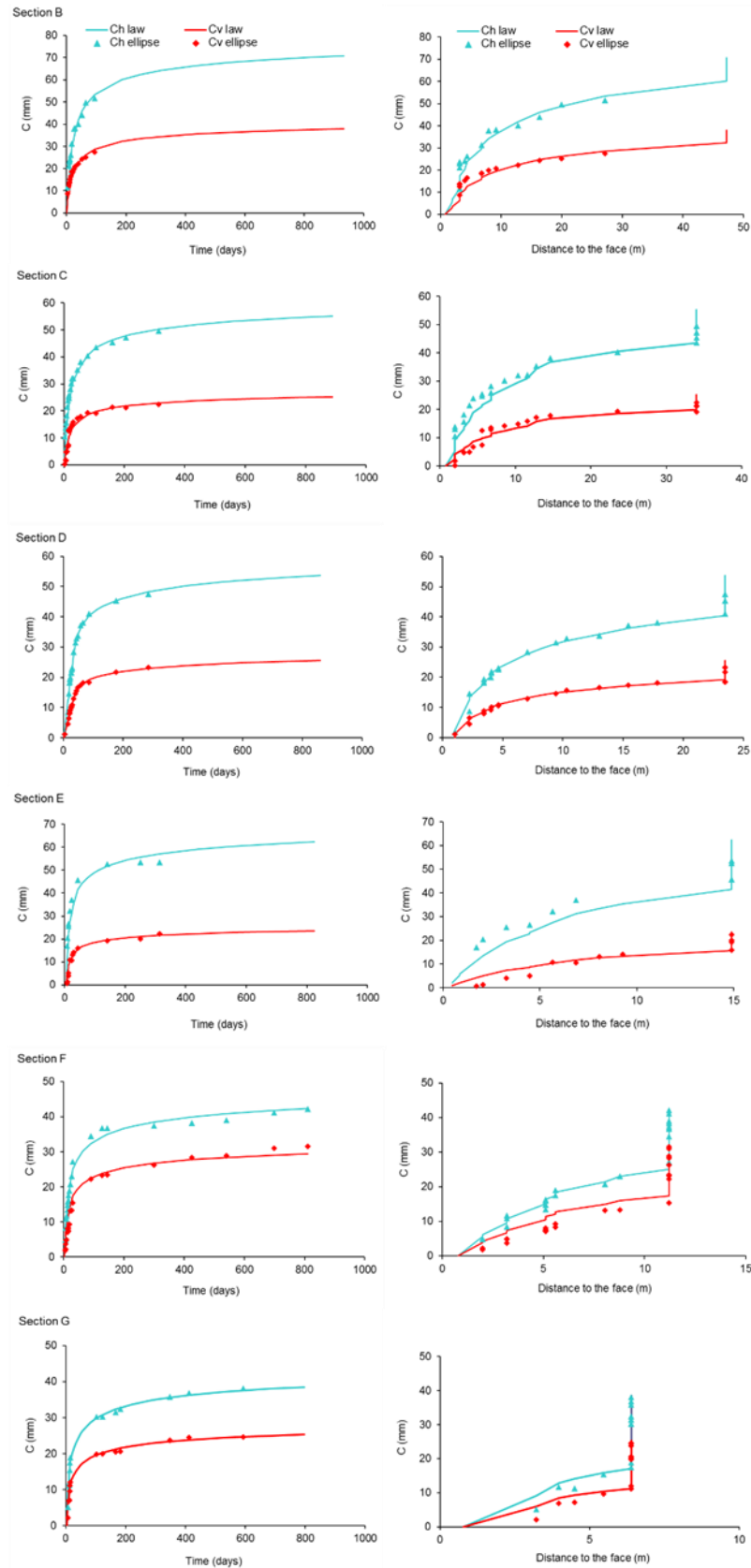


**Fig. A. 1.** Convergence evolutions in sections of GCS drift. Left side: as function of time, Right side: as function of the distance to the face. ($C_h$ = horizontal convergences; $C_v$ = vertical convergences)

## A.3 – Convergence predictability analysis in different sections of GCS drift
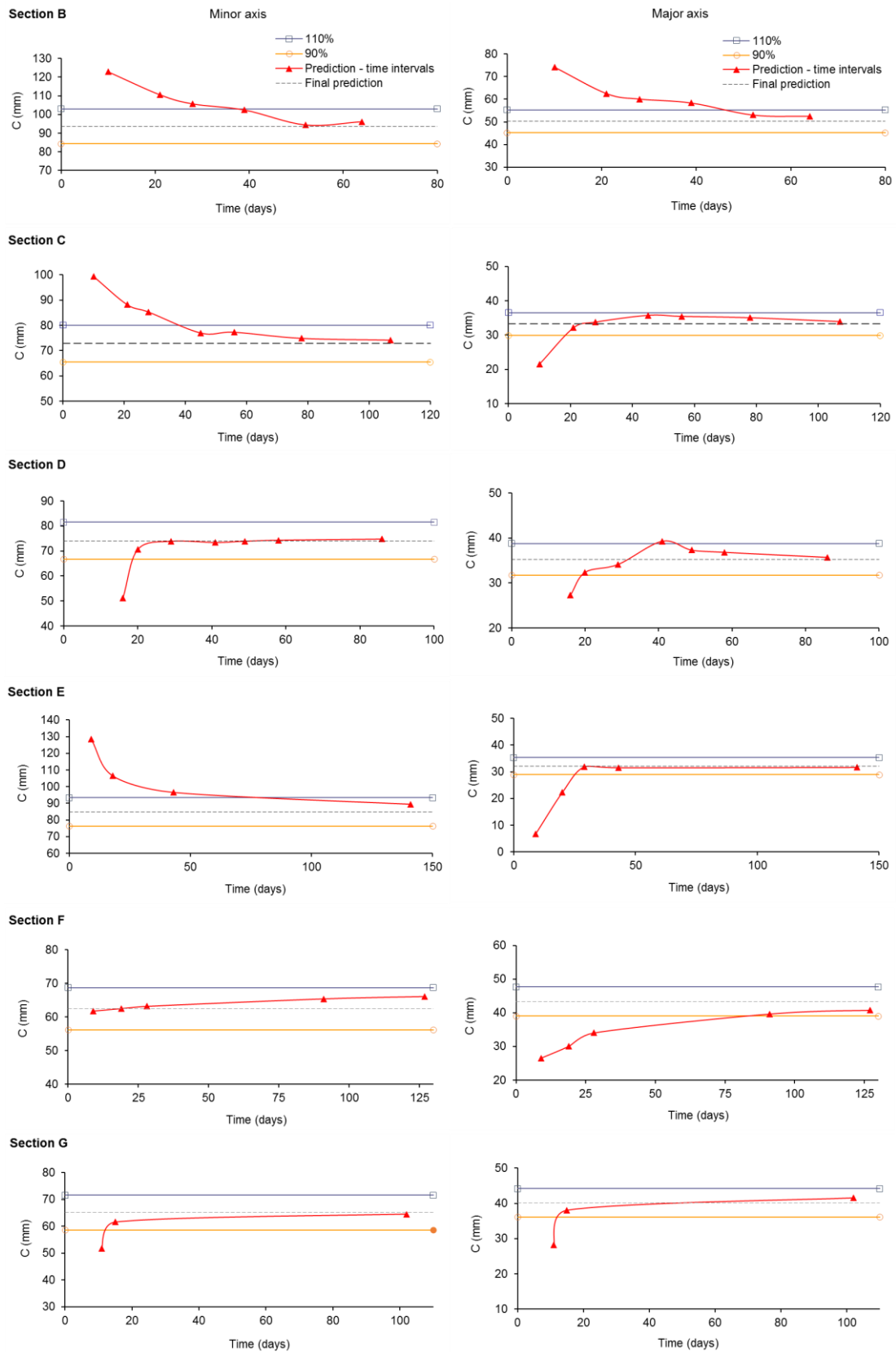


**Fig. A. 2.** Final convergence predictions in GCS drift as a function of the duration of the monitoring

*A.4 – Convergence predictability analysis in different sections of GED drift*
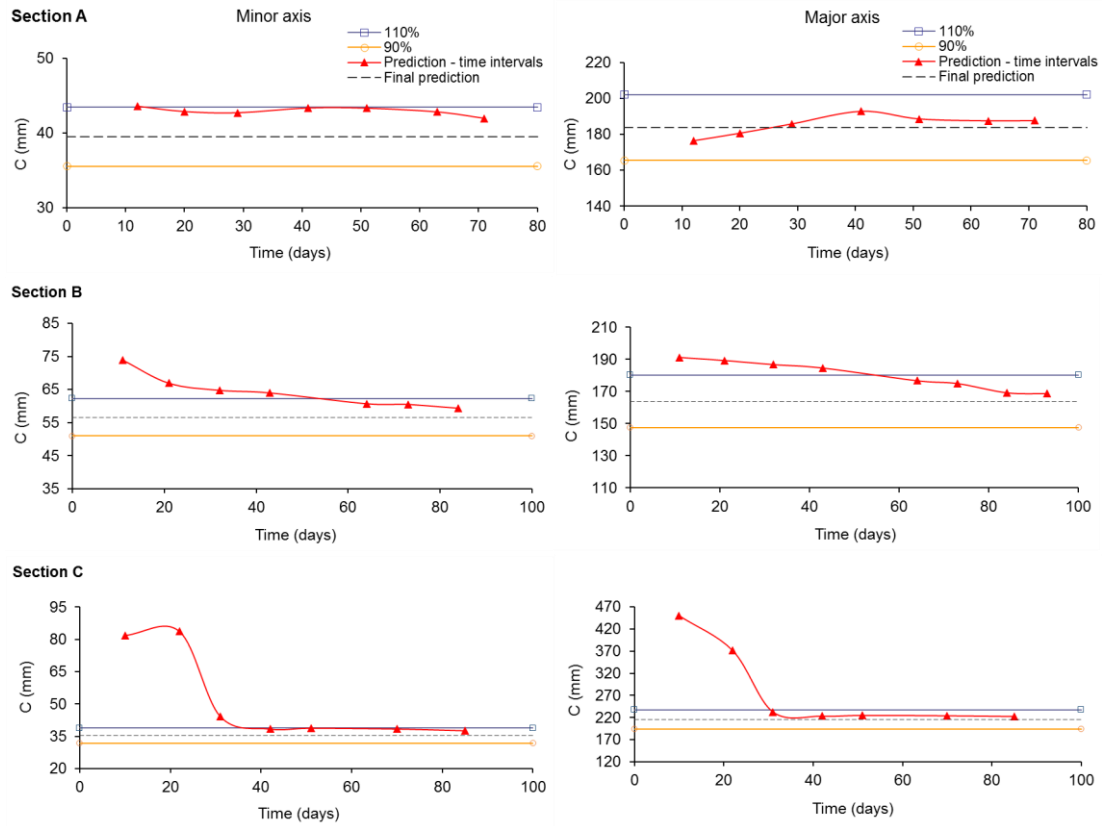


**Fig. A. 3.** Final convergence predictions in GED drift as a function of the duration of the monitoring

*A.5 – Variations on the extent of fracture distribution around different drifts following the direction of $\sigma_H$*

**Table A. 1.** Average extent of lateral fracture distribution around different drifts studied – distance related to the drift diameter

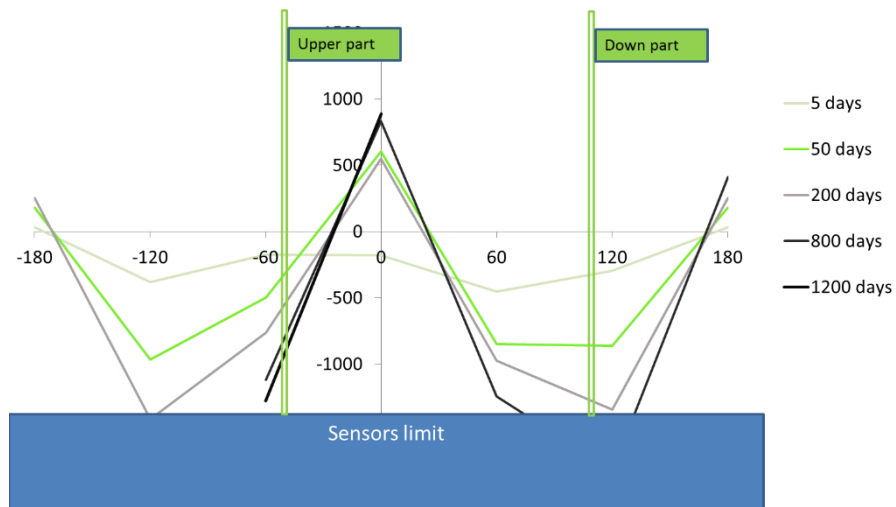| Drift | Tensile fractures | Shear fractures |
|---|---|---|
| | Wall | Wall |
| GCS | $0.17 \times D$ | $0.78 \times D$ |
| GCR | $0.11 \times D$ | $0.57 \times D$ |
| GRD4 | $0.48 \times D$ | $0.95 \times D$ |
| GRM3-stage 1 | $0.46 \times D$ | $0.86 \times D$ |
| GRM3-stage 2 | $0.39 \times D$ | $0.95 \times D$ |
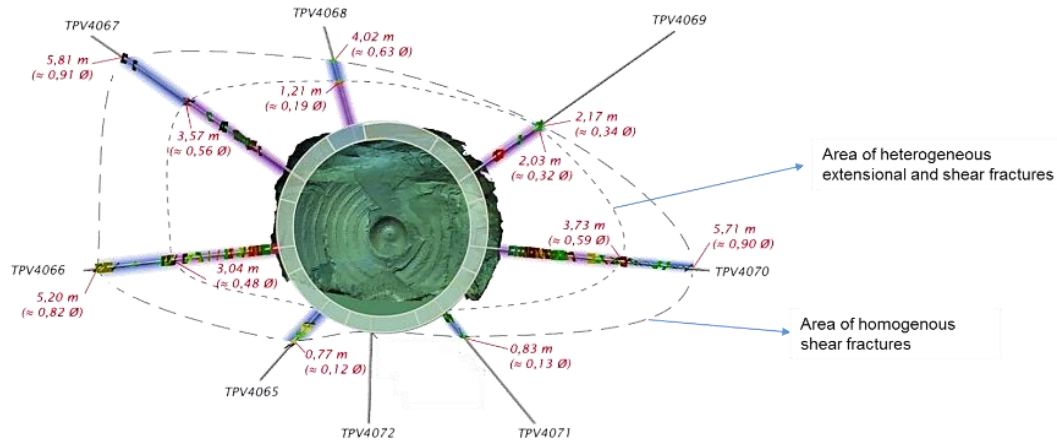


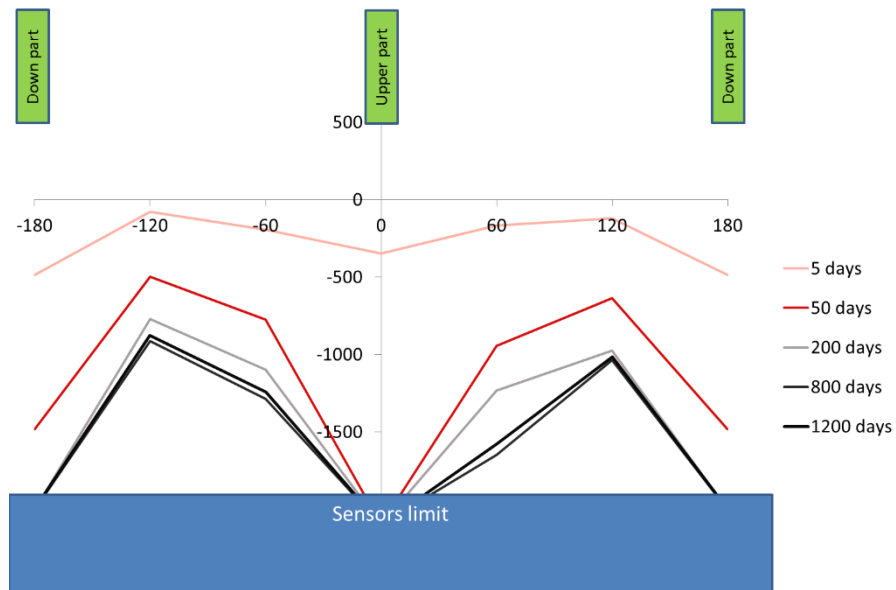**Fig. A. 4.** Fracture distribution observed in GRD4 drift
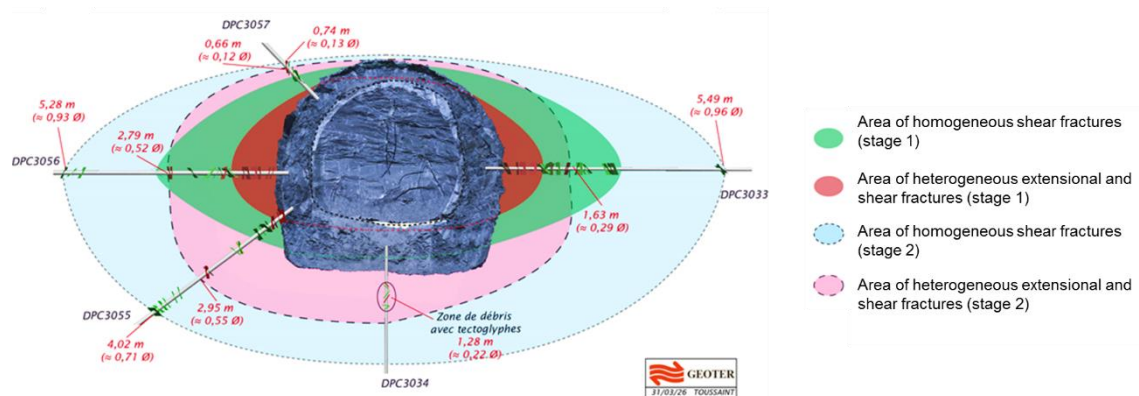


**Fig. A. 5.** Fracture distribution observed in GRM3 drift (adapted from Noiret et al. 2015)

**Fig. A. 6.** Deformation (microdef) evolution as a function of time at GCS drift cross section (Andra database)



**Fig. A. 7.** Deformation (microdef) evolution as a function of time at GCR drift cross section. Section without yieldable concrete wedges (Andra database)

140

## B – Analysis of the pore pressure evolution around drifts

### B.1 – Validation of the numerical model

The validation of our numerical code is performed based on a comparison with the analytical solution developed by Detournay and Cheng (1988) for the isotropic poroelastic response of a borehole in a non-hydrostatic stress field. This 2D analytical solution is derived in the Laplace transform space, and is transformed to the time domain using an approximate numerical inversion technique. As explained by Detournay and Cheng (1988), the loading is decomposed into three fundamental modes: (1) a far-field isotropic stress condition (classical Lamé solution in elasticity); (2) a uniform constant pore pressure distribution; and (3) a far-field stress deviator (Fig. B.1). Solutions for the induced stress, pore pressure and displacements are derived for each fundamental loading modes and superposed.
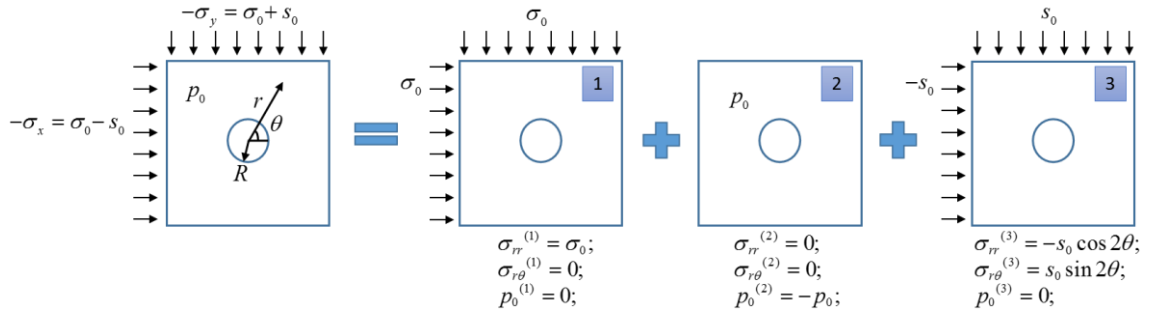


**Fig. B. 1.** Problem definition (adapted from Detournay and Cheng 1988). $\sigma_0$ and $s_0$ are the far-field mean stress and stress deviator, respectively; $p_0$ the initial pore pressure; $r$ and $\theta$ are the polar coordinates; and $R$ the excavation radius

The numerical simulation performed under plane strain conditions is implemented in the finite element code FreeFem++. The size of the finite element model is 100 m × 100 m considering a radius ($r$) of the drift of 2.6 m. Fig. 3.3 shows the model geometry, the finite element mesh, and the initial and boundary conditions. Table B.1 summarizes the set of poromechanical parameters used for the simulation.

**Table B. 1.** Elastic mechanical and hydraulic parameters. Comparison between numerical and analytical solutions

| $\sigma_{x,0}$ (MPa) | $\sigma_{y,0}$ (MPa) | $E_x$ (MPa) | $E_y$ (MPa) | $\nu_{xz}$ | $\nu_{yx}$ | $G$ (MPa) | $b$ | $k_x$ (m²) | $k_y$ (m²) | $\phi_0$ |
|---|---|---|---|---|---|---|---|---|---|---|
| 12.4 | 12.7 | 4000 | | 0.3 | | 1540 | 0.6 | $2.7 \times 10^{-20}$ | | 0.18 |

A comparison between numerical and analytical results for the instantaneous response of the pore pressure and of the displacements is performed (Fig. B.2). Considering the very low permeability of the material, a simulation based on the undrained conditions (i.e. no-flow boundary condition) is more appropriate to represent the instantaneous response of the ground. In addition, a comparison of the pore pressure evolution is also performed at different times: 10 days, 1 month and 2 months (Fig. B.3). It is observed that the numerical model gives accurate results which are very close to the analytical solution. For the numerical simulations, time step is $\Delta t = 5$ days.
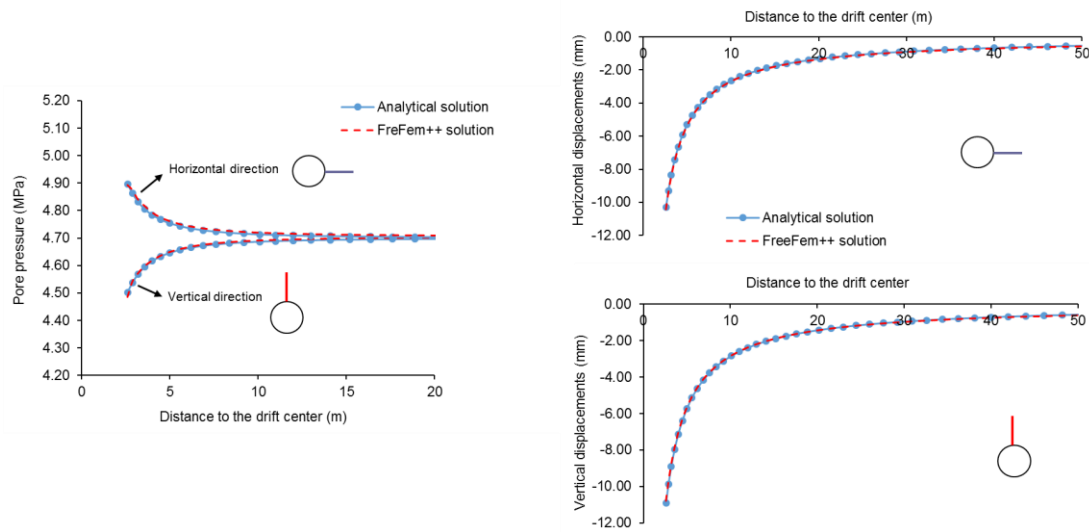


**Fig. B. 2.** Pore pressure response and displacements obtained for an instantaneous response. Comparison between the numerical simulation and the analytical solution proposed by Detournay and Cheng (1988)
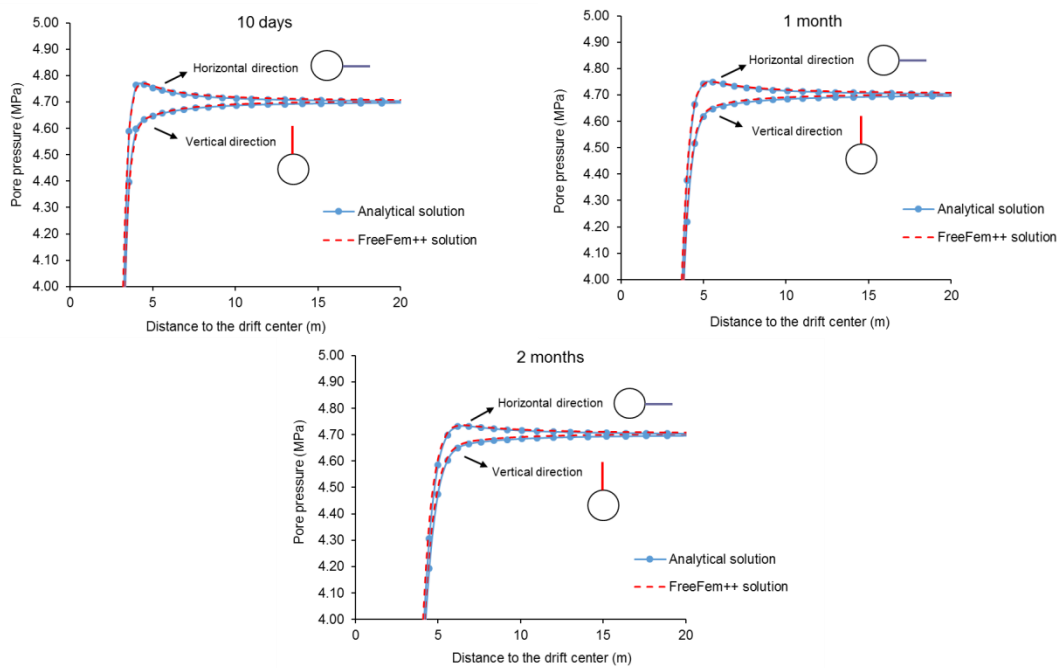


**Fig. B. 3.** Pore pressure evolution with time. Comparison between the numerical simulation and the analytical solution proposed by Detournay and Cheng (1988)

For the anisotropic case, a comparison is performed by comparing the numerical results obtained with the FreeFem++ code and those obtained with the well-known software Code_Aster. This comparison is based on a fully coupled analysis taking into account the influence of the inherent anisotropy of the material. Table B.2 summarizes the parameters used for the comparison and Fig. B.4 presents the comparison of some results obtained in both simulations. It is observed that the results obtained are very similar in the two simulations.

**Table B. 2.** Elastic mechanical and hydraulic parameters. Comparison between numerical simulations in FreeFem++ and Code-Aster

| $\sigma_{x,0}$ (MPa) | $\sigma_{y,0}$ (MPa) | $E_x$ (MPa) | $E_y$ (MPa) | $\nu_{xz}$ | $\nu_{yx}$ | $G$ (MPa) | $b$ | $k_x$ (m$^2$) | $k_y$ (m$^2$) | $\phi_0$ |
|---|---|---|---|---|---|---|---|---|---|---|
| 12.4 | 12.7 | 5600 | 4000 | 0.2 | 0.3 | 1750 | 0.6 | $4.0 \times 10^{-20}$ | $1.33 \times 10^{-20}$ | 0.18 |
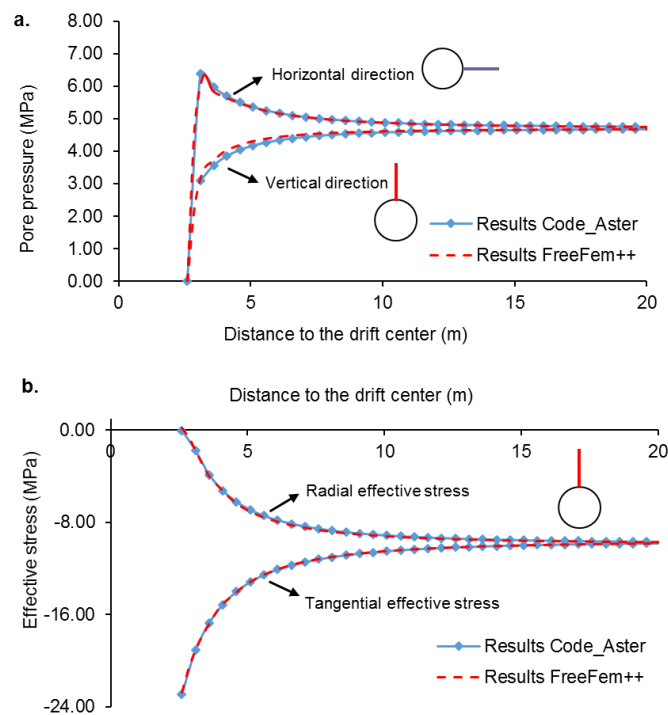


**Fig. B. 4.** Response after one hour for an excavation in drained conditions. Comparison between a simulation performed in FreeFem++ and a similar simulation performed in Code_Aster. a. Pore pressure evolution in the horizontal (0°) and vertical (90°) direction of the drift cross section. b. Radial and tangential effective stresses obtained in the vertical direction (90°) of the drift cross section

*B.2 – In-situ observations of the pore pressure changes around excavations (from Armand et al. 2015b)*

Fig. B.5 shows the measurements performed at different diameter openings at the M/HM URL (with 5 m, 0.7 m and 0.15 m of diameter). It is observed that the maximum overpressure measured is situated at about 1 to 1.5 diameters from the wall. Moreover, in-situ measurements show substantial overpressures rather far inside the rock mass. Fig. B.6 presents the pore pressure evolution in time showing an overpressure inside the rock for several months.
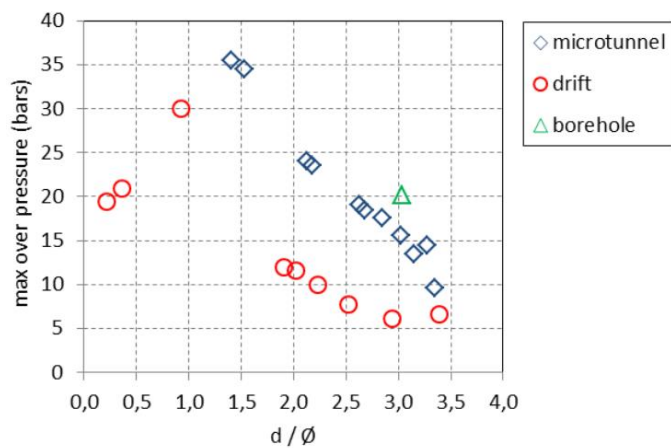


**Fig. B. 5.** Maximum over-pressure measured at the wall side of different diameter openings: drift of 5 m diameter, micro tunnel of 0.7 m diameter and borehole of 0.15 m diameter (d: distance to the wall, $\phi$ diameter of the drift). (Fig. 11 from Armand et al. 2015b)



(a)

(b)
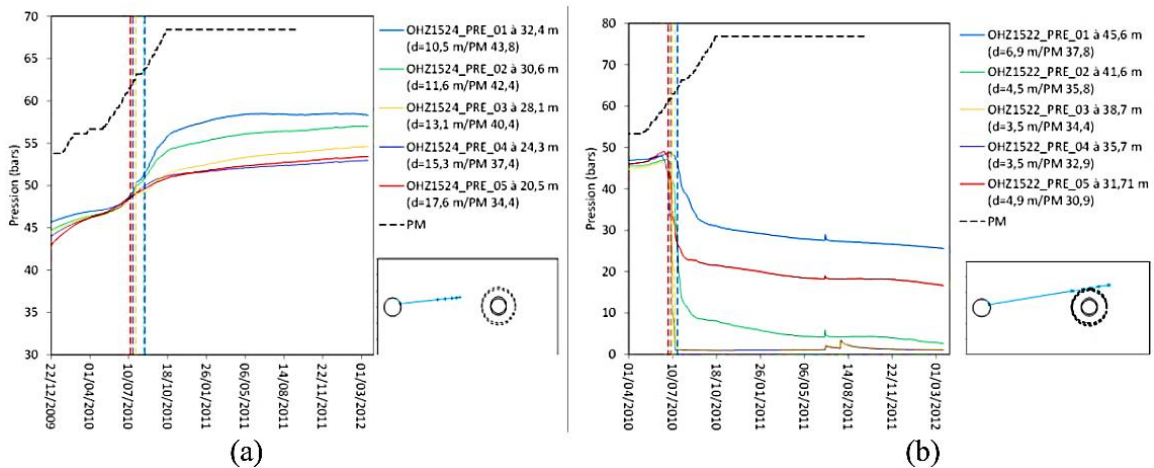
**Fig. B. 6.** Long-term pore pressure evolution : (a) in borehole OHZ1524 on GCS side wall, (b) in borehole OHZ1522 above GCS (PM is the location of the front as function of time, d is the distance of the chamber to final drift wall, colored dash line is the date when front face cross the section of the pore pressure measurement ) (Fig. 7 from Armand et al. 2015b)
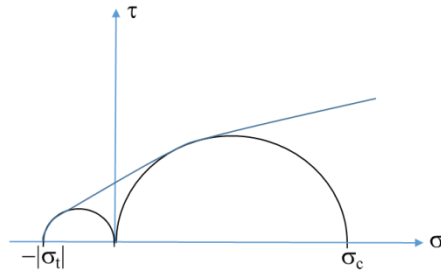
## B.3 – Fairhurst's generalized Griffith fracture criterion

The equation of Mohr's circle (0, $\sigma_c$) is given in eq. B.1 and the equation of the parabola tangent to the Mohr's circle (0, $\sigma_t$) is defined in eq. B.2 (Fig. B.7):

$$\left(\sigma-\frac{\sigma_c}{2}\right)^2+\tau^2=\left(\frac{\sigma_c}{2}\right)^2 \tag{B.1}$$

$$\tau^2=b(\sigma+|\sigma_t|) \tag{B.2}$$

where, $b$ is a constant.



**Fig. B. 7.** Enveloppe of Fairhurst's generalized Griffith fracture criterion

In order to look for the parabola equation, which is tangent to both Mohr's circles (0, $\sigma_c$) and (0, $\sigma_t$), first, from the combined solution between the derivate of eqs. B.1 and B.2 we can obtain:

$$b^2-b\left(2\sigma_c+4|\sigma_t|\right)+\sigma_c^2=0 \tag{B.3}$$

where, the roots are:

$$b=(w\pm1)^2|\sigma_t| \tag{B.4}$$

with, $w=\sqrt{n+1}$ and $n=\sigma_c/|\sigma_t|$. Inserting Eq. (B.4) in Eq. (B.2) and in order to avoid imaginary roots, the equation of the parabola tangent to both Mohr's circles (0, $\sigma_c$) and (0, $\sigma_t$) is defined as:

$$\tau^2=(w-1)^2|\sigma_t|\left(\sigma+|\sigma_t|\right) \tag{B.5}$$

Then, considering the general Mohr's circle equation

$$\left(\sigma' - \frac{\sigma_1' + \sigma_3'}{2}\right)^2 + \tau^2 = \left(\frac{\sigma_1' - \sigma_3'}{2}\right)^2 \tag{B.6}$$

and inserting eq. B.5 in eq. B.6, we obtain

$$A|\sigma_t|(\sigma_1' + \sigma_3') - 2AB\sigma_t^2 = (\sigma_1' - \sigma_3')^2 \tag{B.7}$$

with, $A = 2(w-1)^2$ and $B = \left[(w-1)/2\right]^2 - 1$. Thus, $\sigma_1'$ can be written as:

$$\sigma_1' = \frac{(2\sigma_3' + A|\sigma_t|) + \sqrt{(2\sigma_3' + A|\sigma_t|)^2 - 4(\sigma_3'^2 - A|\sigma_t|\sigma_3' + 2AB\sigma_t^2)}}{2} \tag{B.8}$$

Noted that this is a criterion of fracture initiation for any $n$ when,

$$\frac{\sigma_1' - \sigma_3'}{2} \leq \frac{(w-1)^2}{2}|\sigma_t| \tag{B.9}$$

considering the case when $\sigma_3' = -|\sigma_t|$ and $\sigma_1' = 0$, it is obtained

$$0 \leq w(w-2)|\sigma_t| \tag{B.10}$$

by definition $w$ is positive, thus $(w-2) \geq 0$, which implies that this criterion is valid for any $n \geq 3$